Identification of Structural Phases in Pillared-Layered, Amino-Functionalized M$_2$(abdc)$_2$(dabco) (M = Co, Ni, Cu, Zn)

Master Thesis in Chemistry

By Michal Rohde

University of Bergen

April 2023

Acknowledgements

I would first like to express gratitude to my supervisor, Prof. Pascal D. C. Dietzel. Thank you for this unforgettable project and opportunity, for the hours you've endured with me, and for training me to be the best chemist and crystallographer I can be. You are a scientific role model worthy of appreciation, and it was a pleasure working with you. Thank you for believing in me and showing me how to use the variety of instruments located in our cozy lab. During the last two years I have spent in the Dietzel group, there have been a lot of helpful, encouraging, and great people around me, which helped me persevere through the task of completing this thesis. I wish to extend many thanks to the current and previous Dietzel group members, including Amalie Skurtveit, Vilde Sandtorv, Ida Marie Bentsen, Ticiane Oliveira, Denise Dilsehner, Julie Brun and Amrita Panigrahi. I wish all of you the absolute best in your future careers and undertakings. Thank you for immense support and for being able to make a usual day into something more unique every time.

List of abbreviations

Abbreviation	Description
abdc	2-aminobenzene-1,4-dicarboxylate, conjugate base deprotonated from former acid (H_2abdc)
bdc	1,4-benzenedicarboxylate, conjugate base deprotonated from former acid (H_2bdc)
dabco	1,4-diazabicyclo[2.2.2]octane
DMF	N,N-dimethylformamide
ATP	(abdc)$_2$(dabco)
TP	(bdc)$_2$(dabco)
(H_2abdc)	2-aminobenzene-1,4-dicarboxylic acid
(H_2bdc)	1,4-benzenedicarboxylic acid
PXRD	Powder X-ray diffraction
CPO	Coordination polymer of Oslo
MOF	Metal organic framework
GDS	Gibbs dividing surface
ESRF	European Synchrotron Radiation Facility

Abstract

In the rising popularity of nano-structures, it is no doubt that MOFs are among the most curious of such materials. They impress researchers with their high porosity and selectivity towards various noxious gases, like CO_2, CO or NO_2 all while retaining a finely intricate crystallinity, which is easily tunable to further their capabilities. They have been of special interest in gas storage, capture and separation of fluids. Composed of organic and inorganic building blocks, they create frameworks which spread in all three dimensions, creating vast arrays. These arrays are mostly empty, as the majority of a MOF is but a void. These pores can vary from Å to nm in diameter.

In this project, a set of four analogues of $M_2(abdc)_2(dabco)$ (M = Co, Ni, Cu, Zn, abdc = 2-aminobenzene-1,4-dicarboxylate, dabco = 1,4-diazabicyclo[2.2.2]octane) are closely inspected for their structures during three different phase transitions, which can help in understanding these pillared-layered MOFs. Especially their enigmatic second phase will be brought to more light, as at the time of writing it is poorly documented. Analysis will be performed on data obtained at ESRF synchrotron in 2021 and will utilize powder X-ray diffraction. The plots will also be run through sequential refinement, to closely investigate the change in lattice parameters. $M_2(abdc)_2(dabco)$ (M = Ni, Cu) were also synthesized and differing synthesis variables were tested to possibly improve on the existing procedure. Textural properties of these samples were analyzed with N_2 adsorption.

Table of contents

1.Introduction

Seeing the worrying and exponentially growing damage to the climate, the idea of green chemistry is more prevalent now than ever before. In such a broad field, there are a plethora of good candidates that could help mitigate the dire effects of global warming. One of the most prominent ones are carbon capture and storage facilities (CCS)[1]. CCS is mainly used to capture CO_2 from exhaust gasses of major industrial buildings, like factories and coal-based power plants, and then store these gasses deep underground. However, even this technique requires a lot of resources, for instance, compounds that can separate CO_2 from other gasses, as it cannot be captured when contaminated[2].

A promising addition to the CCS technology might be in the form of highly porous nanomaterials, eloquently named metal-organic-frameworks, or MOFs for short[3]. MOFs are a line of zeolite-like, highly porous nanoparticles, from a family of coordination polymers[4]. These materials showcase a high-level crystallinity, and their physical properties make for interesting experiment in the labs and potential applications in nature, like gas storage[5,6] and removal of toxic chemicals[7] or gasses like NO_2[8]. Today there are various types of MOFs, each differing in topology, but each and every one focusing on attaining maximum porosity[5,9-11] and stability[12,13]. The pores of these structures can have a diameter reaching from 1 Å to 1 nm, which naturally will determine their physical properties. Because of their high porosity, MOFs are able to attain up to several thousand square meters of surface area in just one gram of material. Such a trait allows for fluids to be captured, separated and stored; all done in the pores[14,15]. This makes MOFs a perfect subject for usage in catalysis, filtering, sensors or simply as a compact gas storage. The latter is most significant, considering the high amounts of CO_2, alongside other greenhouse gases, in the air. MOFs might be a very viable solution to safely and efficiently dispose of notorious gasses or fluids[7,16].

Highly porous, coordination polymers have been known about since early 1910's[17], but they haven't been examined more closely before 1990's, most notably by the likes of Kitagawa[18] and Yaghi[3,19]. It was then that the terminology MOF started to gain traction among the scientific community[3]. In 2013 it was finally defined by IUPAC as "coordination network with organic ligands containing potential voids"[20]. As the name suggests, a singular elementary unit crystal is composed of an inorganic, metallic center, which most often are various d-block elements like Cu, Co, Ni or Fe, and an organic ligand (a linker) that binds the entire framework into a coherent, 3D structure[4,21]. The metallic center can be composed of either metal ions or metal clusters and is not necessarily limited to just *d*-block elements, but can also include $s-$ or p metals[9,22]. The usage of different building blocks and synthesis methods will result in different structures, with differing properties. Not all MOFs possess rigid structures, as for instance the MIL-53 has a high pore flexibility[22,23]. On the other hand, the ones with

rigid frameworks are often synthesized with the goal of maximal stability and/or adsorption capability. UiO-66 and CPO-27 both display a quality of high thermal and chemical tolerance[5,12,13,24].

MOFs have been scientifically researched for roughly three decades now[21], where their most important qualities were surface area, porosity and structural integrity. HKUST-1 (HKUST = Hong Kong University of Science and Technology) was among the first MOFs to display permanent porosity[19,25]. It is also structurally relevant to this thesis's material of interest, as it possessed paddle-wheel, Cu-based units[19]. Today, most MOFs are not created at random, rather, they are following well calculated procedures that can make a specific type of MOF, with a highly predictable structure. It is a method often referred to as reticular approach[26,27]. MOFs are highly tunable nanomaterials, leading to new MOFs being synthesized at very fast rates[28], leading to plenty of design possibilities. Different inorganic and organic components can be used together, in a very lenient fashion, allowing for nearly endless combinations. Exchange of the inorganic component is usually the first one when one wants to research a specific MOF more closely, as varying d-block elements rarely lead to varying structures. Exchanging organic ligands for bigger ones, most often lead to enlargement of the pores without changing the fundamental structure of the MOF[29,30]. Organic linker can also be changed or even modified, as the molecule is very prone to the functionalization of its groups, such as OH, NH_2 or Br. MOFs can, and often do possess the same topology, in which case they are said to be isoreticular[31].

1.1 Synthesis of MOFs

The mechanism of building a MOF follows the same principle that is observed for other nanostructures, called self-assembly[32]. It is an autonomous and spontaneous process, under which the disperse, organic linkers and ions aggregate together due to the presence of weak forces like van der Waal forces and hydrogen bonds. The resulting structure is usually highly ordered and not randomized, as the individual components want to exist in the lowest possible energetic state. After the first structure is completed, called an elementary unit, it is then grown further by the rest of the components. The growth continues until the depletion of materials or spatial constraint is reached (Figure 1.1).
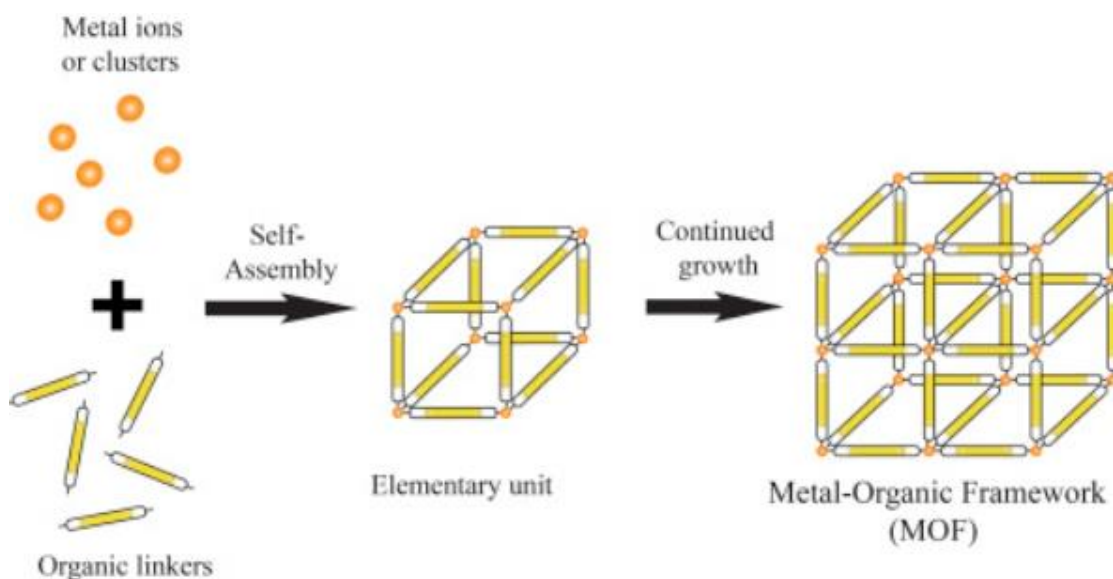
Figure 1.1 - Schematic of how a MOF is synthesized via self-assembly.

Self-assembly is a part of a larger series of methods of synthesizing nanoparticles, called bottom-up approach. It is, alongside the top-down approach, the main method of achieving nano-scaled structures. For MOFs however, only the bottom-up approach is relevant, and possible.

The usual method for synthesizing MOFs is the *solvothermal* method. It involves the loose components in a suspension with a desired solvent, under a strict and constant temperature that is higher than solvent's boiling point in a tightly locked vessel[33]. Solvents like methanol, ethanol, N'N-dimethylformamide (DMF), tetrahydrofuran (THF) and methyl-2-pyrrolidone (NMP) have been reported as being used in the solvothermal synthesis of MOFs[33,34]. Water also can be used as solvent in which case the method is then called a *hydrothermal* synthesis. Teflon inlets are commonly used as reaction vessels, due to their high temperature tolerance and non-reactive nature. They are lined with a steel autoclave, which allows for much better thermal conductivity, as well as sealing the inlet shut due to pressures exceeding 101.0 kPa being generated in the inlet. Variables such as time in the oven, concentration or temperature and pressure often must be experimented with, in order to find the path that gives desired results. It is important that the conditions remain uninterrupted for the synthesis's entire runtime, as only then can steady nucleation and crystal growth occur, leading to the desired crystal phase[34]. Despite there existing many different methods like hydrothermal, microwave-assisted[35], sonochemical[36] and mechanochemical[37], the solvothermal has by far been used and researched the most. It is used to synthesize most reported MOFs, including CPO-27-M series[10,11,38] and the $M_2(abdc)_2(dabco)$[39,40].

1.2 $M_2(abdc)_2(dabco)$

The star of this thesis is a slightly more involved MOF, compared to its contemporaries. Unlike the standard MOFs, which are a network composed of linkers coordinated to a metal center which then is grown in three dimensions, the MOF in the spotlight of this thesis is arranged from two different organic linkers, both coordinated to the metallic center. One of these ligands is of neutral character, while the other possess a dicarboxylic acid functional group. The 3D network is then comprised out of two-dimensional sheets, made out of the functionalized organic linker coordinated to the metal, while in between these sheets are the neutral organic ligands, often named organic *pillars*. For this reason, the compounds are classified as *pillar-layered* MOFs[41-45] (Figure 1.2).
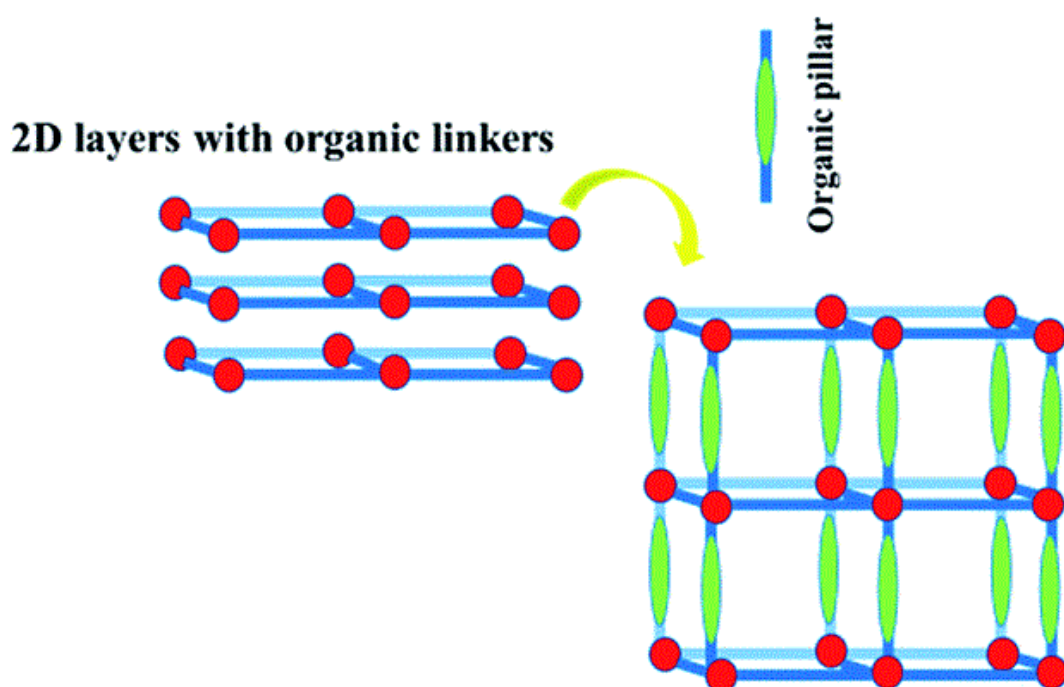

Figure 1.2 *- Schematic of a typical pillar-layered MOF*

The most common ligands used as pillars are 4,4-bipyridine and 1,4-diazabicyclo[2.2.2]octane (dabco)[46], while the ligands used as linkers are commonly either 1,4-benzenedicarboxylic acid (H_2bdc)[41] or 2-aminobenzene-1,4-dicarboxylic acid (H_2abdc)[47] (Figure 1.3). The latter ligand is what the majority of the thesis will be focusing on, although it is very similar in both structure and function to $H_2(bdc)$. Its major difference lies in the functionalized NH_2 group, which has been observed to have an affinity towards CO_2[39,40,47]. $M_2(abdc)_2(dabco)$ is thus isoreticular to $M_2(bdc)_2(dabco)$.
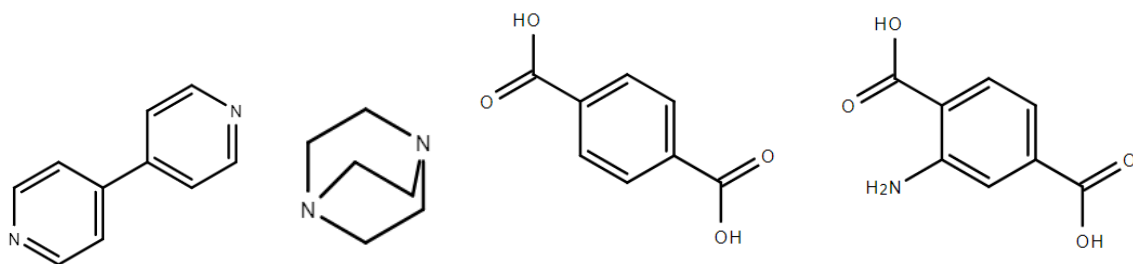
Figure 1.3 - From left to right: 4,4-bipyridine, dabco, H_2bdc and H_2abdc

By looking at Figure 1.4 closer, one can observe that the network of MOFs that follow the pillared-layer formula M_2L_2X (M= Fe, Cu, Co, Ni, Zn; L= a functionalized organic ligand; X=a neutral ligand) are assembled from units that possess a unique structure. The pillar ligands are coordinated axially via N-atoms to the metal, while the organic linkers are interconnected equatorially on one plane. The structure of each such unit closely resembles a paddle wheel[41,48], which is where these units got their name from (Figure 1.4).
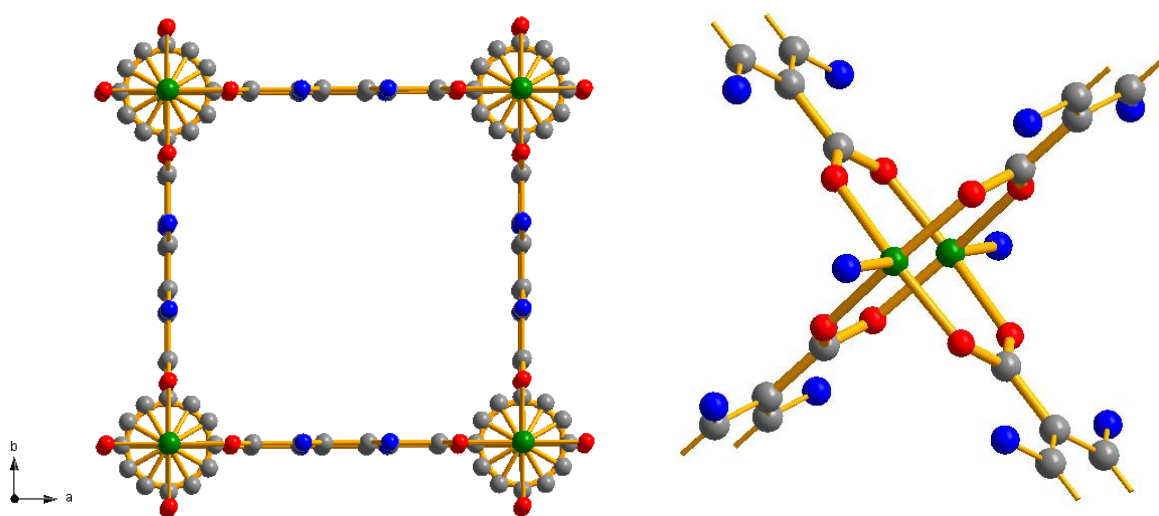

*Figure 1.4, left – A unit cell of $Ni_2(abdc)_2(dabco)$ in P4/mmm space group as viewed along the c-axis, with four visible paddle-wheel units at each corner. **Right** – Closer look at an individual paddle-wheel unit, with disordered N-atoms on abdc and singular N-atoms from dabco. (Green = Ni, blue = N, red = O, grey = C)*

2.Objective of the Thesis

The primary objective of the thesis was to synthesize, identify and measure the adsorption potential of four $M_2(abdc)_2(dabco)$ analogues (M=Co, Ni, Cu, Zn) using *high-pressure* adsorption method. That would require large quantities of the sample, so that multiple synthesis procedures were used, all based on previous work [1]. Quantities of the reactants were scaled-up, but later ordinary quantities were used, as to simply blend the smaller samples into a single, large one. Unfortunately, due to apparatus complications, this was shown to not be possible, alongside the samples not being on the same level of quality as the reported samples[41,48]. Despite the failures, the experiments performed have shown interesting results, that will definitely prove useful when working with these materials in the future. The objective then shifted towards a detailed X-ray structural analysis of the compound at each of three phases using data obtained from synchrotron 2019[48]. Identification of the X-ray peaks, indexing of space groups and obtaining ideal profile fit (and potentially a structure) has become the new objective. The main giveaway from doing that is the ability to have a detailed structural information about every phase of each $M_2(abdc)_2(dabco)$ analogue, which will be helpful in further experiments.

3.Characterisation Methods and Theory

Despite MOFs being relatively new concept, there exist a variety of characterization procedures, which are able to identify in detail important aspects of these nano-materials. Among them are low-and- high pressure adsorption analysis, powder X-ray diffraction, single X-ray diffraction, thermogravimetric analysis, scanning electron microscopy and Fourier transform infrared spectroscopy[49]. However, only the first two methods are going to be relevant to this paper.

3.1 Adsorption

Adsorption can occur in two different ways: chemisorption and physisorption[50] (Figure 3.1). Chemisorption is a much more energetically involving process, where covalent bonds are formed between the adsorbate (the guest molecules) and the adsorbent (the adsorbing solid) and is usually quite rare[51]. Physisorption is the adsorption of adsorbate molecules onto the adsorbent via weak forces, most notably the van der Waal forces. Physisorption is an exothermic process and results in lowering of the adsorbent's surface tension. A system in which adsorption takes place is comprised of three elements: solid, gas and the adsorption space. The number of adsorbed molecules, n_a, in the adsorption space is dependent on the unknown volume, V_a. To counter this, an assumption is made stating that adsorption is a fully 2D process, so that $V_a = 0$, which takes place on an imaginary film known as Gibbs dividing surface (GDS)[50]. With that assumption, one can calculate the amount in gas phase, n_g, by the use of appropriate gas laws. Surface excess amount, n_σ, is so defined as the difference between all adsorptive molecules in the system, n, and n_g.
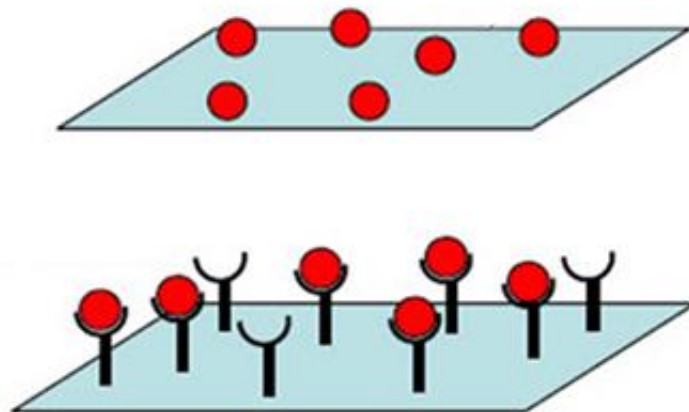
Figure 3.1 - Visualization of physisorption (up) and chemisorption (down), with a substrate surface (blue plane) and binding sites (black hooks)

Most often, for experiments carried at <100kPa, n_a is roughly equal to n_g (low-pressure adsorption). The relation between n_a and the pressure of gas at equilibrium, at constant temperature, is known as the adsorption isotherm[50]. The adsorption is often carried out below the critical temperature of the adsorptive, meaning that relation of equilibrium pressure, p, and saturation vapor pressure (point where liquid and its vapor exist in equilibrium), p_0, can be used in plotting the isotherm. Analysis of adsorptive properties of materials are most often carried out at very cold temperatures (critical temperatures of adsorbates), as the adsorption is most efficient then due to lower kinetic energy of the adsorbate molecules.

Although a surface may seem simple on the grand scale, it is much more complex on the atomic scale. A section of the solid may be considered to be divided into multiple levels. The van der Waal level is the uttermost level (green line, Figure 3.2) and is formed by the outermost atoms on the surface. The next surface is the purely theoretical Conolly surface, where physisorption takes place (blue line, Figure 3.2). Notice how the spherical guest molecule (probe) is fitted perfectly into the cavity between two solid spheres. The blue line also outlines the surface that is available for guest molecules. The red line depicts the accessible radius, r, from the Conolly surface.
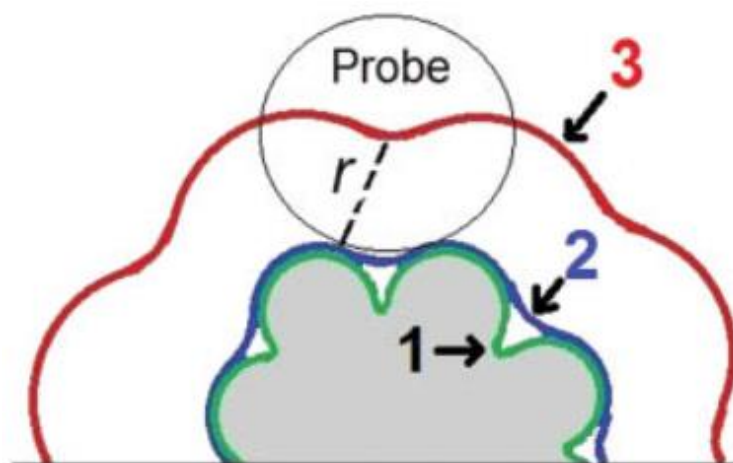
Figure 3.2 – Interaction levels on solids, on the atomic scale

When talking about adsorption onto porous solids, it's important to separate between external (surface on the outside of the pores, non-microporous) and internal surface (surface inside the pores). Pores can exhibit wildly different sizes and are classified as micropores (< 2 nm), mesopores (2-50 nm) and macropores (> 50 nm). Do note that $M_2(abdc)_2(dabco)$ is microporous, with pores of only few Å in length. Because of their much smaller size, micropores are not *covered* but *filled* with the adsorbate molecules. Their filling is occurring at low pressures and is hierarchical, meaning that the smallest micropores are usually filled first (if they are not uniform). This difference makes many models depicting surface coverage quite inaccurate due to the nature of micropore filling.

3.1.1 Heat of adsorption

Heat of adsorption (or enthalpy of adsorption) is an important aspect of the process, as it describes the amount of energy released/absorbed by an adsorption event. It is easiest to summarize it as a value describing the strength of adsorbate-adsorbent interaction. It is most often calculated by low-pressure measurements, spanning different, usually non-cryogenic temperatures[51]. These enthalpies can be so used to determine the efficiency and selectivity of the sites on a material, and whether it can be used in specific future applications. For physisorption, enthalpies up to around 30 kJ/mol can be observed. For comparison, a C-C bond has enthalpy of roughly 350 kJ/mol, which should put into perspective how weak these interactions are (which can nevertheless be quite significant on macro scale).

3.1.2 Isotherm plots

Isotherms are constructed by a continuous measurement with either manometric (used in this paper) or gravimetric method[50]. Manometric method measures the amount of gas removed from the gas phase, while gravimetric method is a direct measurement of the gas uptake via weight measurement. Before the measurement, dead-space need to be precisely calculated, which is the required amount of gas to fill the space around the adsorbent. Dead-space is usually measured by non-adsorbing and inert gas, like He, and its precision is directly responsible for the potential errors in the overall analysis. A proper outgassing is required for accurate measurements later, since leftover gas could also significantly impact the results, especially when working with microporous materials. The manometric analysis entails an injection of adsorbing gas of known amount to a sample which is confined in a calibrated volume, all of which happens under isothermal conditions (static temperature). As the gas adsorbs, the pressure will fall down until the point of equilibrium, where the difference between admitted gas and dead-space is the amount adsorbed gas. There exist six types (I-VI) of isotherms, with each being able to describe porosity of a given material (Figure 3.3).
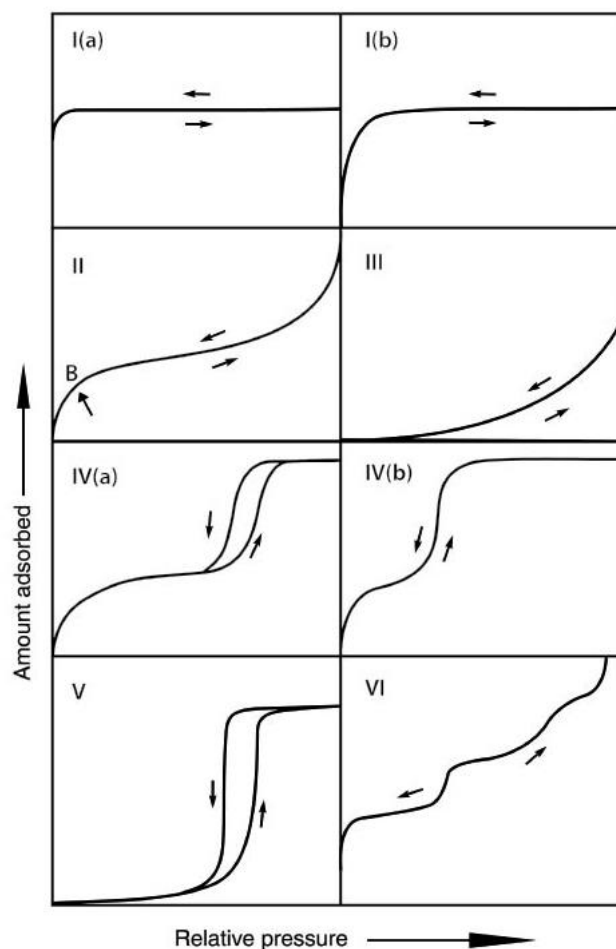

***Figure 3.3** – Physisorption isotherm types*

Type I (a) isotherms are reversible and easily recognized by their flatness across almost the entire axis. They are given by microporous materials with very small external surfaces. The limited adsorption is due to narrow pores and their restricting access. The uptake is nevertheless quite high at lower pressures due to energetic, microporous surfaces which enhance the adsorbent-adsorptive interactions. Type I (b) isotherms are very similar and occur in solids with wider micropores. Type I isotherms are most relevant to this paper, since CPO-27-Cu is known to be a microporous MOF.

Type II isotherms are reversible and given by either macroporous or nonporous solids. The shape is due to unrestricted monolayer and multilayer build-up even at high pressures. A characteristic "knee", or B-point, describes the point where a monolayer is most likely filled. The more gradual curves are much more ambiguous when it comes to monolayer filling and multilayer formation.

Type III reversible isotherms are also given by nonporous or macroporous solids. Without any point B, it means that no monolayer is ever completed as molecules only cluster around the most energetic sites. This suggests weaker adsorbate-adsorbent interactions.

Type IV reversible isotherms are given by mesoporous adsorbents. A monolayer-multilayer adsorption can be noticed at first, similar to Type II, on the mesopore walls. The further adsorption is due to pore condensation, which is a phenomenon where gas condenses into a liquid-like state in a pore. It is also known as capillary condensation. A plateau at the end is characteristic of this type of isotherm. Type IV (a) features a distinctive hysteresis loop due to pore width exceeding critical width, which is a term that depends on the system parameters (temperature, gas etc.). Type IV (b) occurs with narrower mesopores, as it's perfectly reversible. Notice how the first plateau in Type IV (b) is shorter, hinting at an earlier capillary condensation.

Type V reversible isotherm features a rapid pore filling due to clustering, followed by a plateau. It is reminiscent of Type III at lower pressures, suggesting weakened adsorbate-adsorbent interactions. It's not a common isotherm, mostly occurring in hydrophobic micro/mesopores and with water as the adsorptive. Hysteresis occurs most likely due to the clustering of adsorbate, which results in pore condensation.

Type VI reversible isotherm occurs in nonporous solids with a homogenous surface. Each plateau represents a layer, and the overall isotherm shows a multilayer adsorption. Capacity of each monolayer can be derived from the step height.

3.1.3 Hysteresis plots

Type IV and V exhibit an example of something called a hysteresis loop. Hysteresis loop is the result of desorption, which may take a different path than the adsorption depending on the complexity of the solid's network. A complex network may be a mesopore, but with a very narrow pore opening. Pore blockage is not uncommon and can happen in mesopores with narrow openings. The escaping gas may clog the opening, resulting in a blocked bottleneck until the blocking molecules evaporate. The higher concentration of molecules at the neck may result in temporary condensation, which can lead to nucleation and creation of gas bubbles, known as cavitation. To recognize the hysteresis types more easily, five classifications have been reported (Figure 3.4).
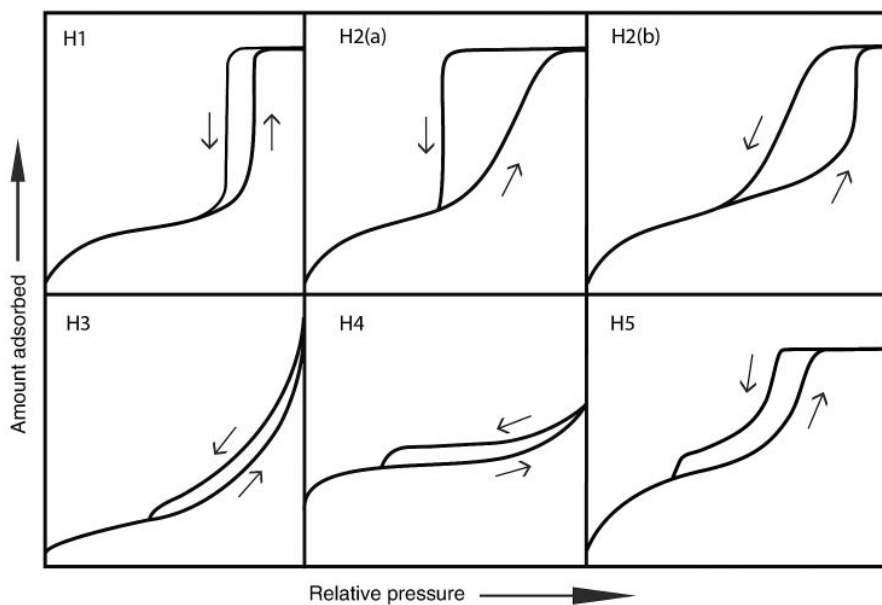

Figure 3.4 – Types of hysteresis loops

H1 is very simple, suggesting a non-complex network structure of pores. This hysteresis occurs in uniform mesopores. It has the same shape as the original curve, pointing towards a delayed condensation.

H2 is found in more complex structures with noteworthy effects. The steepness of the curve is the result of either pore blockage due to narrow necks or cavitation. In H2 (b) the desorption branch looks different due to wider necks.

H3 curves heavily resemble Type II isotherm and is given by macropores which are not completely filled with pore condensate. The lower part of the desorption branch is usually located at the cavitation point.

H4 resembles Type I isotherm and is associated with micropore filling. The hysteresis may be due to temporary clogging of the pores.

H5 is quite rare, but mostly associated with materials where mesopores can be open and closed.

3.1.4 Langmuir and Langmuir-Freundlich models

The adsorption process is difficult to observe at macroscopic scales. Various models have been proposed to explain adsorption in solids, yet still none of them is able to function properly without specific assumptions. Nevertheless, they remain useful tools, proven experimentally to predict the behavior of adsorbate molecules well enough in most cases. Many of these models are modifications of already existing theories, and some may even be empirical. The ones used for calculations in this paper, will be described below.

The Langmuir model is the first model to arrive at the scene[52]. It describes adsorption (more specifically; chemisorption) as adsorptive molecules getting adsorbed into energetically uniform sites. To achieve this, the model runs on multiple assumptions: no formation of multi-layer, a perfectly homogenous surface and surface energy, adsorption sites are energetically equivalent and no interactions between seated adsorbate molecules as well as their complete immobility. In accordance with the model, adsorption and desorption are reversible processes. (Eq. 3.1) describes the base model and how the number of occupied sites, θ_A, relates to gas volume adsorbed, V, and gas volume monolayer that covers the entire surface, V_m. It can also be seen how partial pressures, p_A, relate to V and V_m.

$$\theta_A = \frac{V}{V_m} = \frac{K_{eq}^A p_A}{1 + K_{eq}^A p_A}$$

(3.1)

The model is limiting when it comes to very rough and non-homogenous surfaces. These types of surfaces have new accessible sites with varying parameters, most often the heat of adsorption. Another problem occurs with the neglection of adsorbate-adsorbate interactions. The guest molecules can interact with each other to either fill the site in an unexpected way (for instance, deviating from a monolayer) or not fill it all, depending on the site's size. To account for the problems, there exists several modifications to the Langmuir model, like Dual-Site Langmuir (DS, for short), Triple-Site Langmuir (TS) and Langmuir-Freundlich model. DS/TS Langmuir focuses on an idea where one adsorbate molecule is adsorbed onto two/three distinct sites respectively.

Each of these sites can so be described with its own expression, independent of the other sites. The implementation of different sites can make calculations more accurate to the reality. Langmuir-Freundlich considers multi-site adsorption in addition to the base assumptions of the Langmuir model. It is based on the empirical formula for isotherm presented by Freundlich (Eq. 3.2). The isotherm describes relation of mass of adsorbate, *x*, and mass of adsorbent, *m*, towards the pressure of gas, *p*. The K and n are constants, and they depend on the type of adsorbate and adsorbent at a given temperature. This means that the adsorption is very much determined by pressure and does not take additional effects and miniscule forces into account.

$$\frac{x}{m} = Kp^{1/n} \tag{3.2}$$

By combining both formulas, a new formula can be derived (Eq. 3.3). It can be easily noticed that the Langmuir-Freundlich equation bears striking resemblance towards the Langmuir equation (Eq.3.1), but with parameters taken from the Freundlich equation (Eq. 3.2).

$$\theta_e = \frac{(K_{LF}C_e)^{1/n}}{1 + (K_{LF}C_e)^{1/n}} \tag{3.3}$$

3.1.5 BET model

Brunauer-Emmett-Teller model (BET for short) is probably the most widely used theoretical model for describing adsorption onto solid surface, specifically the calculation of specific surface area[53]. Type II and IV isotherms are well defined by BET plots, as other types shouldn't utilize BET. Type I isotherms (w. microporous surfaces) can utilize BET, but it's often extremely different to separate the filling of micropores from external surface covering. The model is a direct extension of the Langmuir model, where many limiting assumptions are either omitted or exchanged with new assumptions. The major difference between the two being that BET allows for creation of monolayers, in a theoretically infinite manner. There is also no need for a layer to fully form, before a new is being built. The Langmuir model, however, can be applied to each individual monolayer that is formed. BET assumes no interaction between gaseous adsorbate molecules, but the adsorptive molecules can interact with adjacent layers. Enthalpy of adsorption is always highest for the first layer, lowering with each consecutive layer. To apply BET model, the specific isotherm needs first to be transformed into a linear BET plot. From this point onwards, one can apply a closely related Rouquerol criterion[54]. These are the set of criteria used when calculating BET surface for microporous materials. It is meant to optimize the selection of data from the measurement. These criteria include:

i, Obtaining a linear fit to the BET transformed data,

ii, A positive C-constant,

iii, η_{ads} must increase continuously with p/p_0

iv, η_m (monolayer capacity) should be within the limits of the data used

v, The value $\dfrac{1}{\sqrt{C}+1} \approx p/p_0$ at the monolayer capacity

A BET plot can be linear at multiple places, which makes the interpretation quite subjective. Extended criteria are added to make the finding of linearity in the BET plot much more objective, thus scientific. Points ii and iii are the criteria that eliminates this problem.

3.2 Powder X-ray Diffraction

A crystal is composed of arranged atoms, ions or molecules, that give the crystal a specific shape, which depends on the components and their packing. The smallest repetitive unit that describes said packing with respect to possible symmetry operations, its coordination of atoms, is called a *unit cell*[55]. Unit cells extend in three dimensions, thus creating the crystal that is observed on a non-micro scale. Several unit cells put together form a so-called crystal *lattice,* which together with the information of the unit cell, gives additional details of the unit cell's neighboring environment. In crystallography, any unit cell is visualized as a quadrilateral cage formed by the principal axes, with angles α, β and γ, and *a, b, c* coordinates, which are named *lattice parameters* (Figure 3.5)[55]. Inside a given lattice, one can form a *lattice plane*, which is a plane created from a set of integer descriptors, *h, k, l -parameters,* or Miller indices. Miller indices are based on the Cartesian coordination system, where *hkl*-parameters describe the distance from origin to the unit's cell border. For instance, a *hkl* of (001) describes a plane that is located at the top of the unit cell, as only the z-coordinate is set to 1 (Figure 3.5). Sometimes, *hkl* may be larger than 1; in that case it's said that the unit cell is extended. The important difference to make is that Miller indices only define the spatial positions, while lattice parameters describe the approximate distances and angles.
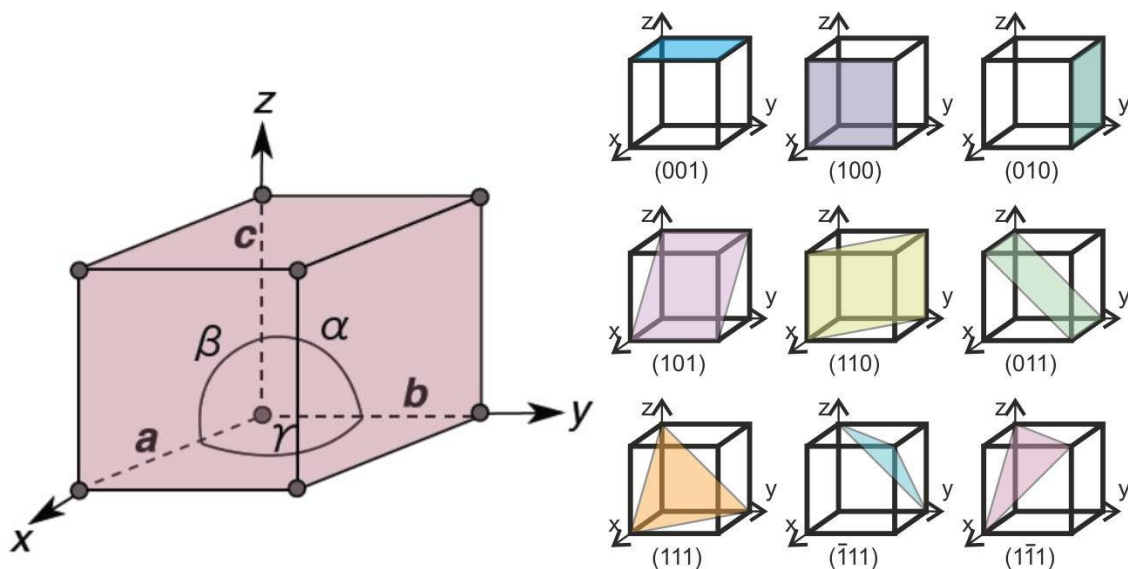

Figure 3.5 Left - *Cartesian coordinate system with a drawn unit cell, showcasing a, b, c coordinates and α, β, γ angles.* ***Right*** *– Examples of colored lattice planes described by Miller indices (in parentheses)[56]*

The crystal's intrinsic periodicity of the structure, and its lattice planes' ability to reflect a beam of highly energetic electromagnetic radiation are the fundamental qualities that make powder X-ray diffraction (PXRD) possible[55]. Because of this, any material possessing crystallinity is able to showcase a diffraction pattern, i.e. a pattern that visualizes all possible reflections of the lattice planes. "Possible" is the keyword here, as the incident X-ray's wavelength must be calibrated to a specific order of magnitude to reflect from the planes. The specificity is dependent on the interatomic distances of the unit cell, which are of only few angstroms (Å) in length. Fortunately, X-rays' wavelengths already exist in the Å-range, so that only a finetuning is necessary. To describe the process of reflection itself in detail, Bragg's law will be necessary. The law stands as a crucial component in the innerworkings of X-ray diffraction (Eq. 3.4)[55].

$$\lambda n = 2d_{hkl}\sin\theta \tag{3.4}$$

In the equation, λ is wavelength, n is *reflection order*, d_{hkl} is separation distance between two lattice planes and θ is the angle at which the X-ray beam interacts with the atoms. The properly tuned monochromatic beam of photons is sent towards the atoms located on the lattice planes from all possible angles, θ. These photons are then reflected by the electrons, populated mostly in areas around the atoms. An individual reflection like that will not be detectable, so it needs to be magnified by approximately same reflections from similarly positioned atoms, through the process of constructive interference, where two waves of the same wavelength and phase can converge into one (Figure 3.6). Only then are the intensities high enough to be recognized as a peak. The constructive (or destructive) interference is enhanced with the increase of the reflection order n[55,56]. Each pattern, or collection of said peaks, that emerges will create a "fingerprint" of the desired crystal, each with various diffraction peaks. Each of the peaks is attached to a specific Miller index, which also can show which planes are most prevalent in a structure. The positions of these peaks contain the structural information of the unit cell (*a, b, c, α, β, γ*) and relate to the overall periodic nature of the crystal[56][57]. The intensities of these peaks are describing the distribution of scattering matter (electron densities) within the cell[55].
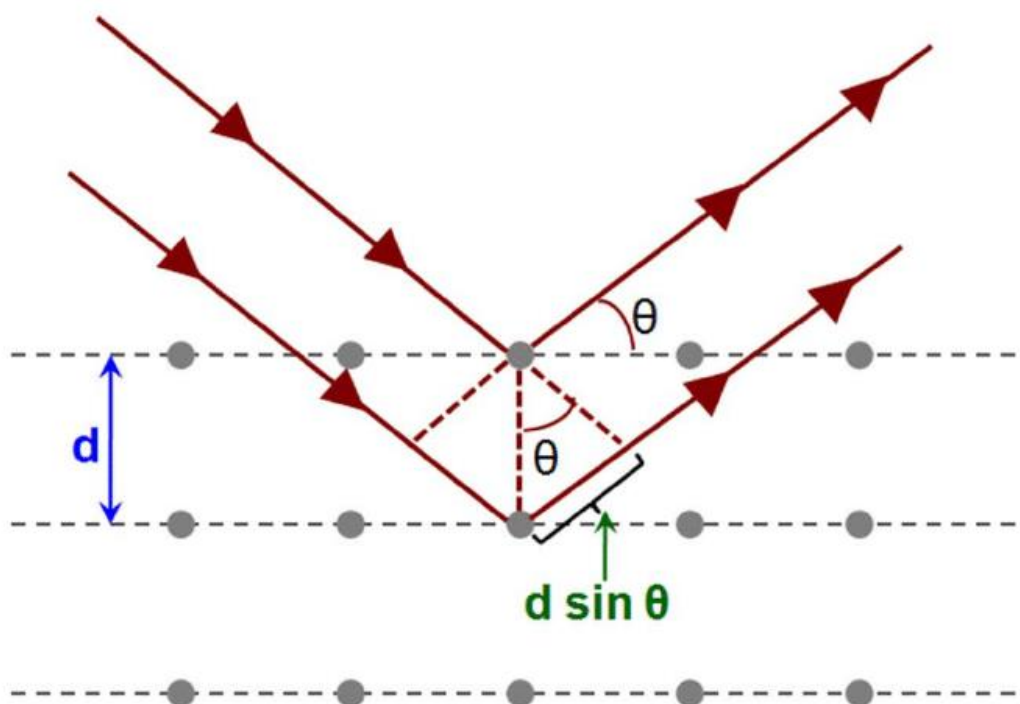
Figure 3.6 - *Diagram depicting a reflection process. Grey dots represent atoms, while dotted lines represent the lattice planes, with the distance d_{hkl} between them.*

Single crystal diffraction and PXRD both can display the same information about a compound, however, there are key differences in their methodologies, which is why they both exist as very valid methods at identifying crystalline structures[57]. Single crystal diffraction produces data by irradiating a single element of a crystalline structure with large enough surface area with monochromatic X-rays. The reflected beams are then captured by the detector, together with their finely defined spacings (Figure 3.7). This method is advantageous when it comes to peak identification, as the data is presented in a three-dimensional format and the peaks are well separated. However, the growth of a sufficiently large crystal may pose a challenge, or even an impossibility in some cases. When crystal used is of insufficient size, the data becomes fuzzier, leading to various errors[57]. PXRD produces its data by irradiating a sample containing millions of tiny nanocrystals with finely tuned monochromatic X-rays. Unlike single-crystal, these crystallites are oriented in random directions, meaning that only collective, or superimposed, reflections of the whole sample can be measured. It is important that preferred, non-random orientation is absent, as it can display "false" data, which is usually observed with strong *hkl*-dependence. The diffractions take the form of a set of cones (Figure 3.7), with an angle equal to the diffraction angle 2θ, forming so-called powder rings[55, 57]. By integrating these rings, data can be presented as a plot of diffraction angle 2θ and intensity. The data is presented in a one-dimensional format, meaning that peak overlap may be prevalent, and potentially lead to erroneous results.
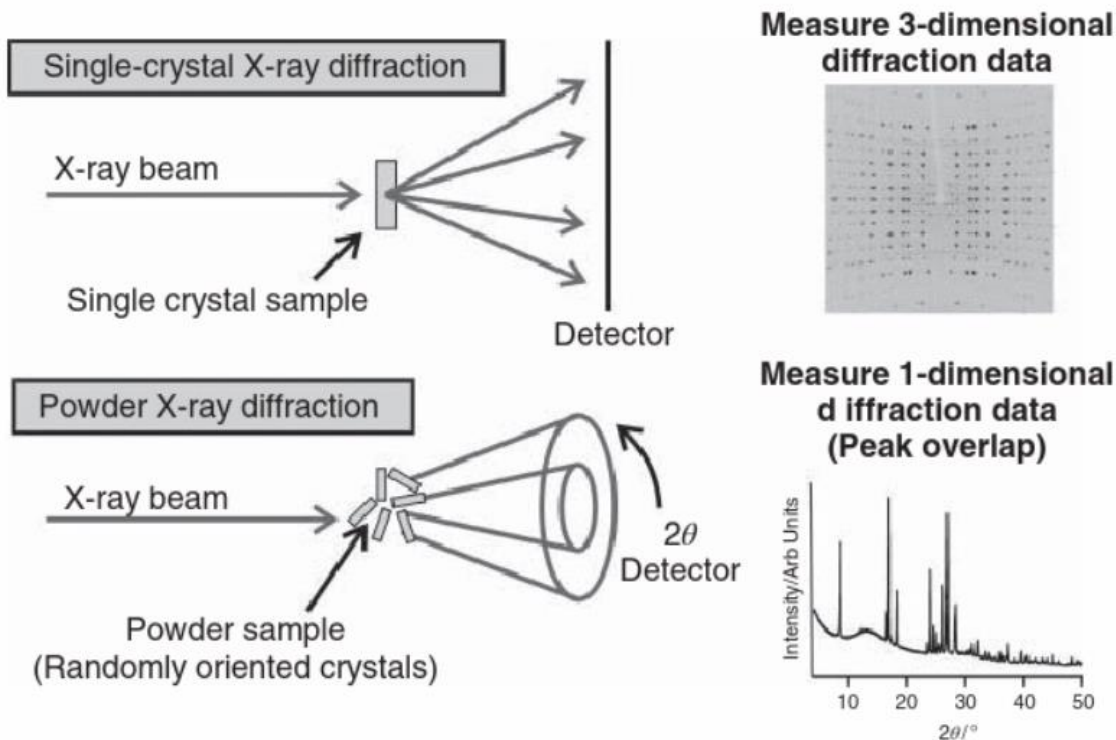
Figure 3.7 – Simple schematic showcasing the difference in operation of single-crystal diffraction and PXRD, together with the respective data produced by the techniques.

PXRD, however, is much more common crystallographic technique than single-crystal, due to its simple procedure[57]. Good results can be obtained even from smaller samples. It is more important that the crystallites are of similar size, and are well positioned on the sample holder. While many modern labs may possess X-ray diffractometers, the overall best data is produced in the synchrotrons. Synchrotrons produce X-ray radiation by utilizing high-speed electrons' change of momentum due to an interference from a magnetic field[58]. The main difference here is that these X-rays are much more energetic, with energies exceeding 100keV, which enables them to penetrate the matter much more effectively than conventional X-rays. The result is a much larger resolution of the data, which may minimize peak overlap and overall, much narrower peaks[57, 58].

3.2.1 Analyzing the data

Ultimately, the model of the unit cell is achieved by following these steps: indexing, profile fitting, determination of structure and refinement[57]. The process of analyzing data of an unknown structure starts with indexing of the PXRD pattern. For this process to be most accurate, one needs enough defined peaks in the dataset; 20 is usually the safest choice. From interplanar distance d_{hkl} of the reflections, the respective lattice parameters can be calculated with Bragg's law (Eq. 3.4).

The result of indexing is usually presented as a list of solutions, pointing towards the most favorable space groups, given the observed lattice parameters. Several space groups should be tested before continuation, as not always the first one will be the best one to fit the data. Additionally, space groups can have varying degrees of symmetry, and usually those with highest symmetries are favored (although they still need to match the data).

Important information is stored in five variables: peak positions, background intensity distribution, peak widths, peak shapes and peak intensities[57]. Profile fitting is a process of creating a calculated fit to the observed pattern. Pawley method is used, allowing for finetuning of variables that define the peaks, which are the five variables mentioned above[59]. Background intensities are also included and need to be accounted for, most often by using an integer value of Chebyshev polynomials[55]. Peaks can have Gaussian, Lorentzian or both characters, all of which are probabilistic models[60], used to make the fit match the data better. Spherical harmonics can also be used to account for possibility anisotropic peak broadening[61]. They are a set of functions, describing the surface of a sphere, which is particularly useful here, since atoms are assumed to be spherical balls. Various other functions can be used to idealize the fit, like a Simple Axial model, which can help when dealing with asymmetrical peaks[60] (not a case in this thesis). The calculated fit needs to be as accurate as possible, as it will be used for further analysis.

Structure determination is mostly performed by a method called simulated annealing[62]. It is a technique which moves atoms into randomized (or user-defined) positions within the unit cell. One such iteration will most likely be erroneous, thus several thousands are run, in order to acquire the most plausible structure for the given Pawley fit, with smallest value for error.

Lastly, Rietveld refinement is used to finetune and refine the raw model produced by simulated annealing[63]. All variables used in the two previous methods are put through refinement, which follows the well-known least square methods. Data should be acquired appropriately and include geometry of diffractometer, quality of calibration, X-ray source, wavelength, slit sizes and necessary counting time. Both the intensities and 2θ values need to be correct.

The final fit should closely resemble the observed pattern. Throughout the analysis a variable named weighed powder factor, R_{wp}, is used to determine the error between the calculated and observed pattern (Eq. 3.5)[63].

$$R_{wp} = \sqrt{\frac{\Sigma_{i=1}^{N} w_i (y_{obs} - y_{calc}(p))^2}{\Sigma_{i=1}^{N} w_i y_{obs,i}^2}}$$

(3.5)

Here, $y_{obs,I}$ and $y_{calc,}$ are displaying the intensity at ith point in the observed and calculated patterns, while w_i is the weighing factor at ith point. R_{wp} should be closely monitored with the expected R-factor for best fit, R_{exp} (Eq. 3.6).

$$R_{exp} = \sqrt{\frac{N-P}{\Sigma_{i=1}^{N} w_i y_{obs,i}^2}} \quad (3.6)$$

Here, N is equal to number of data points, while P is number of parameters. Both of these R-factors can be used to calculate a ratio, which in absolute terms can showcase the overall refinement quality, or goodness of fit (Gof).

$$Gof = \frac{R_{wp}}{R_{exp}} \quad (3.7)$$

3.2.2 Space groups

A space group is a symmetry group, a group of all transformations where an object remains invariant, for an object in three-dimensional space. These kinds of transformations are mathematical concepts, referred to as symmetry operations[57, 59]. Although there are many different symmetry operations deployed in physics and chemistry, in crystallography there are usually only two important transformations; *glide* and *screw*. Glide is a symmetry operation involving a mirror plane (creating a mirror image of the object), followed by a translation (movement along an axis) parallel to that plane. Screw is a symmetry operation that involves a rotation around given axis (screw axis), which is followed by translation along the direction of the same axis (Figure 3.8).
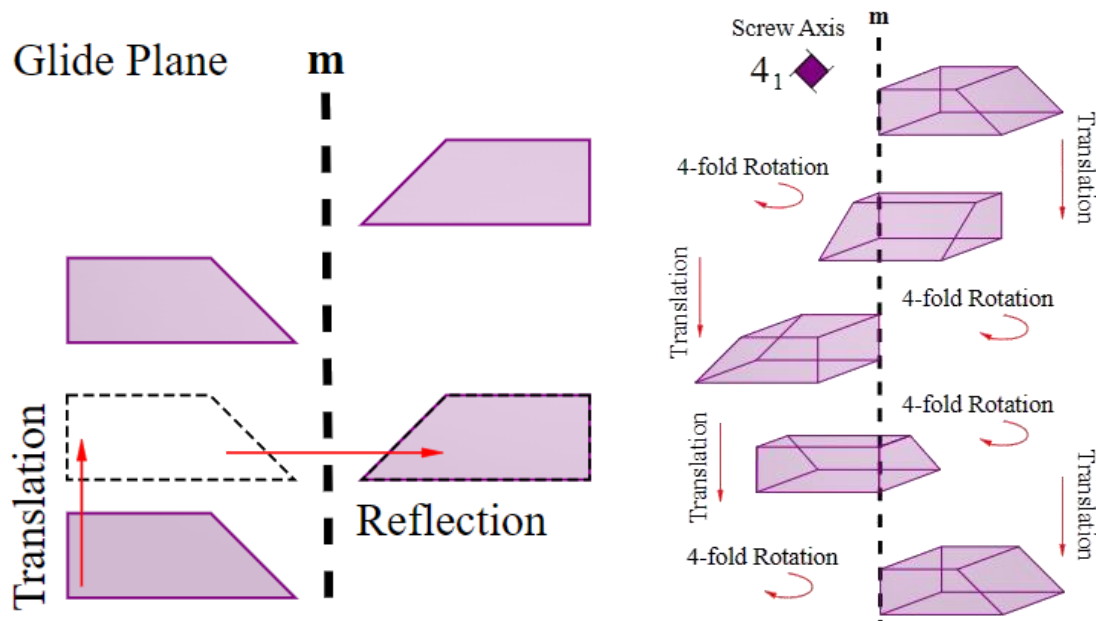
Figure 3.8 - *Visualization of glide plane (**left**) and screw axis (**right**)[57].*

Space groups relate to the seven crystal systems: monoclinic, triclinic, trigonal, tetragonal, hexagonal, orthorhombic and cubic[64]. They are essentially a given crystal system's group of the possible symmetry operations. Space groups that lie in one of these crystal systems are often closely related, and may change when influenced with mechanical stress, heat or introduction of a guest molecule inside a porous material[65]. Such an event is called a phase transition, due to the crystal's changed orientation of the lattice planes. Most of the time, the space groups of highest order, e.g. with most possible symmetry operations, are preferrable due to easier analysis.

3.2.3 Sequential refinement

Sequential refinement has been used to closely inspect the changes made between fits for every scan number. It is a computational technique where datasets are put under similar conditions and models[66]. In the context of PXRD, instead of the usual method (batch refinement), where a single configuration is used for a range of scans, every scan now gets its own configuration when using sequential refinement. It is not a widely used technique, but can nevertheless give an additional insight into subtle differences between each scan, as they progress towards the next phase.

4.Experimental Methods

All synthesis of the materials was done by utilizing the solvothermal method. The procedures were based on the one described in previous work[39,41,48], but here only those with increased dosages will be presented. Other experiments were based exactly on the procedures described in previous work, as to facilitate building a large enough sample out of multiple smaller ones. The concentration of scaled-up solutions remained consistent with those described prior.

4.1 Synthesis of $Cu_2(abdc)_2(dabco)$

The concentration was set to 0.05 M for $Cu(NO_3)_2 \cdot 2.5H_2O$ and H_2abdc, and 0.15 M for dabco. $Cu(NO_3)_2 \cdot 2.5H_2O$ (0.698 g, 3.0 mmol) and H_2abdc (0.543 g, 3.0 mmol) were transferred to a large Teflon inlet (125 mL). DMF (60 mL) was added to the inlet, which resulted in green solution. The solution got a slightly more bluish hue with more DMF. The mixture was stirred for 10 minutes. While still stirring, DABCO (1.010 g, 9.0 mmol) was added, which gave a green suspension. The Teflon inlet was transferred to a steel autoclave which was put in a pre-heated oven (383 K) for approximately 24 h.

4.1.1 Treatment under inert atmosphere

The first three experiments with this compound were done under inert conditions to confirm whether it made any difference. After sufficient cooling of the autoclave, the solid, dark green product was quickly transferred into a Schlenk filter funnel, which was already connected to an operating tubing system with argon-rich environment (Schlenk line). It was washed with roughly 80 mL of DMF and finally left under vacuum for 24 h to dry. Before drying, a fraction of a sample was taken for the PXRD measurement. The dry sample was then moved to a glovebox, where it got transferred to a sample holder equipped with a Cu-nano filter cap. It was then pre-treated and its porosity was then measured.

4.1.2 Standard treatment procedure

After sufficient cooling of the autoclave, the product was filtered and washed with roughly 80 mL of DMF. A fraction of the sample was taken for PXRD measurements. It was left to dry for 2 h before transferring into a sample holder equipped with a Cu-nano filter cap. It was then pre-treated and its porosity was measured.

In both approaches, the dried product was brightly green in color. The substance was structurally confirmed to be $Cu_2(abdc)_2(dabco)$ by PXRD (yield: 1.110 g). The product was vulnerable to ethanol and moisture.

4.2 Synthesis of $Ni_2(abdc)_2(dabco)$

$Ni(NO_3)_2 \cdot 6H_2O$ (0.872 g, 3.0 mmol) and H_2abdc (0.543 g, 3.0 mmol) were transferred to a large Teflon inlet (125 mL) DMF (60 mL) was added to the inlet, which resulted in a green solution. The mixture was stirred for 10 minutes. Dabco (1.010 g, 9.0 mmol) was then added, which resulted in a green suspension. The Teflon inlet was transferred to a steel autoclave which was put in a pre-heated oven (393 K) for approximately 72 h. The solid product was dark green. After being washed with DMF (80 mL) and filtered in air, the sample was put in a Petri dish to dry. While still moist, a small amount of sample was taken for PXRD measurement. After 2 h, the sample's color was a much brighter green, and some of the powder was transported to an adsorption sample cell equipped with a Cu-nano filter cap. The product was confirmed as $Ni_2(abdc)_2(dabco)$ by PXRD (yield: 1.174 g) and visually under the microscope. The product was vulnerable to ethanol and moisture.

4.3 Low-pressure adsorption measurements

A dry enough sample was transported to a pre-weighed sample cell, equipped with an O-ring and a cap with a Cu-nano filter. It was weighed and was then put on a BELMaster^{TM} pre-treatment station, where it got heated up to 423 K for 18 h (for Ni-ATP) and 393 K for 18 h (for Cu-ATP). The cell was weighed again after pre-treatment. The adsorption measurements were all done with N_2 at 77K, and followed a general procedure that came together with the instrument.

4.4 PXRD measurements

A fraction of the sample was carefully picked up by a spatula and was transported to a specimen holder. With the use of the spatula, the sample was gently smeared in the center of the holder, until the surface was visually flat. The sample was kept moist with DMF, which was dosed in a form of 1-2 droplets. The XRD pattern was measured on a Bruker[TM] instrument, with a 4 min. beamtime.

4.5 Structure determination of synchrotron samples

The patterns that will be the focus of this paper have been measured on synchrotron and are otherwise unrelated to both of the synthesis described above[48]. $M_2(abdc)_2(dabco)$ was synthesized according to the literature, reported prior [1]. The sample, after washing and filtration, was dried in dynamic vacuum to remove any traces of the solvent from the pores. It was then radiated with monochromatic light with the wavelength of 0.73074 Å at steadily increasing temperature, provided by a blower. The usable angular range was 2θ = 1.8– 28.7°. The entire procedure was done by utilizing Topas 5 software together with jEdit which was used to create necessary input files. Pictures of the structure shown throughout the thesis were achieved using Diamond 4 and taken from a related work on PXRD curriculum. Plots have been made and refined in Origin. The procedure described in section *3.2.1* was then followed.

5.Results

The synthesized crystals possess a needle-like shape and are a varying shade of green. Under the microscope, $Ni_2(abdc)_2(dabco)$ are seen as homogenous crystals, light-green in color, with well-defined crystalline structure, as well as not too many impurities (best ones reach purities of 98-99%). Impurities were observed to be brown or dark-yellow amorphous solids. The crystals' size is likely in the range of micrometers; thus, the sample appears as a fine powder for a naked eye (Figure 5.1). $Cu_2(abdc)_2(dabco)$ was of a much darker green color and was less crystalline. Both compounds have been evacuated for any solvent, resulting in a weight loss of roughly 32%, which is notably higher than previously reported (roughly 20%)[48]. After pre-treatment, samples were measured with low-pressure adsorption apparatus to determine their pore volume and surface area. Finally, a part of wet sample (roughly 10% of the total sample weight) was taken and measured with PXRD.
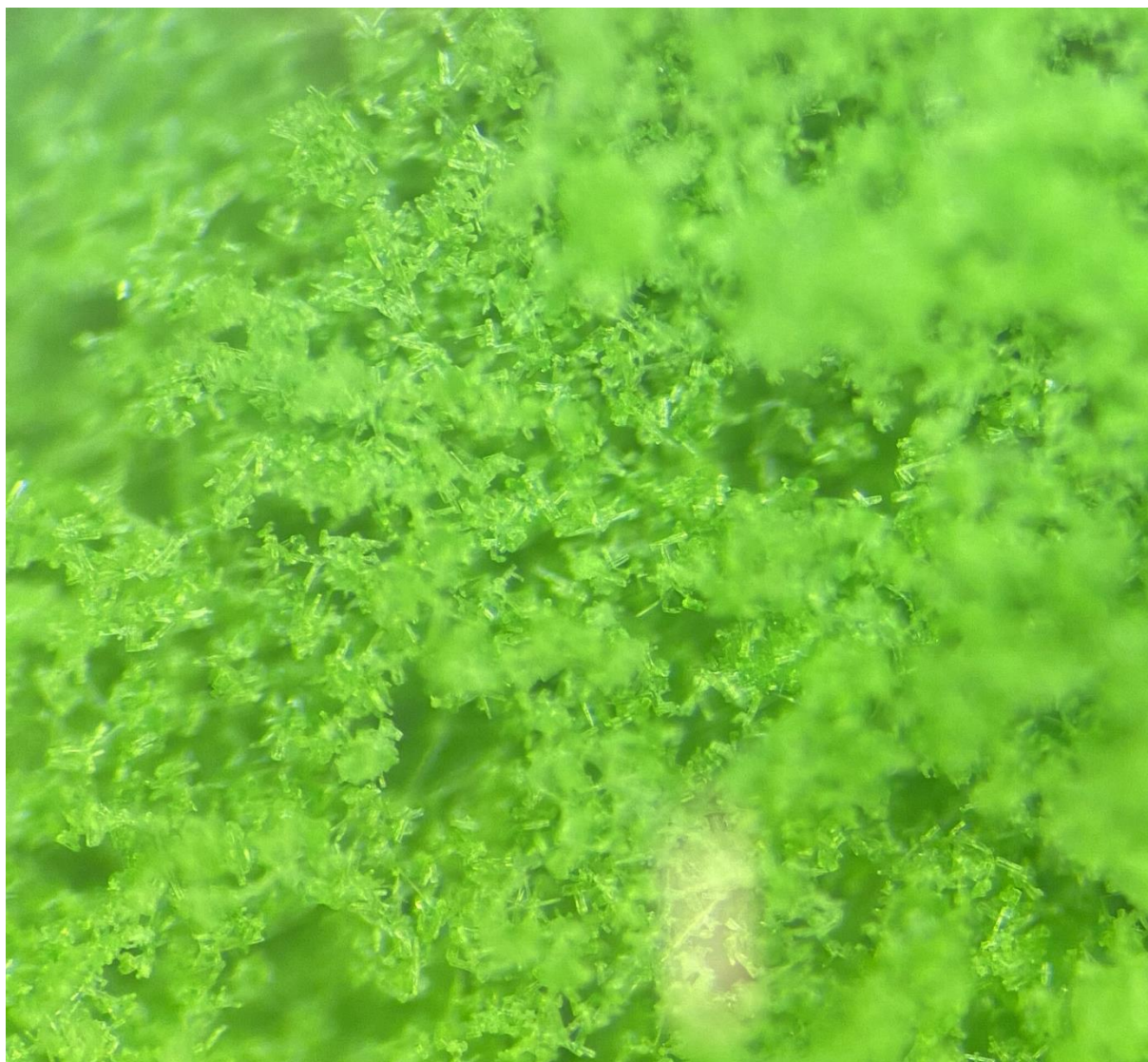
Figure 5.1 - Image of solvated Ni$_2$(abdc)$_2$(dabco) crystals, taken by an ordinary camera through lens of the microscope. The light-yellow spot is just the reflection of light. No impurities in sight.

5.1 Low-pressure adsorption measurements of synthesized samples

Adsorption of both samples revealed worse results, compared to those previously reported[[40,41,48]] (Figures 5.2 and 5.3). The best total pore volume (at *p/p$_0$* = 0.500) and BET surface area for Ni$_2$(abdc)$_2$(dabco) sample was 0.70 cm^{3}g^{-1} and 1775.7 m^{2}g^{-1} respectively, which was achieved by swaying away from standard procedure. It is better than previously reported Ni$_2$(abdc)$_2$(dabco)[48] by roughly 12 %. For the scaled-up synthesis, the total pore volume was 0.38 cm^{3}g^{-1} and specific surface area was 947.7 m^{2}g^{-1}, which is, interestingly, roughly half of the results for the best sample given by ordinary synthesis.

For scaled-up $Cu_2(abdc)_2(dabco)$, the surface area reached 896.67 m^2g^{-1} and total pore volume was 0.36 cm^3g^{-1}, which is also lower, compared to 976 m^2g^{-1} and 0.40 cm^3g^{-1} [48], although the change is much smaller. The plot shown below was taken of a sample, treated under argon.
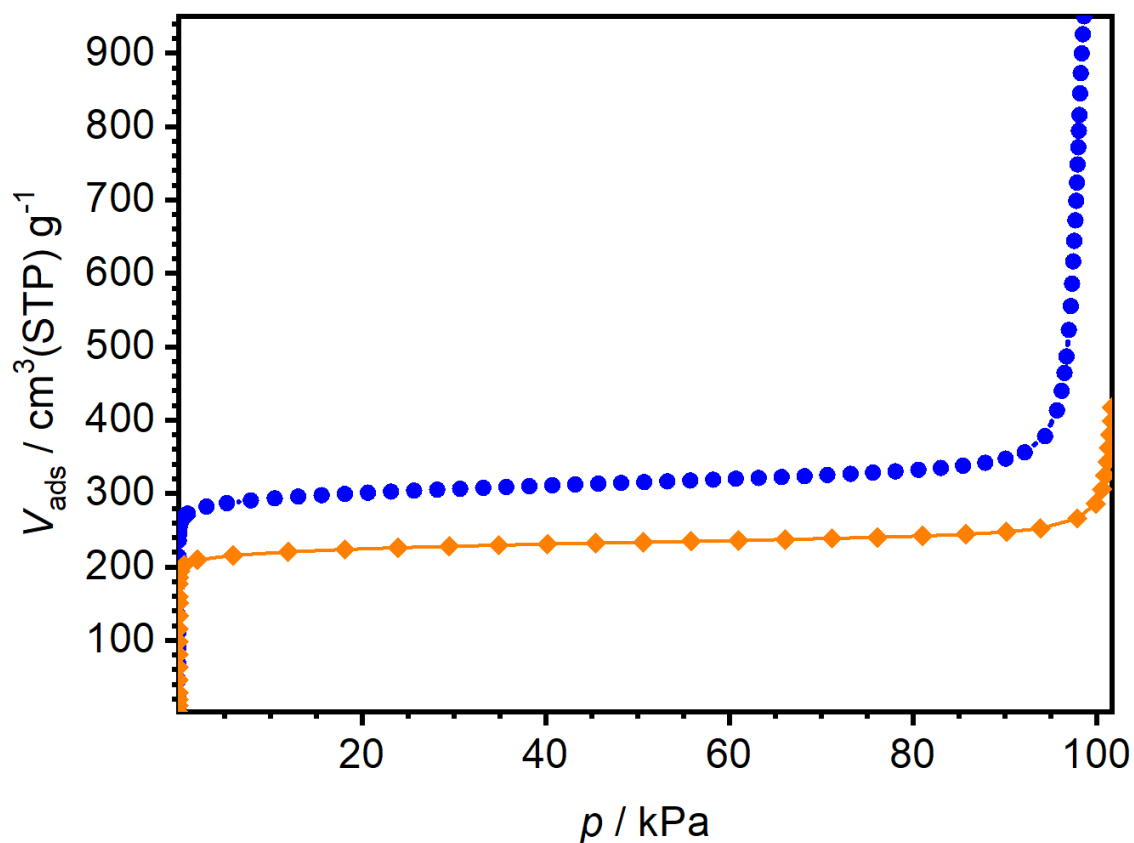
Figure 5.2 - *Isotherm plots comparison for $Cu_2(abdc)_2(dabco)$. Orange diamonds are for the sample from this thesis (scaled-up synthesis, inert atm.), blue dots are from previously reported work[48].*
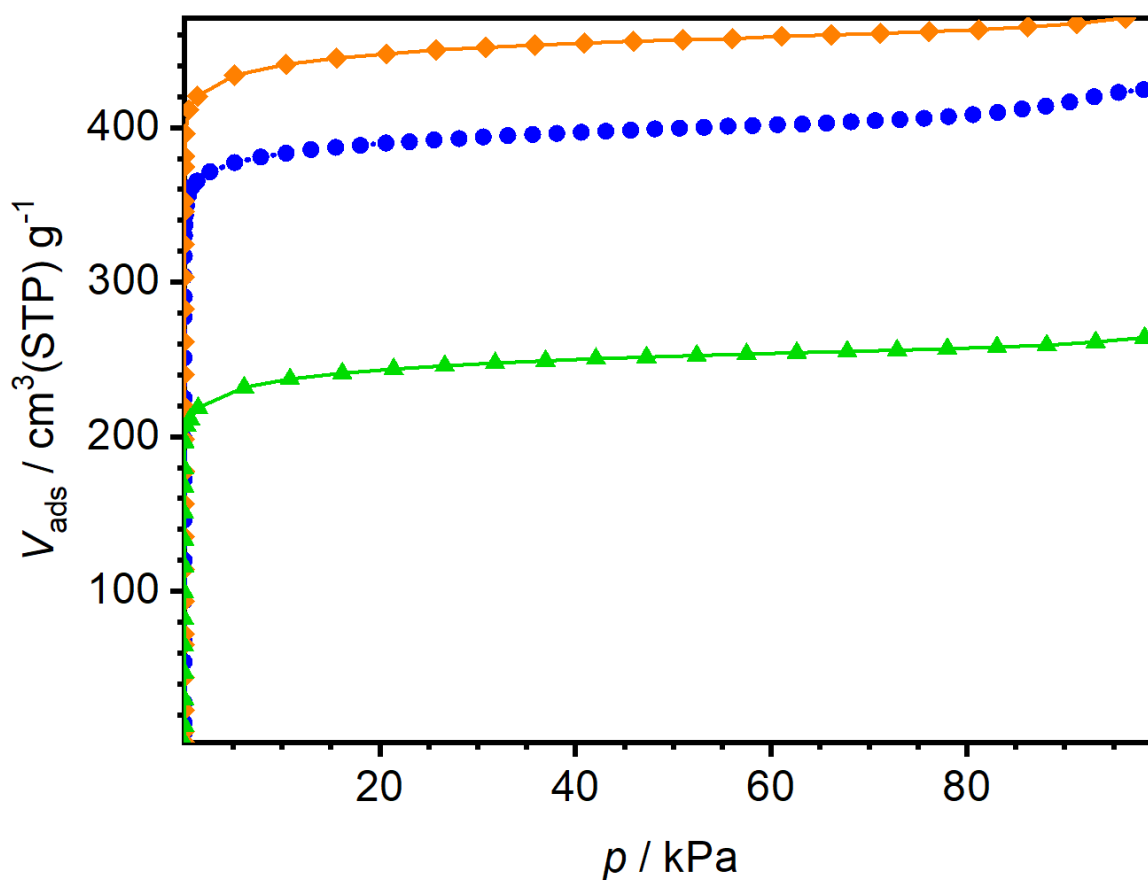
Figure 5.3 - *Isotherm plots comparison of Ni$_2$(abdc)$_2$(dabco). Orange diamonds are from this thesis (ordinary procedure), blue dots are from previously reported work [48], green triangles are from this thesis (scaled-up synthesis)*

The experiments where samples were carefully treated in inert conditions did not bring any improved results. It was, however, observed that Cu$_2$(abdc)$_2$(dabco) is very sensitive towards the concentration of the involved reactants. This trait is likely to be translated to the other three analogues as well.

5.2 PXRD characterization of synthesized samples

The best patterns of both $Cu_2(abdc)_2(dabco)$ and $Ni_2(abdc)_2(dabco)$ were analyzed following the steps described in section *3.2.1*. However, the structure determination and Rietveld refinement were not used, as the data was not of high enough quality. Thus, only indexing and Pawley method were used, in order to observe whether the synthesized materials possessed characteristics present in previously reported samples[41,48], like for instance, a consistent space group. No other peaks belonging to other structures were observed (Figures 5.4 and 5.5).
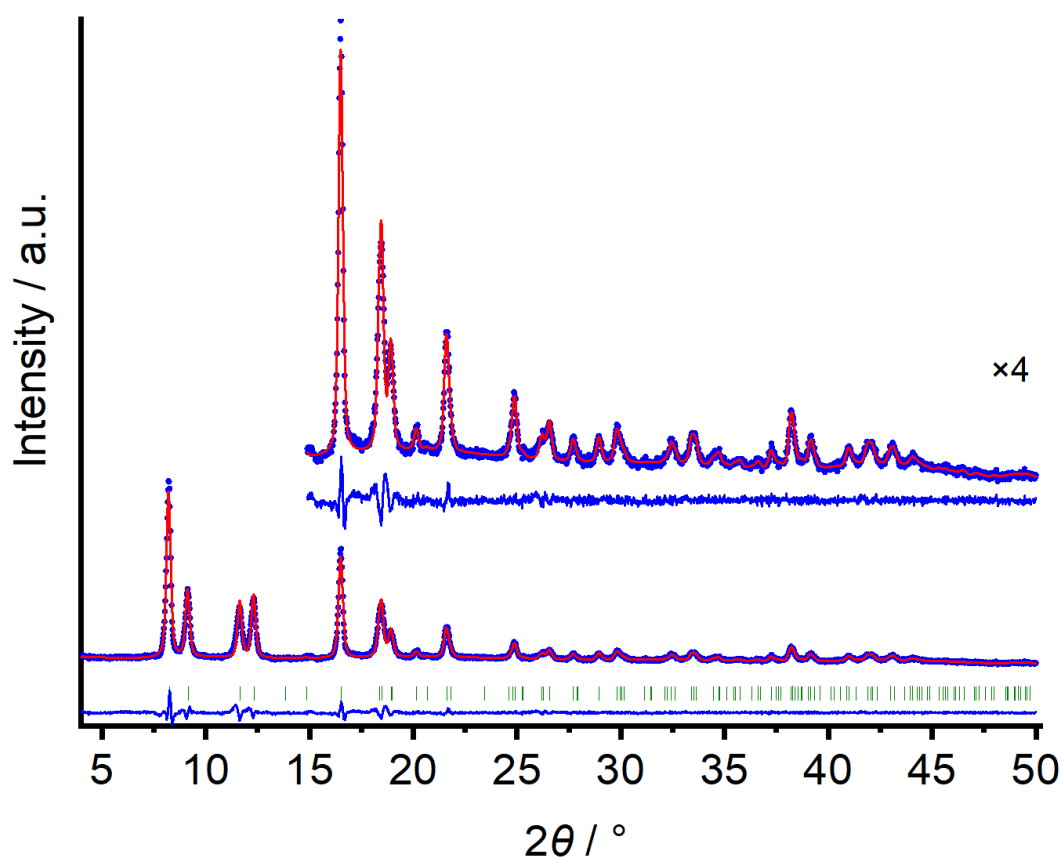
***Figure 5.4** - Pawley plot of Cu₂(abdc)₂(dabco) (scaled-up synthesis). Blue dots are the original data, red line show calculated plot, blue line underneath the plot is the difference between calculated and observed patterns, green ticks show reflection positions. The upper plot is the magnified part of the main plot along with the magnification factor.*
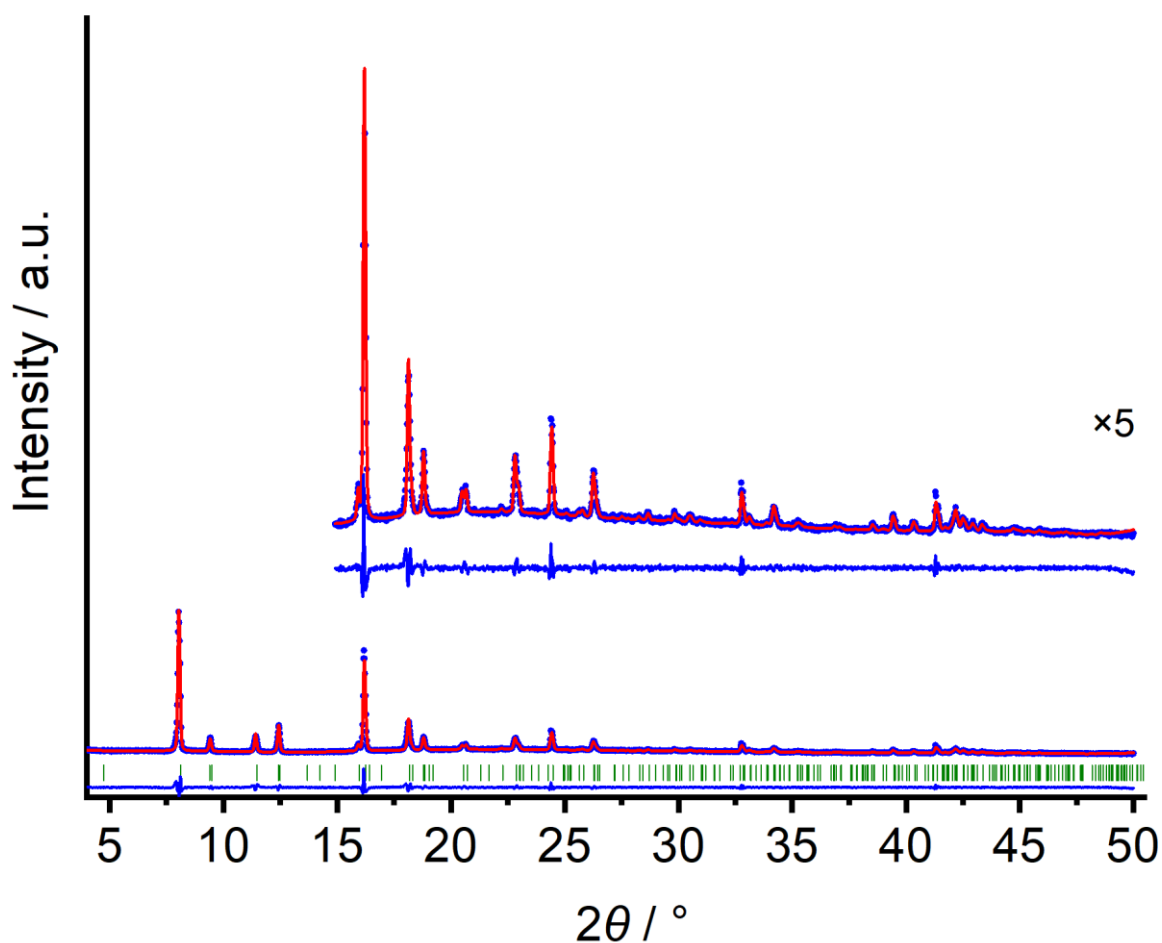
Figure 5.5 - *Pawley plot of Ni$_2$(abdc)$_2$(dabco) (scaled-up synthesis). Blue dots are the original data, red line show calculated plot, blue line underneath the plot is the difference between calculated and observed patterns, green ticks show reflection positions. The upper plot is the magnified part of the main plot along with the magnification factor.*

5.3 PXRD of synchrotron data

The synchrotron data was gathered at Swiss Norwegian Beamline (BM01) at ESRF in 2021[48]. The samples were measured in N$_2$ atmosphere, with a heat blower continuously elevating the temperature from 293 K to 440 K, and in a beam of X-rays measuring 0.73074 Å in wavelength. The samples generally showed good quality diffraction patterns and relatively clear transition between phases, with some key discrepancies (see 6. Discussion).

5.3.1 Contour plots

Four contour plots were constructed with the data provided, depicting $M_2(abdc)_2(dabco)$ (M = Co, Ni, Cu, Zn). This type of plot displays compound's changes in structure due to temperature increase as a shift in peak position Different peak positions will naturally dictate different lattice parameters, which results in a different space group. These phases can (for the most part) be observed simply by looking at the plot. The plots also come with regular PXRD plots for each of the phase, for easier comparison (Figures 5.6-5.9). The color coding in each of the plot points towards relative intensities of the reflections, with blue being the weakest (background) through green, to red (highest intensity).
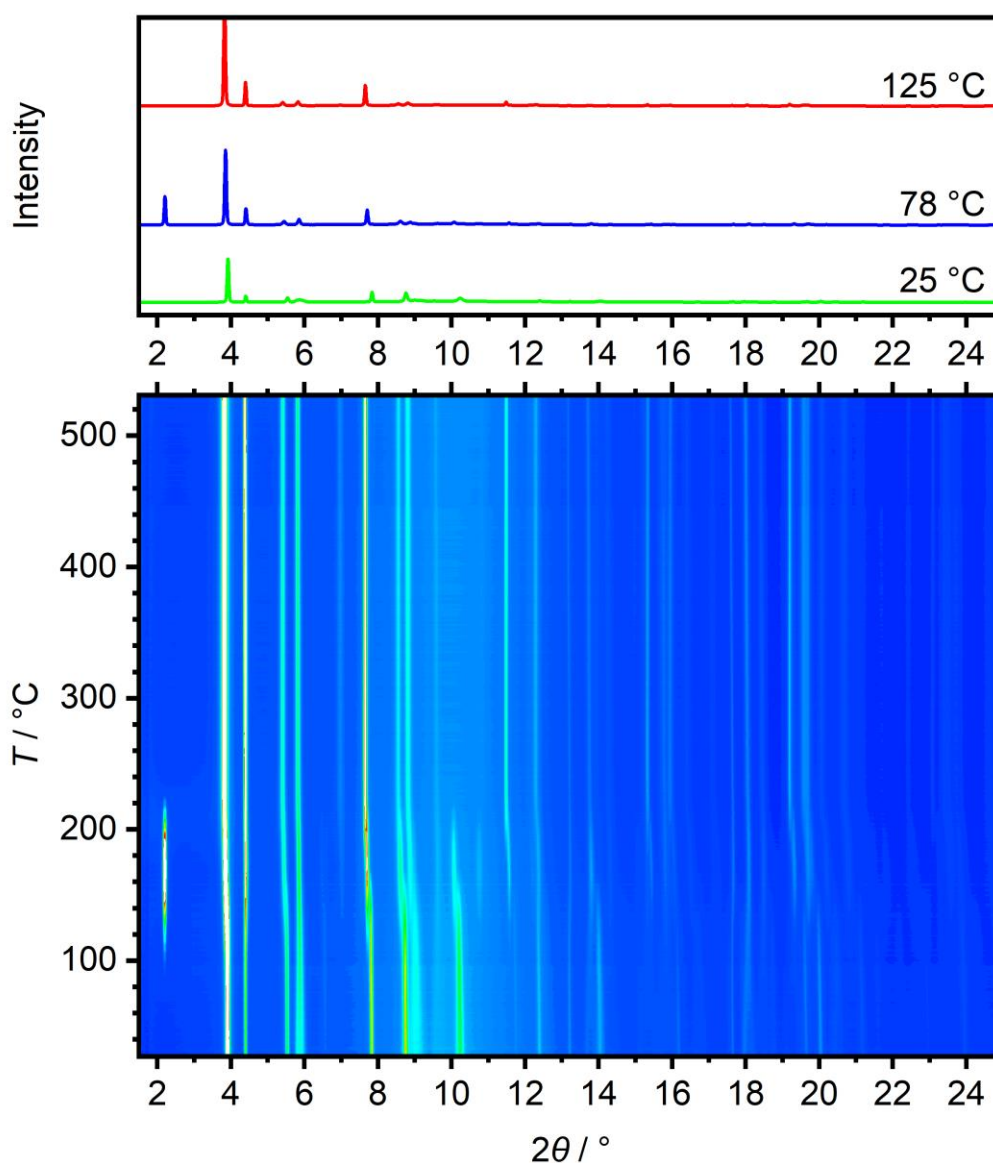
Figure 5.6 - *Contour plot for Co₂(abdc)₂(dabco)*
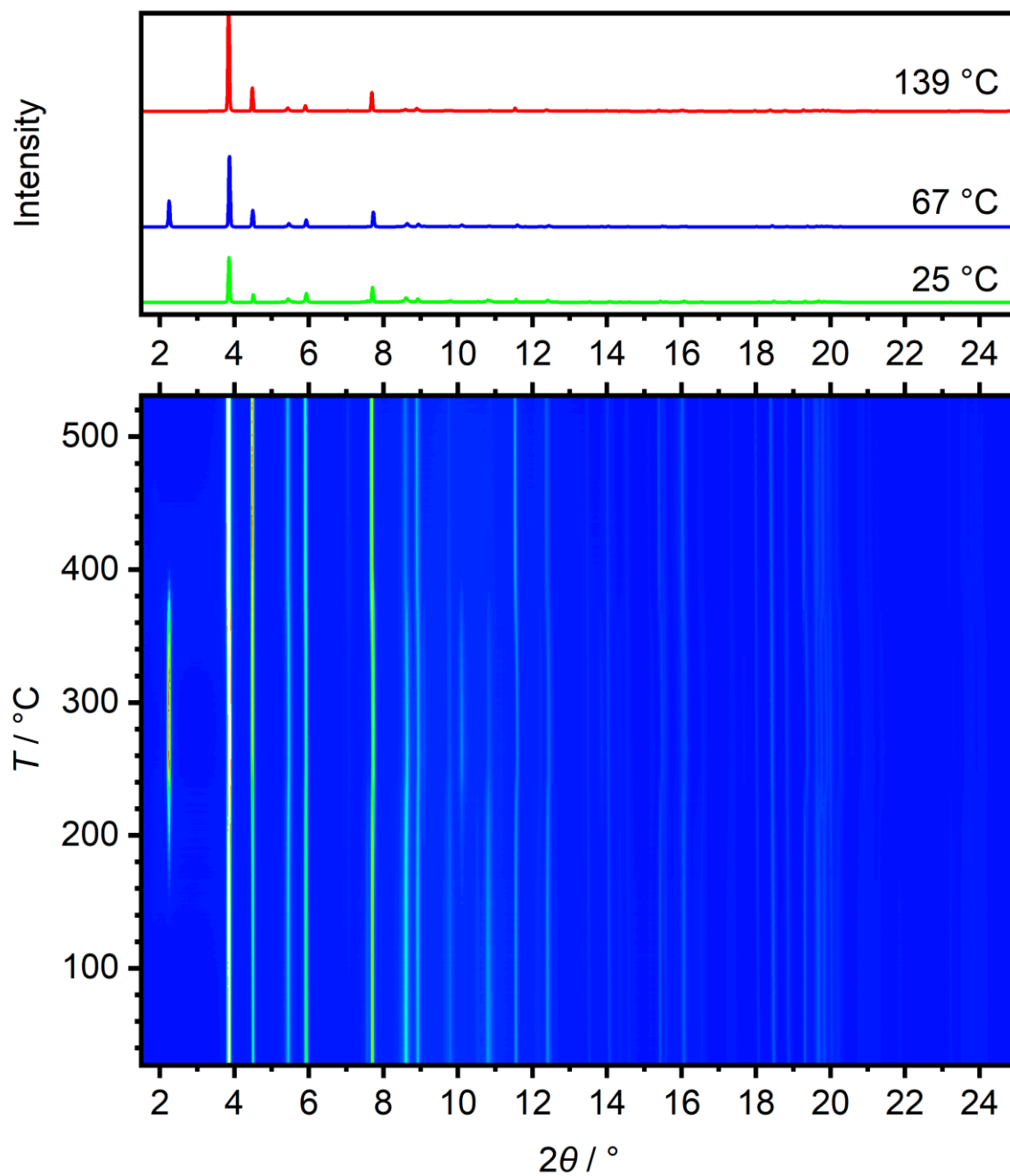
Figure 5.7 - *Contour plot for Ni$_2$(abdc)$_2$(dabco)*
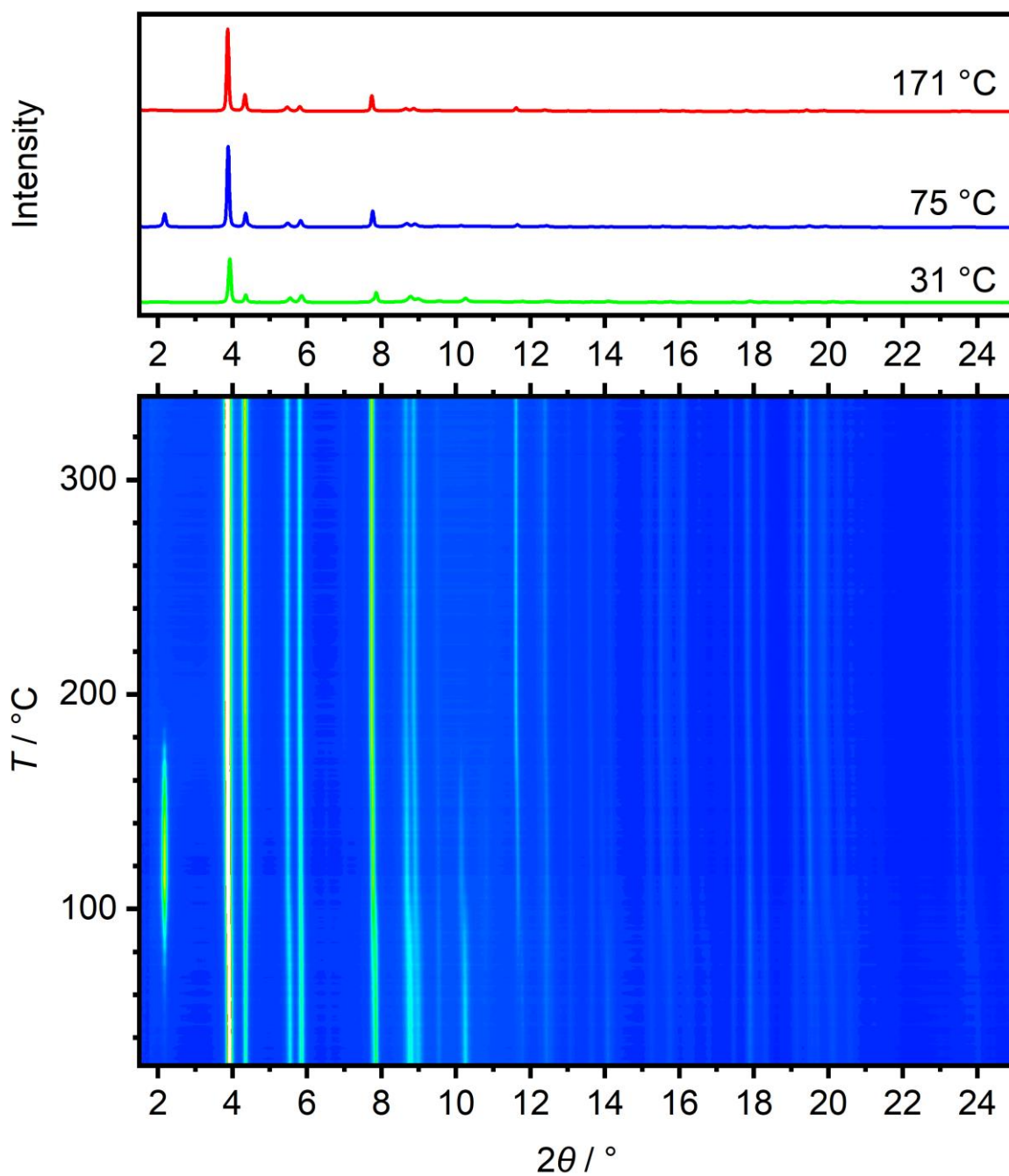
Figure 5.8 - Contour plot for Cu$_2$(abdc)$_2$(dabco)
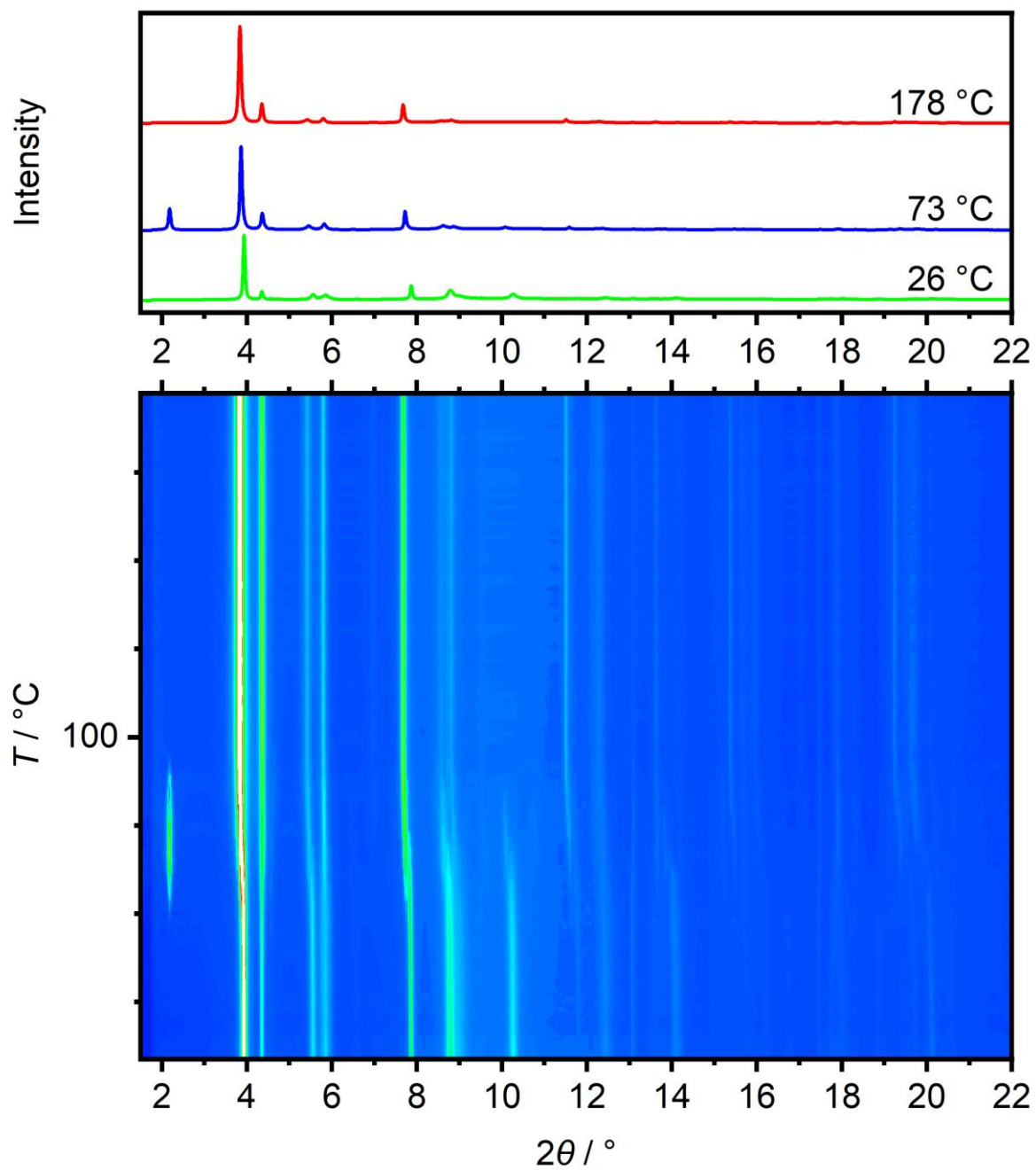
Figure 5.9 - *Contour plot for Zn$_2$(abdc)$_2$(dabco)*

The temperature ranges for each phase and its transition for all four $M_2(abdc)_2(dabco)$ analogues have been noted in Table 5.1.

Table 5.1 - *Temperature ranges (in °C) for each phase for $M_2(abdc)_2(dabco)$ (M = Co, Ni, Cu, Zn).*

Compound	Phase 1	Phase 1+2	Phase 2	Phase 2 pure*	Phase 2+3	Phase 3 (empty)	Phase 3 decomposition
Co-ATP	24.8-48.4	47.4-77.8	47.4-99.1	77.5	90.6-99.1	99.1-269.5	269.5-291.0
Ni-ATP	24.9-46.1	46.1-68.1	46.1-99.4	67.4	73.6-99.4	99.4-365.3	365.3-438.8
Zn-ATP	26.3-52.8	52.8-75.3	52.8-97.1	72.9	81.1-97.1	97.1-178.7	178.7-260.4
Cu-ATP	30.8-45.5	45.5-62.1	45.5-98.6	69.9	80.9-98.6	98.6-175.5	175.5-253.7

Phase 2 pure displays the point at which data for phase 2 was taken, as the peaks were the most prevalent there

5.3.2 Characterization

The analysis closely followed the procedure detailed in section *3.2.1*. Relevant peaks were first identified, both automatically and manually. Indexing was then performed, with many solutions being fairly peculiar, due to samples' unideal background reflections. All of the phases possessed a tetragonal crystal system. Full profile matching resulted in pretty good R_{wp} , which ranged from 1.7 % to 6.3 % across all three phases (Table 5.2). Although all crystallized in a tetragonal crystal system, $Ni_2(abdc)_2(dabco)$ would do so in a P4/nbm space group, which was surprising. The other analogues would crystallize in the predicted I4/mcm space group[41,48,67]. Phase 2 displayed a consistent behavior, where all analogues transitioned temporarily to P4/nbm with *c* ranging closely within 19.2 Å. Phase 3 remains consistent with previous work[48] alongside other reports[25,39,41,42].

Table 5.2 - *Crystallographic data for each of the M$_2$(abdc)$_2$(dabco) phases (M = Co, Ni, Cu, Zn).*

Metal	Co	Ni	Cu	Zn
Phase 1				
Space group	I4/mcm	P4/nbm	I4/mcm	I4/mcm
a / Å	15.139760	15.402968	15.090046	15.075407
b / Å	15.139760	15.402968	15.090046	15.075407
c / Å	19.054795	9.311709	19.256851	19.256373
V / Å³	4367.594	2209.216	4384.967	4376.355
Rwp / %	5.1	3.8	3.3	1.9
Phase 2				
Space group	P4/nbm	P4/nbm	P4/nbm	P4/nbm
a / Å	15.392010	15.349644	15.259815	15.351460
b / Å	15.392010	15.349644	15.259815	15.351460
c / Å	19.031080	18.673388	19.277900	19.229168
V / Å³	4508.729	4399.666	4489.089	4531.687
Rwp / %	1.9	3.6	1.9	2.5
Phase 3				
Space group	P4/mmm	P4/mmm	P4/mmm	P4/mmm
a / Å	10.960492	10.915664	10.835820	10.921763
b / Å	10.960492	10.915664	10.835820	10.921763
c / Å	9.533359	9.354283	9.678881	9.617217
V / Å³	1145.265	1114.579	1136.446	1147.189
Rwp / %	4.1	4.2	6.3	3.0

Although no other peaks belonging to other crystal structures were observed, some patterns would display a certain degree of poorly fitted peaks. This is especially relevant for Co-analogue with a poorly fitted peak at around 2θ = 13.0° (Figure 5.10). Other fits do not appear to have any discrepancies (Figures 5.11 and 5.12).
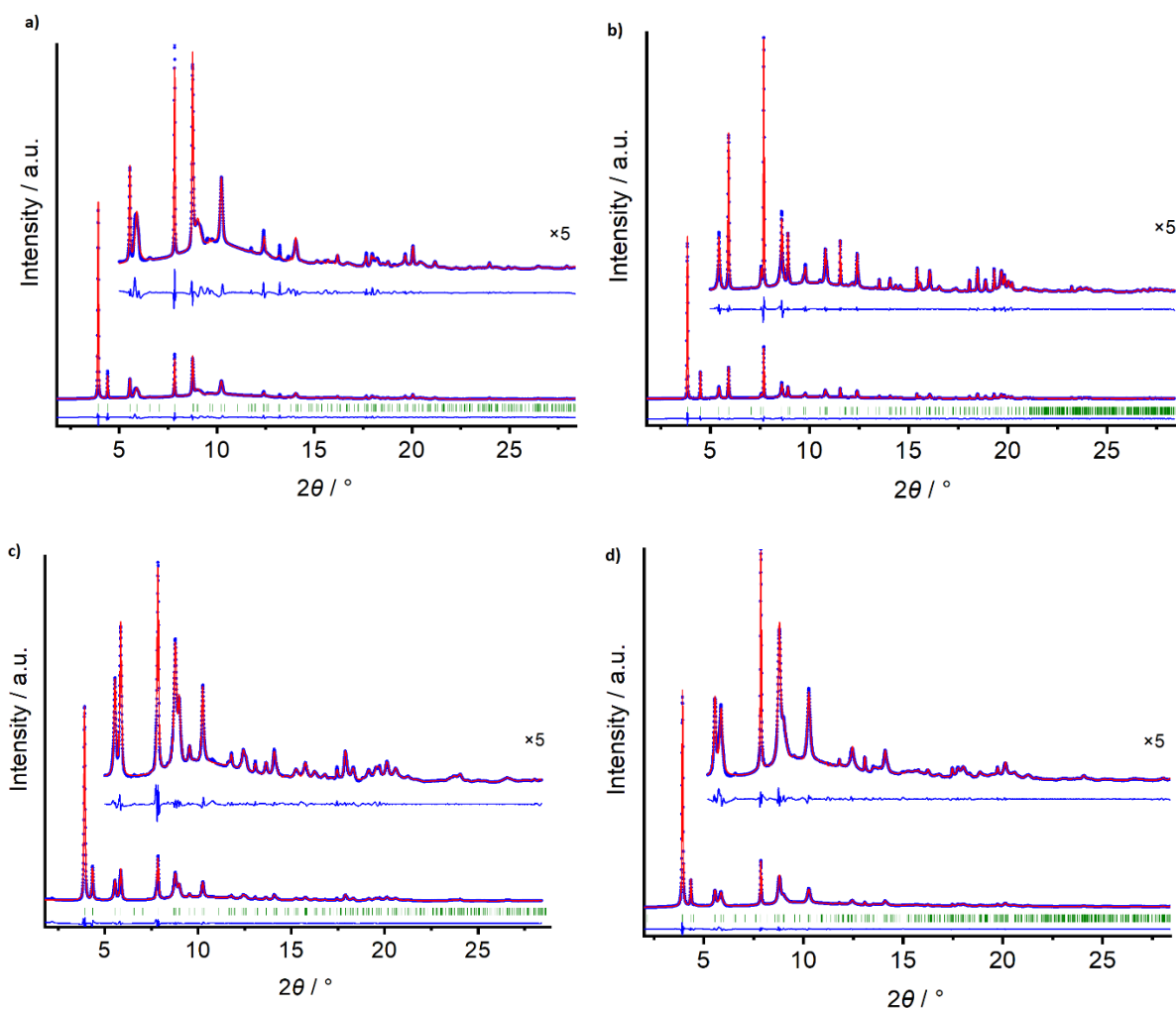
Figure 5.10 - *Pawley plots for Phase 1 for **a)** Co$_2$(abdc)$_2$(dabco), **b)** Ni$_2$(abdc)$_2$(dabco), **c)** Cu$_2$(abdc)$_2$(dabco) and **d)** Zn$_2$(abdc)$_2$(dabco) respectively. Blue dots are the original data, red lines show calculated plot, blue line underneath the plots is the difference between calculated and observed pattern, green ticks show reflection positions. The upper plot is the magnified part of the main plot along with the magnification factor.*
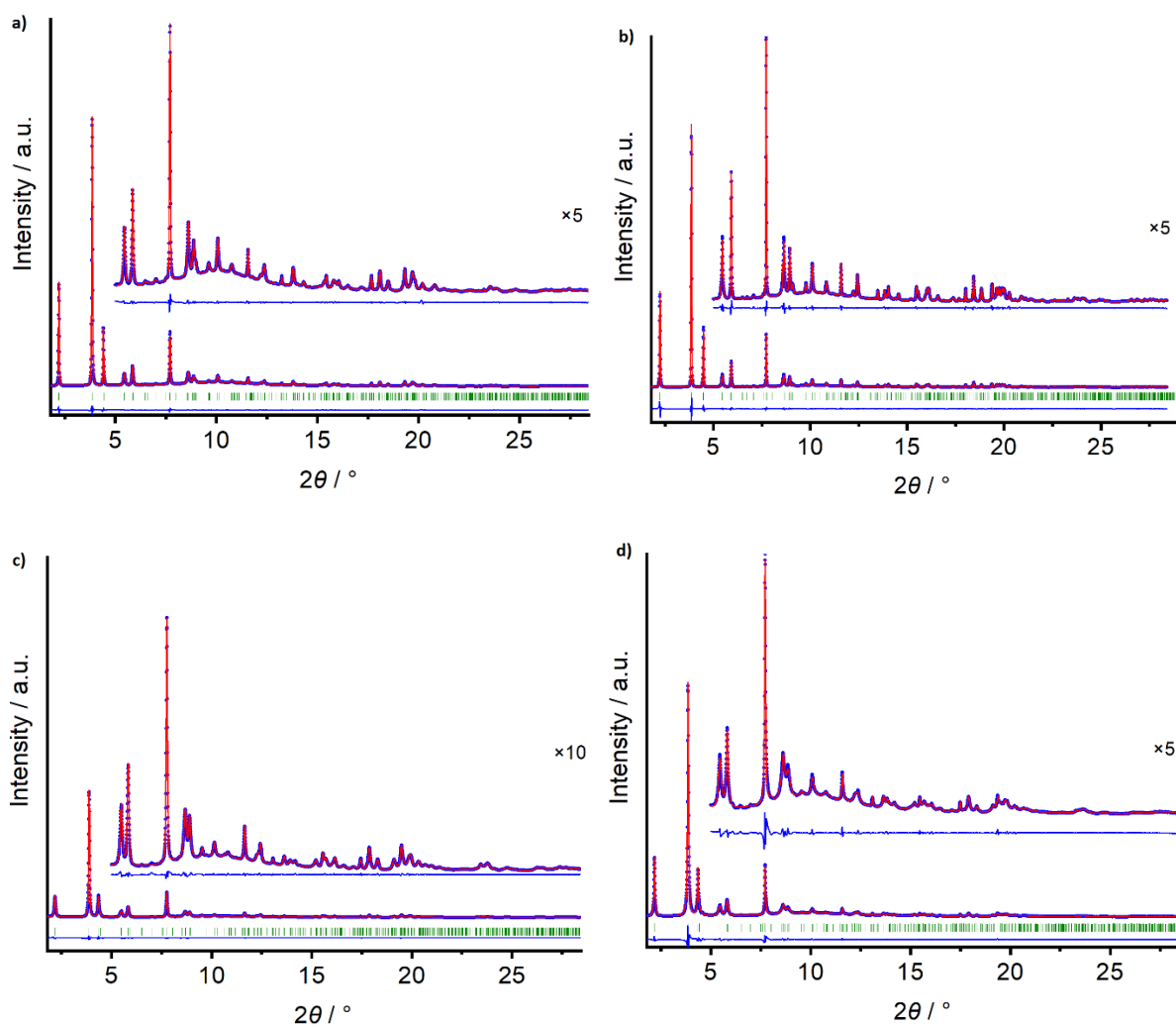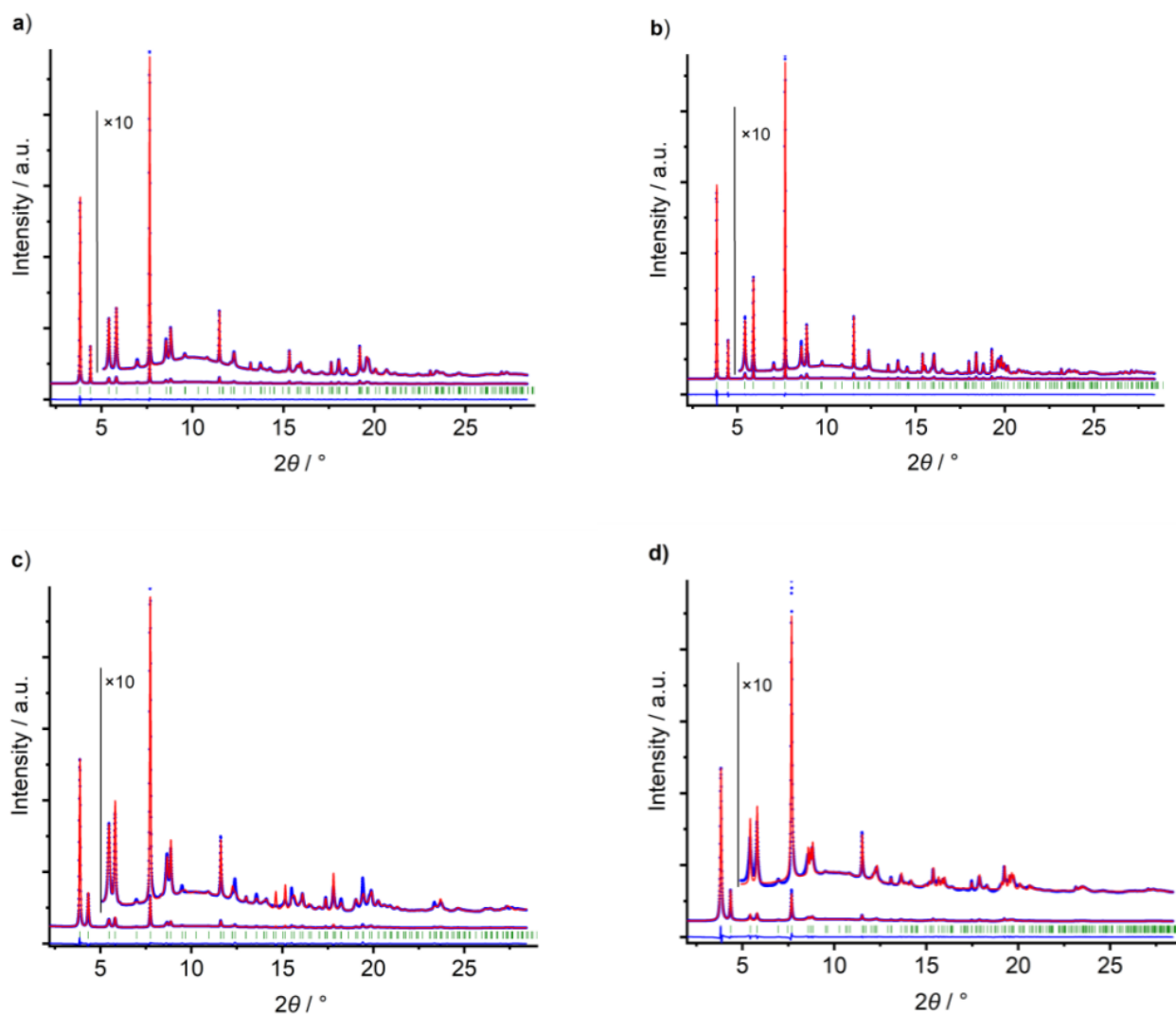
Figure 5.11 - Pawley plots for Phase 2 for a) Co₂(abdc)₂(dabco), b) Ni₂(abdc)₂(dabco), c) Cu₂(abdc)₂(dabco) and d) Zn₂(abdc)₂(dabco) respectively. Blue dots are the original data, red lines show calculated plot, blue line underneath the plots is the difference between calculated and observed pattern, green ticks show reflection positions. The upper plot is the magnified part of the main plot along with the magnification factor.

Figure 5.12 - *Pawley plots for phase 3 taken directly from previous work [48], for **a)** Co$_2$(abdc)$_2$(dabco), **b)** Ni$_2$(abdc)$_2$(dabco), **c)** Cu$_2$(abdc)$_2$(dabco) and **d)** Zn$_2$(abdc)$_2$(dabco) respectively. Blue dots are the original data, red lines show calculated plot, blue line underneath the plots is the difference between calculated and observed pattern, green ticks show reflection positions. The upper plot is the magnified part of the main plot along with the magnification factor.*

5.3.3 Sequential refinement

Sequential refinement was performed by running a continuous sequence of scans in Topas 6, via the use of a pre-written script in jEdit. The data was collected and put into Origin, to make final figures (Figures 5.13-5.16). The phases shown were all pure, and their respective temperature ranges can be seen in Table 5.1.
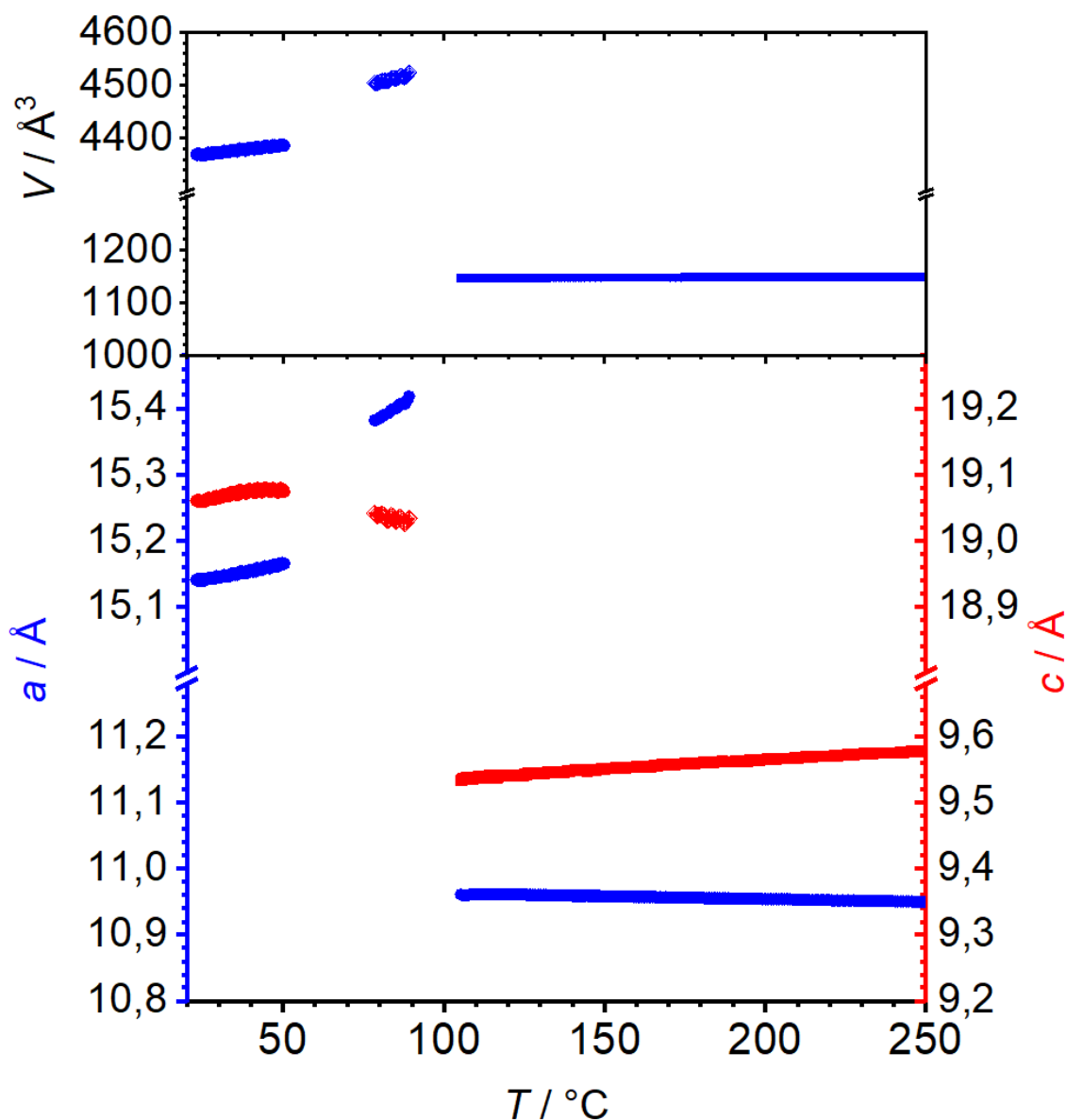
Figure 5.13 - *Results of sequential refinement for $Co_2(abdc)_2(dabco)$ plotted as a function of a/c and T (lower plot). Color coding: blue/red dots = parameters a/c respectively for phase 1, blue/red diamonds = parameters a/c for phase 2, blue/red squares = parameters for phase 3. Upper plot shows the results as function of V and T for each of three phases. Does not include decomposition.*
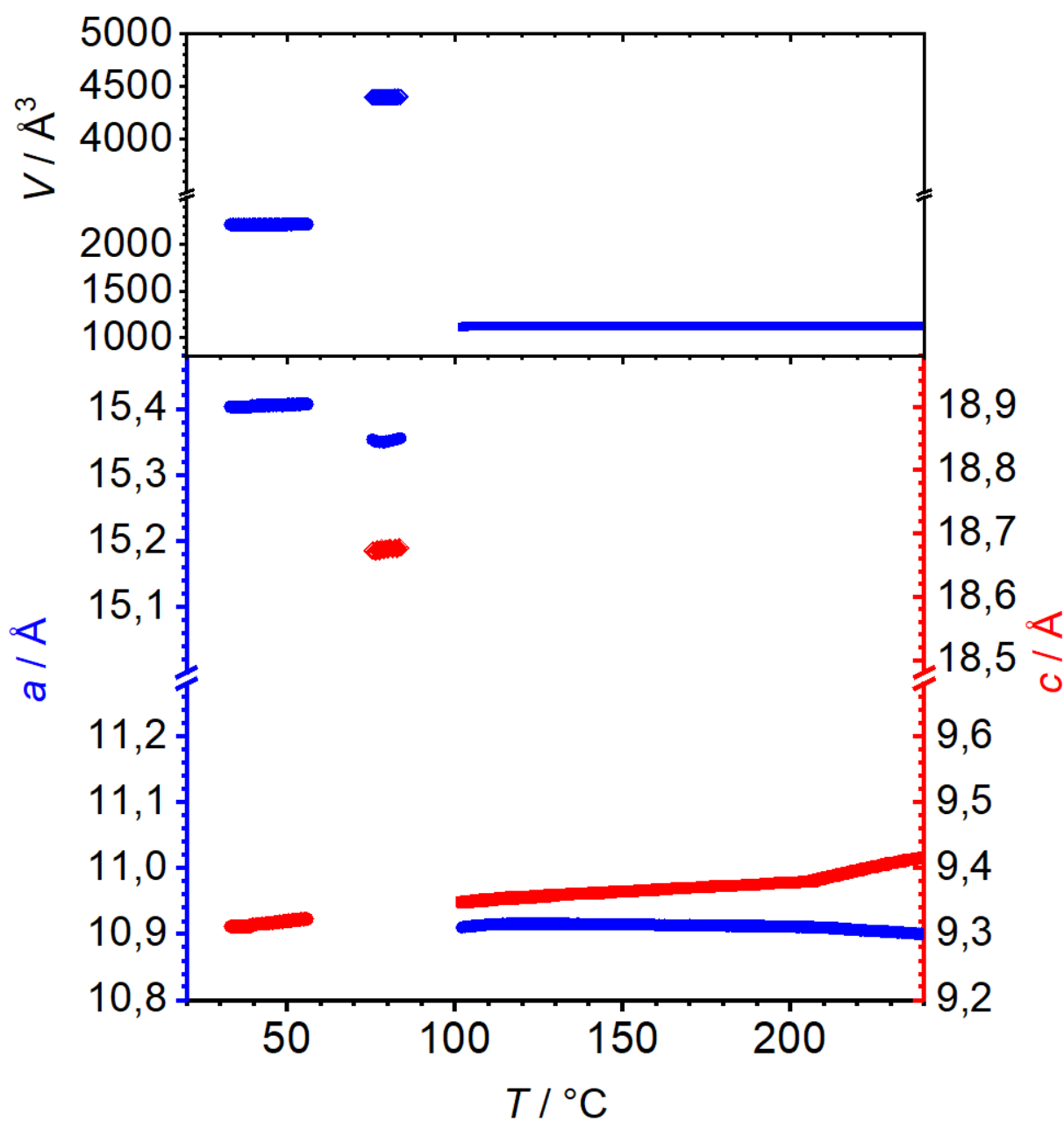
Figure 5.14 - *Results of sequential refinement for Ni₂(abdc)₂(dabco) plotted as a function of a/c and T (lower plot). Color coding: blue/red dots = parameters a/c respectively for phase 1, blue/red diamonds = parameters a/c for phase 2, blue/red squares = parameters for phase 3. Upper plot shows the results as function of V and T for each of three phases. Does not include decomposition.*
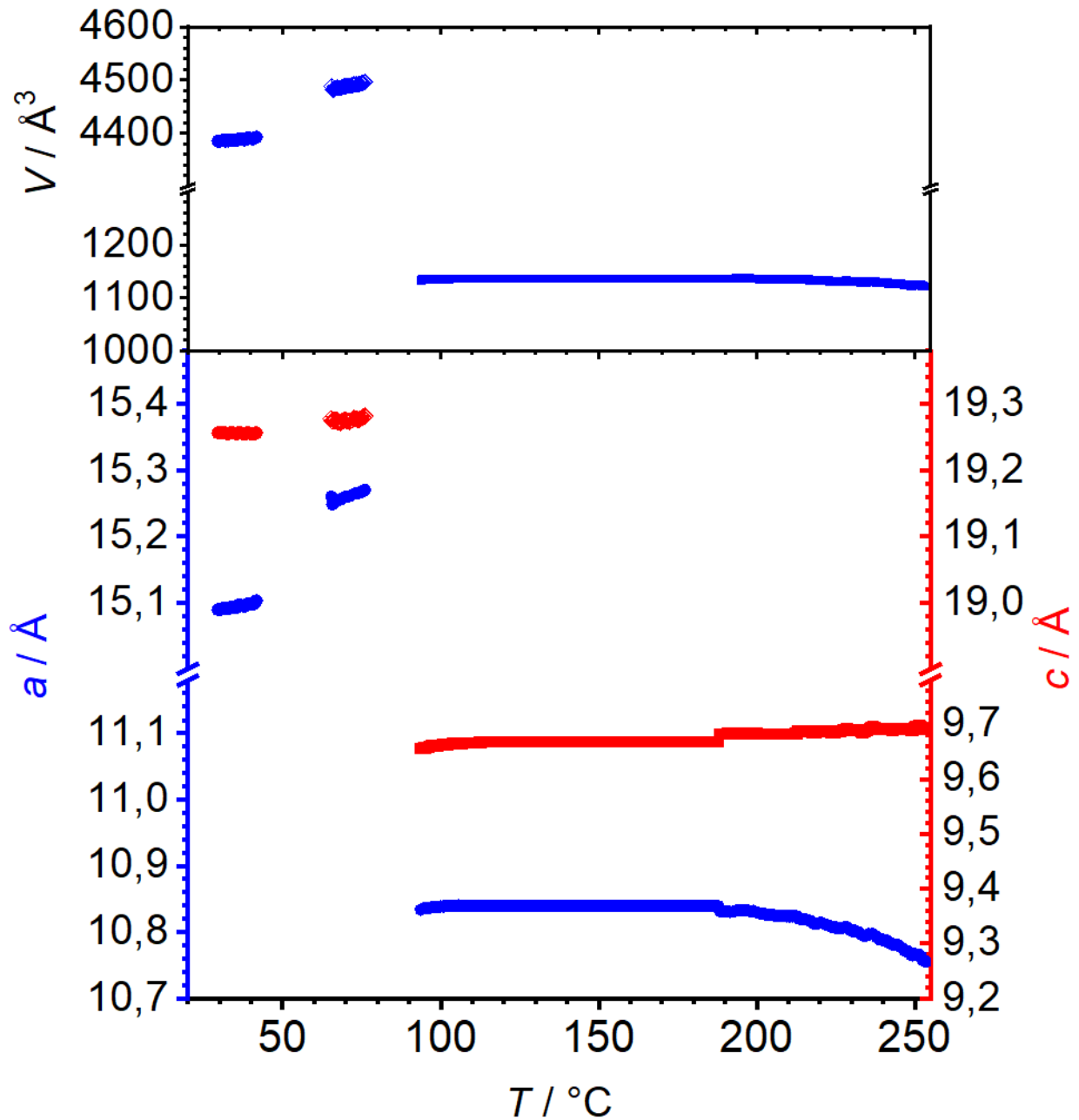
Figure 5.15 - *Results of sequential refinement for Cu₂(abdc)₂(dabco) plotted as a function of a/c and T (lower plot). Color coding: blue/red dots = parameters a/c respectively for phase 1, blue/red diamonds = parameters a/c for phase 2, blue/red squares = parameters for phase 3. Upper plot shows the results as function of V and T for each of three phases. Does not include decomposition.*
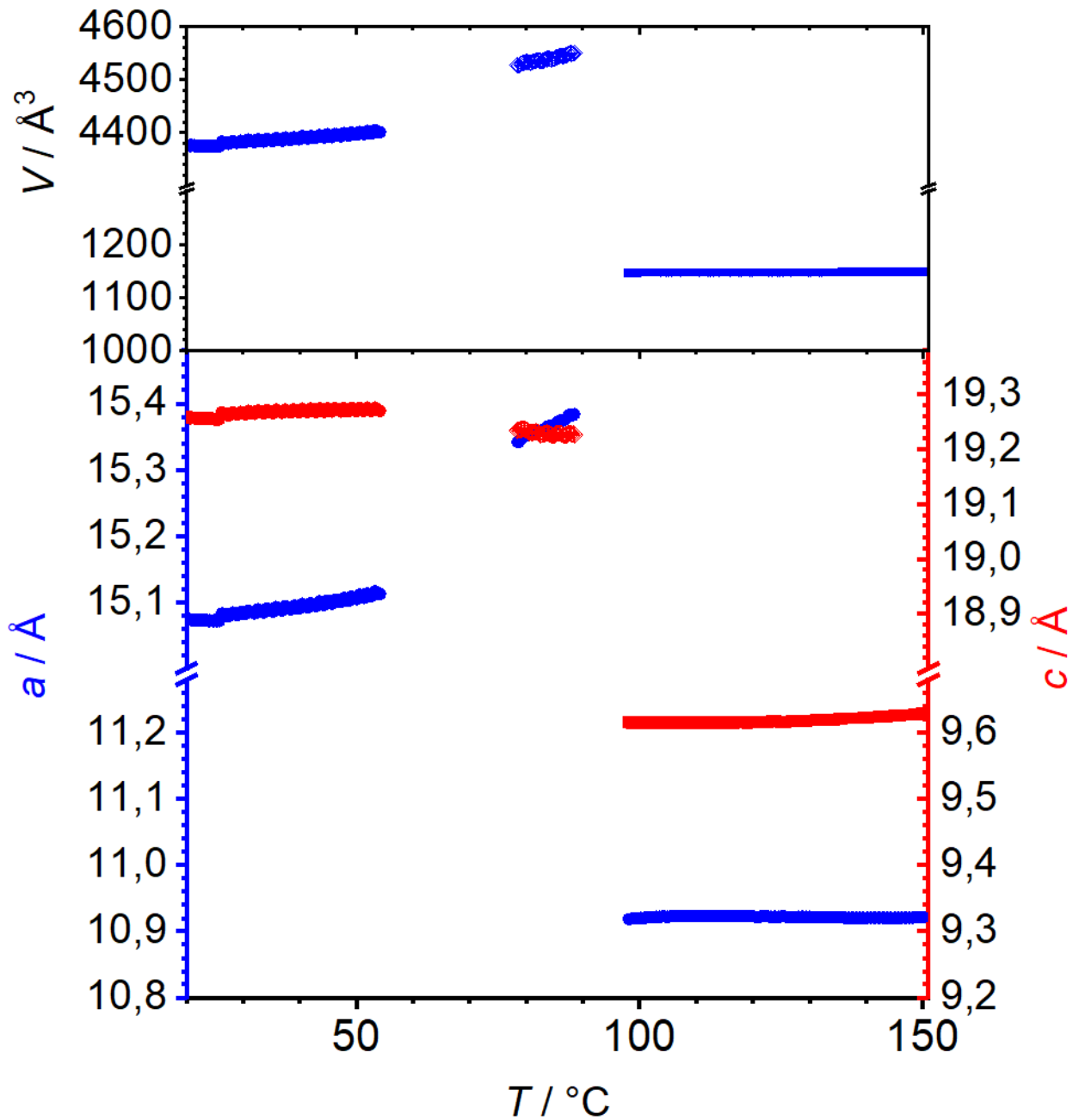
Figure 5.16 - *Results of sequential refinement for Zn$_2$(abdc)$_2$(dabco) plotted as a function of a/c and T (lower plot). Color coding: blue/red dots = parameters a/c respectively for phase 1, blue/red diamonds = parameters a/c for phase 2, blue/red squares = parameters for phase 3. Upper plot shows the results as function of V and T for each of three phases. Does not include decomposition. Phase 3 is incomplete, due to abrupt cut in data.*

6.Discussion

6.1 Comparison of synthesized M$_2$(abdc)$_2$(dabco) with previously reported samples

Although the procedures utilized in the synthesis M$_2$(abdc)$_2$(dabco) were the same as the ones reported previously[41,42,45,48], the results were ultimately a lukewarm success, compared to previous work. It was, however, beneficial nonetheless, as several variables in the solvothermal synthesis method were tested, thus possibly refining the most ideal method for synthesizing M$_2$(abdc)$_2$(dabco). All isotherms were measured with N$_2$ at low pressure with a range of 10^{-3} to 100 kPa and strictly follow a Type I isotherm pattern (Figure 3.3). It was observed that a scaled-up synthesis won't yield a sample of high enough adsorptive capability, even if the overall crystallinity is up to par with the small-scale samples (Figures 5.4 and 5.5). For the scaled-up Cu-analogue the surface area reached 896.67 m^{2}g^{-1} and total pore volume was 0.36 cm^{3}g^{-1}, compared to 976 m^{2}g^{-1} and 0.40 cm^{3}g^{-1} [48]. This is roughly a 9 % decrease, and may not be as severe as for Ni$_2$(abdc)$_2$(dabco) due to procedure being carried under argon. This is creates a possibility that synthesis under inert conditions will yield in texturally better materials[39,48]. However, experiments included scale-up were all affected negatively. Unless new method is designed, a direct increase of reactants, even while maintaining original concentrations[48], should be avoided.

PXRD was taken of solvated samples. Out of possible indexing solutions, Cu$_2$(abdc)$_2$(dabco) and Ni$_2$(abdc)$_2$(dabco) fitted best to I4/mcm and P4/nbm space groups respectively (Figures 5.4 and 5.5) and (Table 6.1). This is in good accordance with the synchrotron data which will be discussed later. This data is, however, only a rough estimate as it is of much lesser quality than that obtained at the synchrotron. It can be easily observed via the provided R_{wp} values.

Table 6.1 - Crystallographic data for synthesized, tetragonal M$_2$(abdc)$_2$(dabco) (M = Cu, Ni)

	Space group	a / Å	b / Å	c / Å	V / Å^3	R_{wp} / %
Cu$_2$(abdc)$_2$(dabco)	I4/mcm	15.2	15.2	19.3	4434.3	5.5
Ni$_2$(abdc)$_2$(dabco)	P4/nbm	15.4	15.4	18.6	4431.1	6.2

There were many experiments involving Ni$_2$(abdc)$_2$(dabco), out of which only few samples had passable adsorption capability[41,48]. It is strange, as for most of them, the PXRD revealed decent fits, with discrepancies occurring almost exclusively at 2θ =16° and 23° (Figure 5.5), where peaks were not ideally fitting to the data obtained from synchrotron.

Additionally, inspection under microscope revealed crystals that were ranging from 90-98% in purity. Most notable and frequent impurity was the yellow, amorphous and non-transparent substance, likely to be a form of shell from which the crystals continued their growth. Another notable impurity was white, non-transparent and vaguely crystalline solid, which may likely be a remnant of a proto-crystal or perhaps unreacted dabco.

Because of the impurities and unideal adsorption results, the variables involved in the synthesis were adjusted, in order to inspect whether any major difference would occur. These differences include increased time in the oven and differing ratio of the reactants. Changing the ratio of $Ni_2(NO_3)_2 \cdot 6H_2O$, H_2abdc and dabco to 0.5 : 0.5: 0.5 (in mmol) was shown to give very bad results, as the product contained few actual crystals (roughly 10-15% pure), and was mostly covered by a whitish-brown, amorphous solid, which was present only as a tiny impurity in other samples. With PXRD, it was confirmed that the sample was mostly amorphous, with only few discernible peaks, while others were being blended in with the high background. The ratio was also changed to include more dabco than in original synthesis[48], approximately 0.5 : 0.5 : 1.5 (in mmol), which resulted in better results, especially for the samples that spent 48 h in the oven (Figure 6.1).
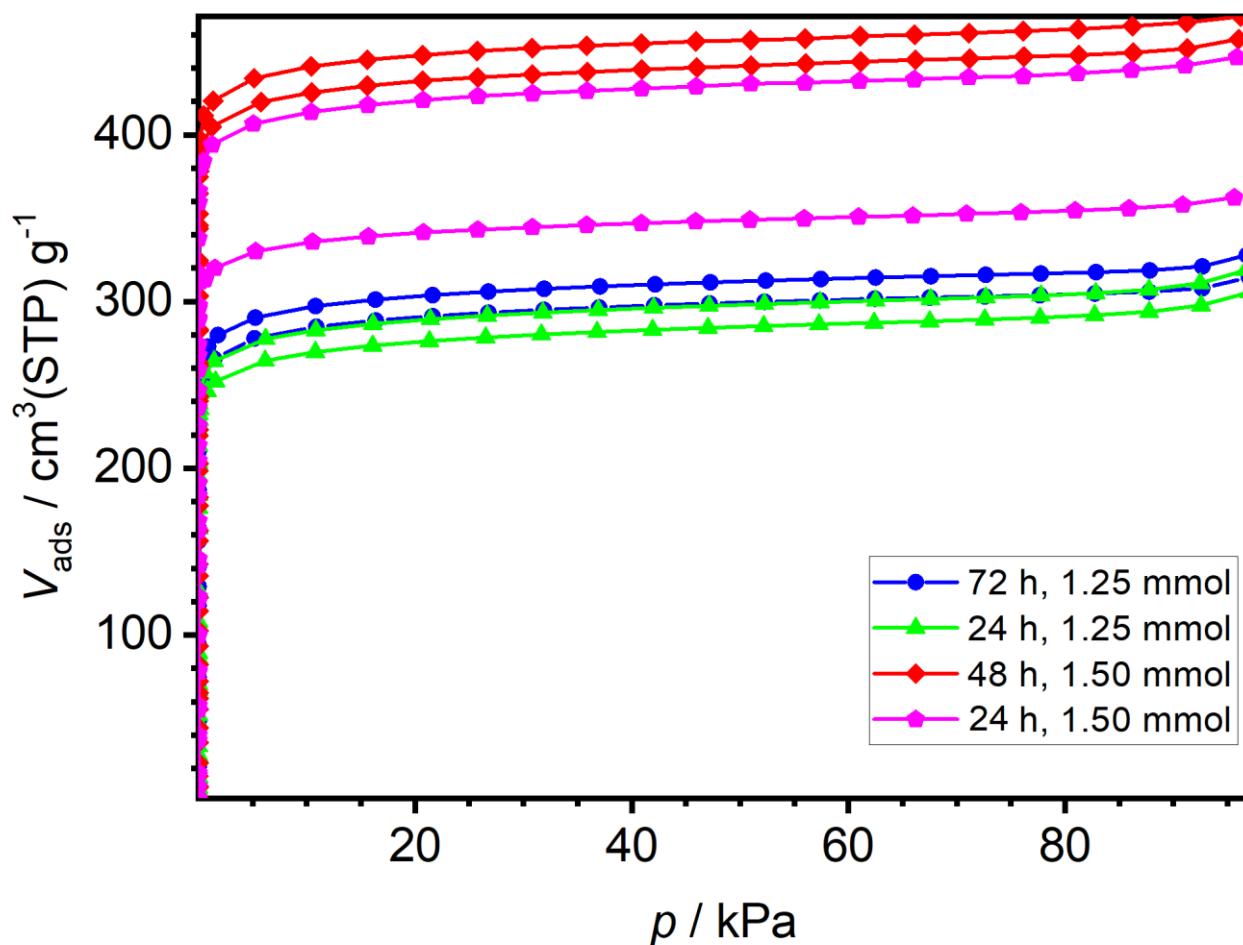
Figure 6.1 - *Comparison of $Ni_2(abdc)_2(dabco)$ isotherms of the samples synthesized as instructed by prior work[48], with tuned variables. Legend, from left to right: number of hours in oven, ratio of dabco with regards to 0.5 mmol for $Ni_2(NO_3)_2 \cdot 6H_2O$ and 0.5 mmol for H_2abdc*

It appears that when the amount of dabco is increased to 1.50 mmol as mentioned, but the oven time is reduced to just 24 h, the results are quite inconsistent. The pool of samples is only two each, so it may be too few to draw out any definitive conclusions. It should be safe to assume that under correct conditions and clean equipment, 24 h is enough with such ratio, considering the timing in other methods[41,42,48,68]. It is also highly probable that increasing the oven time to 72 h may result in as good (or better) isotherms than the ones which spent 48 h. However, this would obviously make the synthesis much less efficient, due to prolonged oven time. Judging by the plot alone, it can be postulated that increased oven time will result in better isotherms, which is also compatible with the logic of solvothermal synthesis; more time is given for the reactants to form more homogenous and well-defined crystals, which will naturally yield in better overall porosity.

The BET surface area, alongside pore volume were calculated from adsorption data of the samples presented in Figure 6.1, using the Roquerol criterion (Table 6.2).

Table 6.2 - Adsorption data of the Ni-samples shown in Figure 6.1.

Color of the isotherm	Time in oven / h	Ratio of Ni, H_2abdc, dabco / mmol	a_S (BET)/ m^2g^{-1} (mean)	V_{pore} (p/p_0 = 0.500) / cm^3g^{-1} (mean)
Green	24	0.5 : 0.5 : 1.25	1109.0	0.45
Blue	72	0.5 : 0.5 : 1.25	1174.8	0.47
Magenta	24	0.5 : 0.5 : 1.50	1544.7	0.60
Red	48	0.5 : 0.5 : 1.50	1775.7	0.70

The BET specific surface areas for Ni-ATP samples with increased dabco concentrations are comparable to those presented in most relevant previous works[39,48], where a_S^{BET} for Ni-analogue was reported to be 1536 and 1530 m^2g^{-1} respectively. Pore volumes were also similar, with V_{pore} = 0.61 and 0.50 cm^3g^{-1} respectively. However, the samples that retained original reactant ratios got worse a_S^{BET} by roughly 0.400 m^2g^{-1} and V_{pore} by 0.20 cm^3g^{-1}. $Ni_2(bdc)_2(dabco)$ samples were reported to have much higher specific BET surface areas and pore volumes, reaching 2120 m^2g^{-1} and 0.82 cm^3g^{-1} respectively[69]. For additional comparison, the scaled-up sample of $Ni_2(abdc)_2(dabco)$ possessed an a_S^{BET} of only 949.7 m^2g^{-1} and a V_{pore} = 0.39 cm^3g^{-1}, which is slightly more than half of what is expected of this analogue[39,40,48,70].

6.2 Analyzing the synchrotron scans

Previous work focused heavily on defining the space groups for the empty phase 3, which was all confirmed to be P4/mmm[39,42,48]. Due to that fact, it is expected that phases 1 and 2 need to fit nicely into tetragonal space groups as well, since they need to somewhat relate to P4/mmm, as well as be in higher hierarchy space groups[71]. This doesn't take into account the unit cells that have been extended, which will have different lattice parameter values, but still remain its relationship to the tetragonal crystal system. I4/mcm has been mentioned[[30,39-41,45,48,70,72-75] and observed to be the space group of solvated $M_2(bdc)_2(dabco)$, while also discovering that $M_2(abdc)_2(dabco)$ solvates in the same space group. However, it is observed on contour plots (Figures 5.6 - 5.9) that the structure goes through two phase changes, not just one, unlike the compounds without functionalized NH_2 group. Each of these three phases possess a unique diffraction pattern, allowing all three to be investigated more closely.

Out of all indexing solutions and throughout multiple tests, it was determined that P4/nbm (No. 125) fitted best to available data at Phase 2. Additionally, it also related well to P4/mmm (No. 123) and I4/mcm (No. 140) (Figure 6.2), as it lies right in between them in space group hierarchy. That is why the investigation is focusing exclusively on these three space groups. Monoclinic solutions have also been reported[76,77], however they either strayed away from standard synthesis procedure or applied high pressure to induce phase transition. However, interestingly the latter has shown that $Zn_2(bdc)_2(dabco)$ transitions to different phase depending on the guest molecule. The compound transitions to C2/m when EtOH is used, and P4/mmm when DMF is used[77]. DMF is the usual solvent used in the synthesis of the isoreticular $M_2(bdc)_2(dabco)$. These results may be relevant, even if the high pressure isn't involved, as they showcase a somewhat selectivity of the phases towards differing solvents.
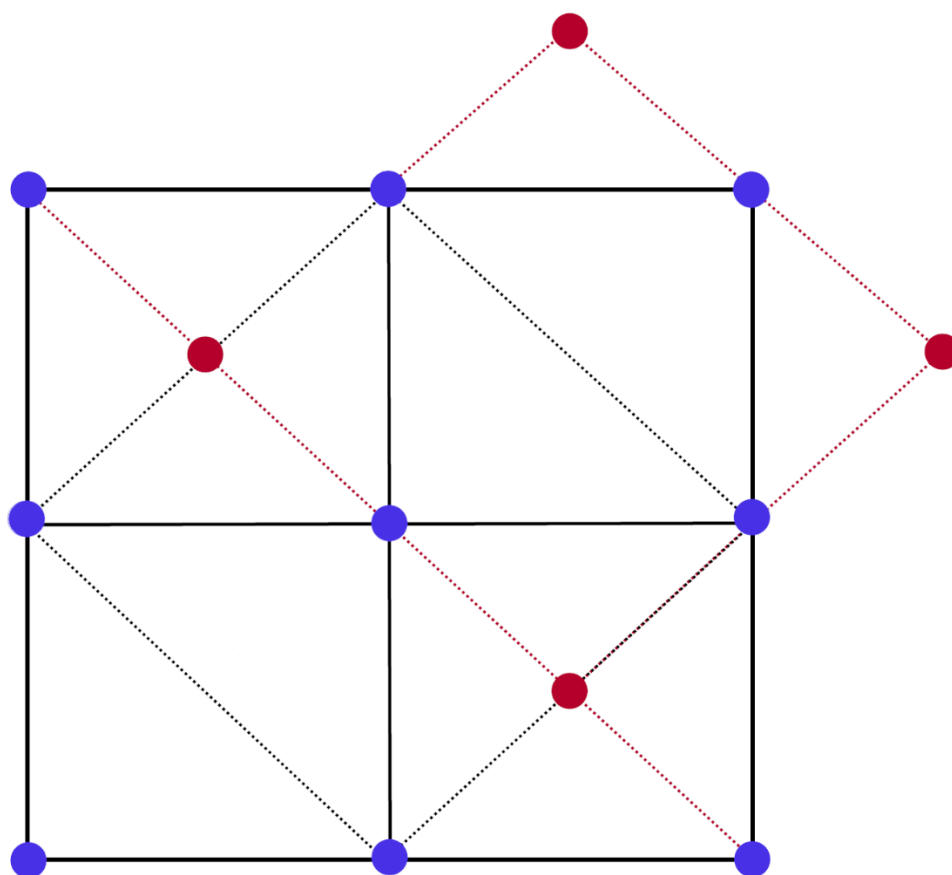
***Figure 6.2** - Illustration of the relationship between P4/mmm (hard black lines, blue dots), I4/mcm (black dotted lines, blue dots) and P4/nbm (red dotted lines, red dots). Dots represent possible positions of the paddle-wheel elements, while lines (dotted and hard) represent one length of a ligand (abdc in this case).*

All profile fits used 2nd order of Chebyshev background, as further increase in the integer resulted in extremely minor R_{wp} improvements. Spherical harmonics played an integral part in creating best possible fits that, despite being measured at synchrotron, still had unideal backgrounds alongside other anomalies, like sudden broadened peaks. This was especially prevalent for Co-analogue.

6.2.1 Determining space group for $M_2(abdc)_2(dabco)$, Phase 1

$M_2(abdc)_2(dabco)$ (M= Co, Cu, Zn) appears to crystallize in I4/mcm space group, in accordance with established papers[48,70-75] (Figure 6.3). However, it can be observed that the peaks shown do not correlate perfectly to the calculated pattern. It should be expected to some extent, as the calculated pattern is that of $M_2(bdc)_2(dabco)$[67] and doped with a certain amount of abdc, meaning that two linkers are used in differing ratios.

This would explain the peak at 2θ = 6.8°, which is unobserved in the other diffraction patterns. Nevertheless, it can serve as a decent guideline. All other major peaks appear to be corelating well to the calculated pattern, with most notable difference being that of Ni at 2θ = 6.8°, which is slightly shifted to the left, alongside the peak at 2θ = 10.9°, which was shifted to the right when compared with its analogues. Other disparities include the peaks of all four analogues at 2θ = 3.6°, which appear opposite in height when compared to the same two peaks for the calculated pattern. Additionally, Co displays an unusually broad peak at that point, alongside the peak at 2θ = 9.0°.
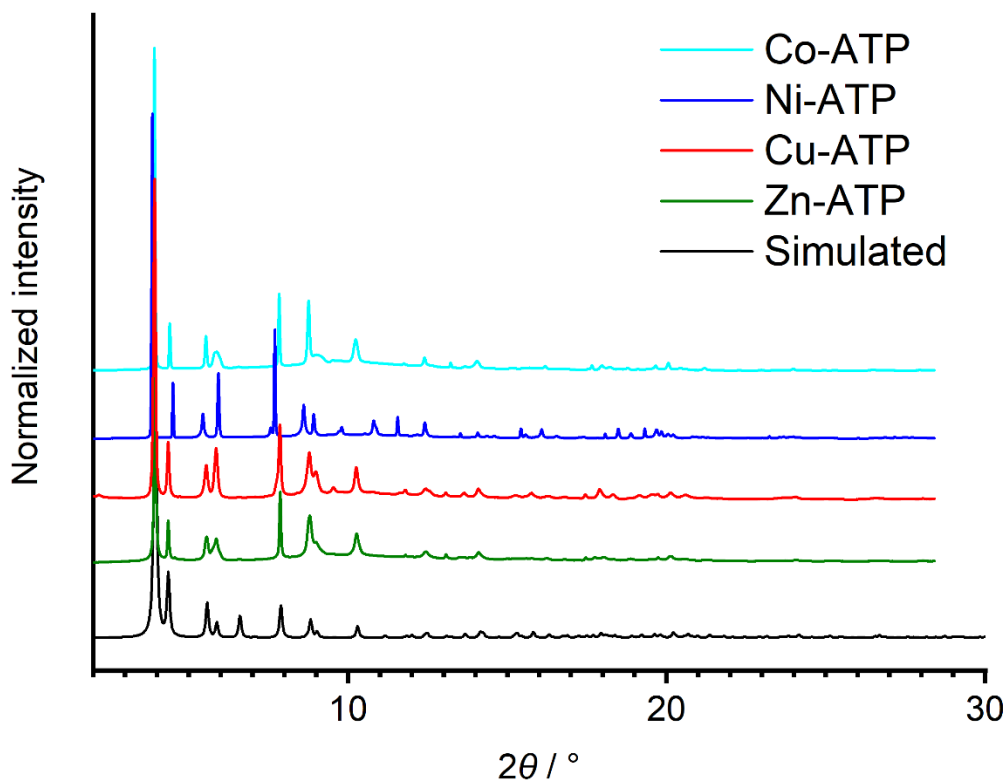
Figure 6.3 - *PXRD comparison of M$_2$(abdc)$_2$(dabco) analogues (M= Co, Ni, Cu, Zn) in Phase 1, alongside a calculated plot from Cadman et.al.[67].*

When determining the space group for M$_2$(abdc)$_2$(dabco) Phase 1, the indexing solutions were not suggesting the body-centered crystal system (I) as often as they likely should, but were usually leaning towards monoclinic solutions. These solutions were generally avoided, as they displayed irrational lattice parameter values, hence they were dropped from further testing.

For Co$_2$(abdc)$_2$(dabco), it is possible that Phase 1 may already have been under the process of desolvation. Both the first and other early scans were used, but both offered similar results, with slightly differing R_{wp} values for the specific space groups. The fits overall, weren't affected much by the change of scans. I4/mcm gave undesirable fits at 2θ = 5.8°, 9.0°, 10.2°, 12.4° and 14.0° (Figure A1.1). There were also three small unaccounted for peaks at 2θ = 6.5°, 11.7° and 13.2°. A big suspect is the possibility of a mixture of Phase 1 and Phase 2 already in the early scans. Another valid argument might be the cracking of the crystal, which could create peaks that would be badly fitted. Unlikely to be caused by impurities of other origin. R_{wp} = 5.1 %, which is much higher than for other analogues (Table 5.2). P4/mmm gave a bad fit at 2θ = 5.8°, 6.6°, 9.2°, 10.2° and 18.2° with an unaccounted peak at 2θ = 13.6° (Figure A1.2).

R_{wp} got to 3.06 %, which may further strengthen the argument that Phase 1 was impure, where some crystallites existed in Phase 3. Phase 2 cannot be an option, since its characteristic peak at 2θ = 2.2° is not observed at all. P4/nbm gave a good fit at first glance, but upon closer inspection, some of the peaks would not fill too well, especially ones at 2θ = 5.0°, 11.3°, 13.6°, 15.1° and 18.0° (Figure A1.3). The R_{wp} = 2.95 %, which is rather low, but contradicts previous results[48,41,70-75]. This unique scenario happened only once during this thesis, but the I4/mcm was chosen over P4/nbm, despite its lower R_{wp}.

For Ni$_2$(abdc)$_2$(dabco), I4/mcm solution is not a good fit. Peaks do not fit well at 2θ = 5.4°, 8.6°, 9.8°, 10.8° and 12.0°. There are also peaks that are completely omitted at 2θ = 7.7°, 13.3° and 14.3° (Figure A1.6) The overall R_{wp} was 9.8 %, which is rather high, and combined with the poor fit, the solution had to be discarded against the prediction stating otherwise. P4/mmm made for an even worse fit. Peaks at 2θ = 4.5°, 9.8°, 13.5° and 14.4° are completely omitted while peaks at 2θ = 5.4°, 5.9°, 8.6°, 8.9°, 10.8° and 12.4° are not fitting well or are shifted slightly (Figure A1.7). R_{wp} is as high as 20.3 %. Even more peaks are either omitted or badly fitted further down towards higher 2θ values, but the solution was wrong already after the first major omitted peak. P4/nbm is the best solution for Ni$_2$(abdc)$_2$(dabco) at Phase 1. Peaks at 2θ = 8.6°, 9.8°, 13.3° and 20.1° do not have an ideal fit, yet are not too far off from the observed positions (Figure A1.8). Overall R_{wp} is 3.8%, and is used as the space group for this phase. It is, however, fairly unpredicted as Phase 1 was thought to crystallize in I4/mcm space group across all four M$_2$(abdc)$_2$(dabco) analogues, as only the different metal tells them apart. It may be unlikely that it is any coincidental error, as the Ni$_2$(abdc)$_2$(dabco) sample synthesized in this thesis has also displayed greater affinity towards P4/nbm space group (Figure 5.5). An important detail is that the *c*-axis for this solution is half as long for Ni$_2$(abdc)$_2$(dabco) Phase 1 (Table 5.2). This attribute is unique to only this one analogue across all phases. Without further backup from high-quality, synchrotron level data, it is currently very difficult to assess for certain whether Ni$_2$(abdc)$_2$(dabco) crystallizes in I4/mcm or P4/nbm. However, judging by the results from this dataset alone, an assumption is made that the P4/nbm solution is the more correct one. Additionally, one can propose that it crystallizes specifically in the same manner as Ni$_2$(bdc)$_2$(dabco)[78] (Figure A2), as its lattice parameters are very similar.

Cu$_2$(abdc)$_2$(dabco) Phase 1 is likely to be contaminated with some crystallites engaging Phase 2 already in the first scans. This may be somehow connected to the higher temperature at which the measurement has started (Table 5.1), although 6 °C shouldn't make for such a big difference. However, from the samples synthesized in this thesis, it was determined that Cu$_2$(abdc)$_2$(dabco) (and likely the other analogues) are very sensitive towards concentration of the reactants. It is then possible, that perhaps a tiny portion of the sample crystallized in some other space group. This could explain the peak at 2θ = 2.2°, as it is characteristic to exclusively Phase 2. For this reason, P4/nbm was tested first, giving a decent fit for Phase 1, with R_{wp} of 3.3%.

However, there are some discrepancies at 2θ = 4.4°, 7.7°, 10.7°, 11.7° and 13.0° (Figure A1.14). Interestingly, the shoulder at 7.7° is made into a full peak in phase 2, further pushing the hypothesis that Phase 1 is already in the midst transitioning. Strangely, no other shoulders have been observed this early, as later on and right before Phase 2 starts, multiple shoulders are prevalent. Other scans were also tested, however to no different results. Curiously, when lattice parameters from P4/nbm are kept ($a = b$ = 15.1 Å and c = 19.2 Å) but the space group is replaced with P4/mmm, the peak at 2.2° is accounted for even more, yet does not fit perfectly into place (Figure A1.13). Otherwise, the rest of the peaks are covered similarly as with the P4/nbm solution. The shoulder at 7.7° is still unaccounted for. Despite these discrepancies, the R_{wp} is 2.9%, which should be the correct solution, judging purely by numbers. This solution is still very hesitantly used for Phase 1, since the phase is more than likely to be contaminated, in addition to being another contradiction to previous work[39-42, 48, 70-75]. I4/mcm presents a decent fit with the same shoulder observed at 2θ = 7.7°. There are also peaks that are not ideally fitted at 2θ = 11.6°, 13.1°, 14.8°, 15.5° and 17.4° (Figure A1.12). A small peak at 2θ = 10.7° is completely omitted by the calculated fit, which is not ideal, and the R_{wp} for the entire fit is 3.3%. The shoulder at 7.7° may actually be some form of impurity, whether structural or of foreign origin.

Zn$_2$(abdc)$_2$(dabco) had much more monoclinic and orthorhombic solutions than the previous analogues. It was unsurprising that the orthorhombic solution, Pnc2, gives the best fitting solution, even when there are some slightly unfitted peaks at 2θ = 5.8°, 10.2°, 11.8° and 17.5°. The shoulder at 5.8° which was also prevalent in other fits is better covered here, although not ideally (Figure A1.21). Despite the telling numbers, this solution cannot be correct as it has an insanely high value for one of the lattice parameters (c = 71 Å, compared to the usual case where $c \approx 19$). With such a large unit cell, it is fairly easy for a computational fit to adjust itself to the data, with very little actual logic. P4/mmm is not accounting for peak at 2θ = 4.5°, which is a major peak, and thus it is not a viable solution (Figure A1.19). P4/nbm gives a good fit with R_{wp} of 1.8 %, although it is important to mention that it is not provided in the indexing. The lattice parameters (Table 5.2) were taken from I4/mcm solution. However, there still are shoulders at 2θ = 5.7° and 9.0° that are not covered too well. At range 11.0° – 12.4° there are some peaks shown by the fit, that are unobserved on the scan (Figure A1.20). I4/mcm appears to be the best solution, given its decent fit, with R_{wp} of 2.0 %. There are few unaccounted for peaks at 2θ = 4.5° as well as the shoulder at 2θ = 5.8°. Range 2θ = 13.4° – 13.9° and 14.8° – 16.1° do not fit too well (Figure A1.18).

It wouldn't be outrageous to assume that $M_2(abdc)_2(dabco)$ (M = Co, Cu, Zn) crystallizes in I4/mcm space group, with the Ni-analogue being the only outlier. Such an anomalous behavior is likely due to lack of better data, rather than to this specific analogue being somewhat unique. It is likely that, due to their similarities, $M_2(abdc)_2(dabco)$ will share many structural qualities with $M_2(bdc)_2(dabco)$ as the functionalized NH_2 group will mostly affect the textural properties, rather than the structural. Most prominent of such quality being the slightly curved linker molecules, where one is bent down, while next one is bent upwards; then repeating the pattern throughout the entire lattice (Figure 6.4).
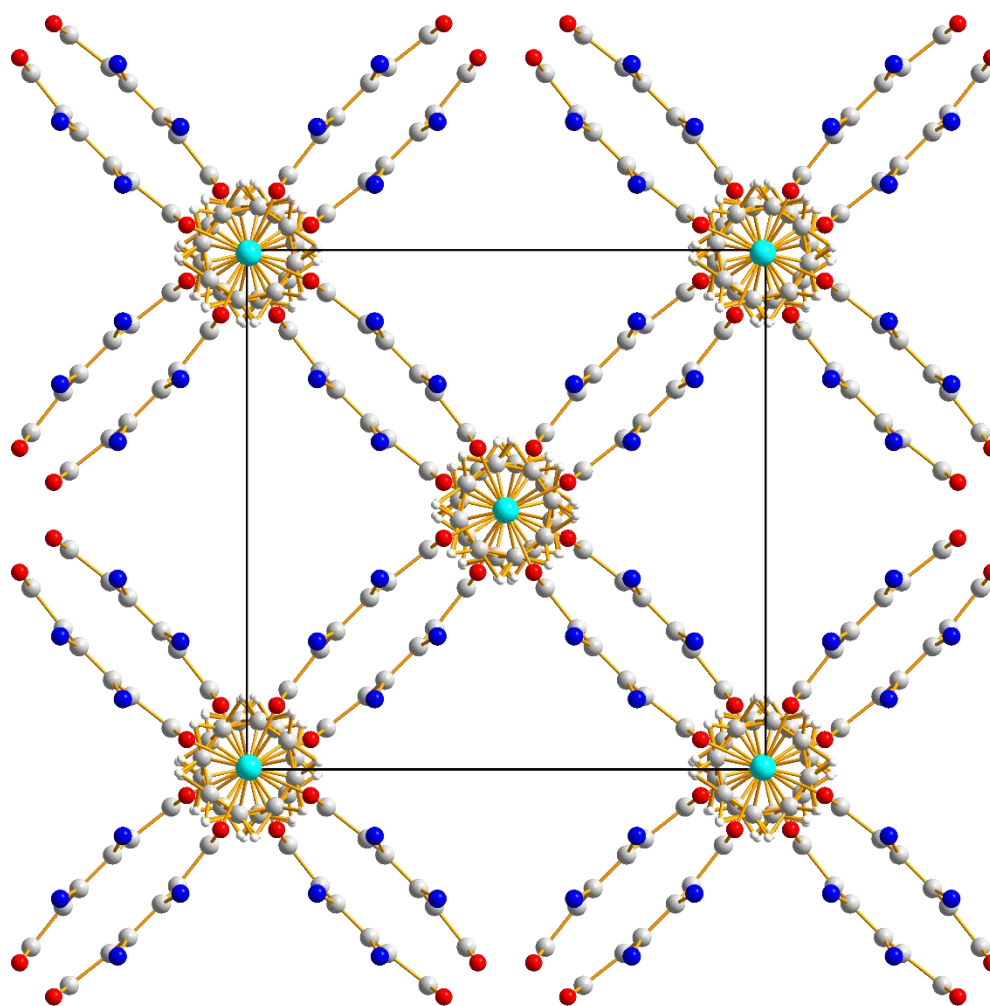
Figure 6.4 - *Extended unit cell of $Zn_2(bdc)_2(abdc)_x(dabco)$ in I4/mcm space group, rendered from the data provided by Cadman et.al[67]. Black lines indicate the unit cell's borders.*

Such a curved linker alignment is observed throughout most of the as-synthesized $M_2(bdc)_2(dabco)$ compounds[30,40,41,45,67,72,73,75], making it a high possibility that $M_2(abdc)_2(dabco)$ will crystallize in the exact same manner[39,48,76]. While running simulated annealing with the parameters of structure from Cadman et.al.[67], the result was one of the better ones, with an R_{wp} of roughly 10 %.

This is still too high to be of any scientific value, but it is just good enough to encourage further inspection in this direction. Lastly, it may serve as a temporary argument for the confirmation that these compounds indeed crystallize in I4/mcm space group.

6.2.2 Determining space group for $M_2(abdc)_2(dabco)$, Phase 2

Phases 1 and 3 are, although sparce with information, somewhat reported, which is why it is mostly accepted that $M_2(abdc)_2(dabco)$ (M = Co, Ni, Cu, Zn) crystallizes in I4/mcm, while transitioning into P4/mmm when close to, or completely empty. However, as observed from contour plots (Figures 5.6 – 5.9) there clearly is another transition, occurring right in between the aforementioned two phases. Unfortunately, Phase 2 is quite obscure, as it was not possible to find much information regarding this highly specific occurence. There has been a report of a solvated $Zn_2(bdc)_2(dabco)$ that crystallized in a P4/nbm space group[78]. The space group is retained, both when solvated and desolvated. Curiously, it also had a shortened c-axis (c = 9.5846 Å), which is comparable to the situation with $Ni_2(bdc)_2(dabco)$ in Phase 1. This could be used to somewhat compare the plots, even though the ligand is without the functionalized NH_2 molecule. It can be observed that the peaks shown correspond nicely to the simulated plot, aside from the obvious, missing peak at 2θ = 2.2°, which is a peak characteristic to this specific phase of $M_2(abdc)_2(dabco)$ (Figure 6.5). It is highly likely that this peak is connected to the length of the c-axis, as all four analogues possess a c – axis with length of around 19.2 in Phase 2 (Table 5.2). Only visible discrepancies appear in ranges 2θ = 15°-17° and 19°-20°. Additionally, the simulated peak at 2θ = 3.5° appears to be less intense than the one visible in other plots. For Ni-analogue, this peak seems to be shifted slightly to the right, compared to other patterns. Judging by the results from this thesis alone, as well as with the additional information provided[73,78], it can be assumed that when the crystals enter the brief Phase 2, they transition into a P4/nbm space group.
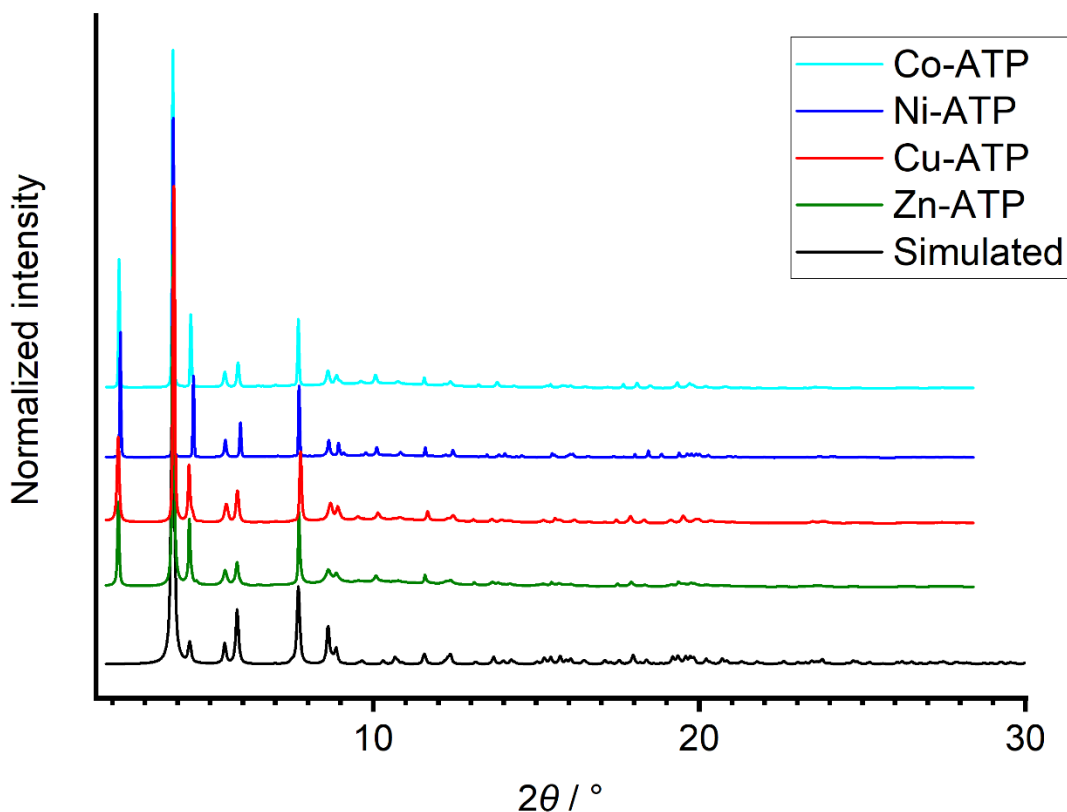
Figure 6.5 - *PXRD comparison of M$_2$(abdc)$_2$(dabco) analogues (M= Co, Ni, Cu, Zn) in Phase 2, with a simulated peak of Zn$_2$(bdc)$_2$(dabco) from Uemura et.al.[73]*

For Co$_2$(abdc)$_2$(dabco), I4/mcm would give a really good fit, but the very first peak at 2θ = 2.2° is completely unaccounted for. Thus, the solution cannot be used for further analysis. P4/mmm would not cover multiple peaks, including those at 2θ =10.0° and 11.0° (Figure A1.4). P4/nbm would give the best solution out of these three, with R_{wp} of just 1.9 %. The calculated plot fitted really well into all of the major peaks, only deviating slightly with barely noticeable peaks. This could be fixed by having a clearer background. Only at 2θ = 20.2° was there observed a deviation from the fit (Figure A1.5).

For Ni$_2$(abdc)$_2$(dabco), I4/mcm also misses the very first peak 2θ = 2.2°, which instantly makes it an unviable solution (Figure A1.9). P4/mmm gives a decent fit with slight discrepancies at 2θ = 7.1°, 10.2°, 11.6° and 14.1° and an R_{wp} of 3.7 %. This solution may explain the slight shift towards the right for peak at 2θ = 3.5°, which can be observed when samples are in Phase 3 (Figure A1.10). P4/nbm also gives a really good fit, with only peaks at 2θ = 7.1°, 8.6° and 9.8° that have some disparities (Figure A1.11). Strangely, the calculated fit gives a small shoulder at 10.2° where it is not observed on the original scan. The R_{wp} is 3.6 %, which is slightly lower than that for P4/mmm solution.

It appears that $Ni_2(abdc)_2(dabco)$ does not engage into a phase transition like its analogues, as the only transformation is that the *c*-axis is elongated from 9.3 Å to 18.7 Å (Table 5.2), alongside with the doubling of volume to *V* = 4399.7 Å³. This unusual transition can also be somewhat observed on the contour plot (Figure 5.7) as no visible shifts are seen throughout and the lines remain almost perfectly straight. There is only one additional line at $2\theta = 2.2°$ that appears and then disappears, marking the start and end of Phase 2 respectively. Thus, it is not unlikely that something makes $Ni_2(abdc)_2(dabco)$ unique, which causes it to crystallize in P4/nbm, and where its phase shift involves only the elongation of *c*-axis.

For $Cu_2(abdc)_2(dabco)$, I4/mcm omits the first peak at $2\theta = 2.2°$. It can be noted that it otherwise fits well with most other peaks, further intensifying how important that new first peak is for Phase 2 (Figure A1.15). P4/mmm yields a good fit, with a R_{wp} of 2.3%. Peaks do not fit ideally at 2θ = 4.3°, 7.9°, 10.1°, 10.8°, 13.3°, 14.4° and 17.4° (Figure A1.16). Especially the peak at 2θ = 10.8° is fitted badly, together with being shifted to the right. At 2θ = 7.0° there is a tiny peak that is not accounted for by the fit. A curious observation was made when P4/mmm was used with *c* = 9.63597 Å, as the first peak at 2θ = 2.2° would be omitted, but an otherwise well-fitted pattern would remain. This could possibly give an insight into Phase 2, and that it must involve a $c \approx 19$ Å, as even the previously mentioned $Ni_2(abdc)_2(dabco)$ elongated its *c*-axis. P4/nbm yields the possibly best fit with a R_{wp} = 1.9 %. Only the peaks at 2θ = 2.2°, 8.7°, 10.8°, 14.1° and 17.5° are not ideally fitted (Figure A1.17).

For $Zn_2(abdc)_2(dabco)$, I4/mcm, like with previous analogues, completely omits the peak at $2\theta = 2.2°$, but otherwise fits decently into the rest of the pattern. P4/mmm gives a decent fit, R_{wp} of 2.7 %. A tiny peak at 2θ = 6.1° is unaccounted for. Fit at 2θ = 7.7° is slightly shifted to the left, while fits at 2θ = 8.7°, 10.0°, 10.7°, 11.6° and 19.4° are shifted slightly to the right (Figure A1.21). Otherwise, fits at 2θ = 8.9° and 12.3° are in correct positions but do not fit ideally. P4/nbm results in an improved fit to P4/mmm, with R_{wp} of 2.5%. Peak at 2θ = 6.1° is still unaccounted for (Figure A1.22). Peaks that were mentioned as shifted in P4/mmm are now in correct positions, but do not fit ideally to the scan, however better than observed with other solutions.

Deciding whether P4/nbm is a good choice for Phase 2 is much more difficult, due to the lack of research done in this area. Out of many reports, only two included a $Zn_2(bdc)_2(dabco)$ with a P4/nbm space group[73, 78] (Figure A2). However, such an alignment wouldn't be possible here, as Phase 2 is shown to specifically involve elongated *c*-axis (Table 5.2). Both samples presented in the reports had a short *c*-axis, one that varied from *c* = 9.6084 Å to *c* = 9.5846 Å[73], while the other had a reported *c* = 9.5830 Å[78]. However, these might be valid solutions for $Ni_2(abdc)_2(dabco)$ in Phase 1, as it was shown to possess similar structural behavior.

When compared directly (Figure 6.6), it can be observed that almost all of the peaks fit well into each other, with the only discrepancy being the peak at 2θ = 4.5°, which is again, slightly shifted towards right for Ni. This may be correct, assuming that Ni-analogue doesn't crystallize in I4/mcm like other compounds. Arguments as to why are still lacking.
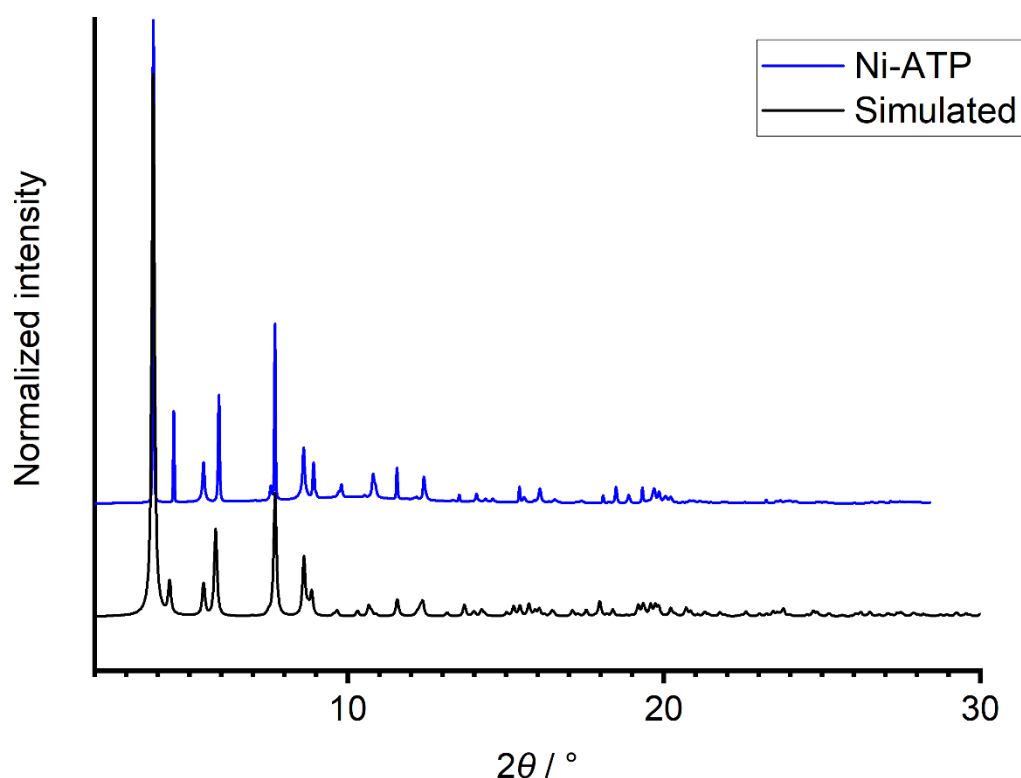

Figure 6.6 - *Comparison between Phase 1 Ni$_2$(abdc)$_2$(dabco) and the simulated plot of Zn$_2$(bdc)$_2$(dabco) obtained from Uemura et.al.[73]*

Judging purely by the results obtained in this thesis, it is most likely that Phase 2 of all M$_2$(abdc)$_2$(dabco) analogues (M = Co, Ni, Cu, Zn) involves a temporary shift from I4/mcm (No. 140) to P4/nbm (No. 125) before finally reaching the final phase, with the space group of P4/mmm (No. 123).

6.3 Sequential refinement

Sequential refinement was used mostly to investigate closer what happens with the lattice parameters as they transition into the three respective phases. It was performed with the assumptions discussed above, and with data presented in Table 5.1.

Co$_2$(abdc)$_2$(dabco) displays a gentle increase of all lattice parameters, where at the tail end of pure Phase 1, all parameters have increased. Parameter *a* have increased linearly from 15.14 Å to 15.17 Å, and *c* increased exponentially from 19.08 Å to 19.1 Å, where the shift was steep at first, but plateaued roughly in the middle of Phase 1. Volume also increased linearly, from 4360 Å^3 to 4400 Å^3 (Figure 5.6). These changes are tiny, but significant, as when reaching Phase 2, the increase in value appears much steeper. At the beginning of Phase 2 the *a* parameter have increased to 15.37 Å, *c* has decreased to 19.04 Å, while *V* increased to 4500 Å^3. The increase lasted until maxima was reached at *a* = *b* = 15.42 Å and *V* = 4560 Å^3. It appears that *c* reached its maxima roughly in the middle of Phase 1, as it only decreased once *c* = 19.1 Å. Finally, in Phase 3, all lattice parameters encounter a significant decrease, with *a* = 10.96 Å, *c* = 9.56 Å and *V* = 1160 Å^3. Parameters *a* and *V* all decreased slightly, with the latter essentially plateauing, while *a* shifted by 0.04 Å, after which decomposition would take place. Curiously, *c* would increase from 9.56 Å to 9.59 Å, which might relate to the desolvation of pores. The R_{wp} showcases that Phase 1 is actually more accurate when closer to Phase 2. This can further strengthen the mentioned hypothesis, that Co$_2$(abdc)$_2$(dabco) at Phase 1 is already under the process of desolvation. The most interesting part of the plot is the one for Phase 2 (Figure 6.7). There it displays a convex shape, meaning that the steep increase of *a* and *V* is most likely exaggerated. Similarly, the R_{wp} increases greatly at the tail end, meaning that the parameters are likely kept near-constant throughout Phase 3.
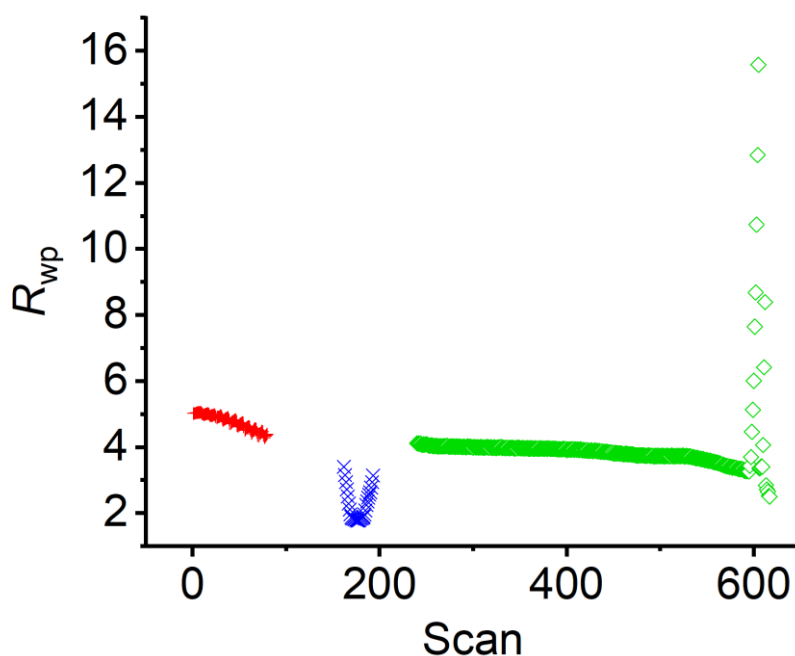
Figure 6.7 *- Plot displaying R$_{wp}$ values for Co$_2$(abdc)$_2$(dabco) at Phase 1 (red), Phase 2 (blue) and Phase 3 (green).*

Ni$_2$(abdc)$_2$(dabco) displays a much less dynamic shift in lattice parameters (Figure 5.7). Both *a* and *c* are kept almost constant throughout Phase 1, with only *c* increasing slightly from 9.32 Å to 9.34 Å, while *a* remained at 15.4 Å. Volume also is unchanged, being kept at 2300 Å^3. Phase 2 shows an interesting shift, as this time the parameters *a* and *b* decrease from 15.40 Å to 15.36 Å, unlike the shift observed with Co$_2$(abdc)$_2$(dabco). Parameter *c* doubles in length, as it increases all the way to 18.7 Å, a process which expands the unit cell. Volume also increases to 4500 Å, but remains unchanged. Once Phase 3 is reached, all parameters predictably decrease as follows: *a* = 10.90 Å, *c* = 9.35 Å and *V* = 1200 Å^3. The parameter *c* encounters a major increase at *T* = 210 °C, where it reaches a value of 9.41 Å. Simultaneously, from roughly the same temperature point, parameter *a* decreases, although not as steeply to *a* = 10.88 Å. It's unlikely that it is due to decomposition, as it occurs when *T* = 269.9 °C which is roughly 30 °C away from the end of the shown pattern. The R_{wp} is also consistent, and does not show any increase in its value (Figure 6.8).
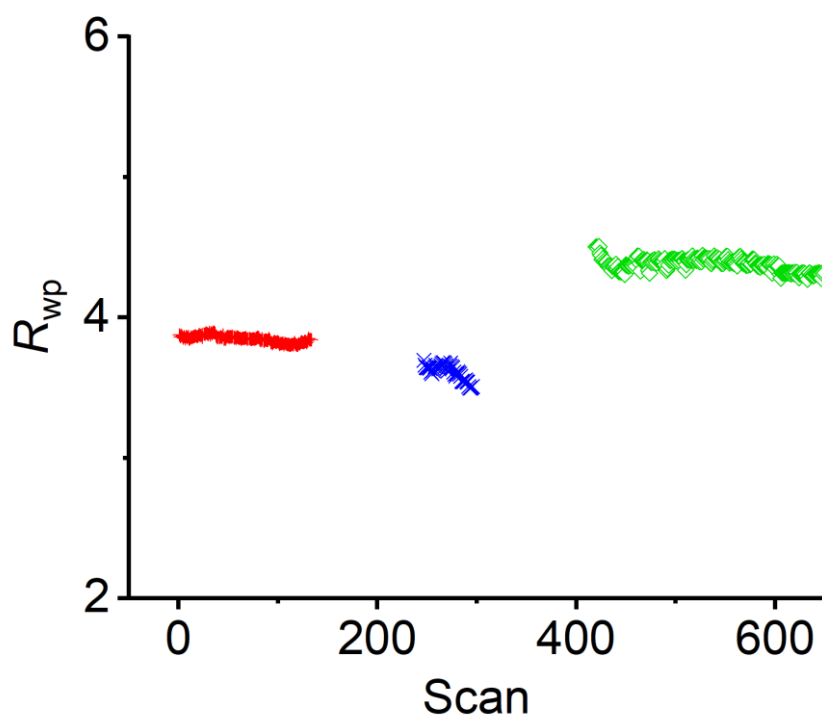
Figure 6.8 - *Plot displaying R$_{wp}$ values for Ni$_2$(abdc)$_2$(dabco) at Phase 1 (red), Phase 2 (blue) and Phase 3 (green).*

Cu$_2$(abdc)$_2$(dabco) displays an increase and decrease in a = 15.1 Å and c = 19.25 Å respectively for Phase 1, both with a change of just 0.02 Å (Figure 5.8). At Phase 2, c increases from 19.22 Å to 19.27 Å, while a increases from 15.12 Å to 15.28 Å, and V increases from 4400 Å^3 to 4500 Å^3. The parameters remain roughly constant, with only a varying with 0.02 Å throughout the entire phase. Phase 3 showcases the usual decrease, where a goes down to 10.82 Å, c decreases to 9.68 Å and V decreases to 1150 Å^3. The values remain constant until reaching T = 180 °C, after which a begins to rapidly decrease towards a = 10.78 Å, while c increases by 0.02 Å to 9.70 Å. Volume also decreases slightly, reaching 1120 Å^3. This change is sudden and occurs way before the supposed decomposition temperature. By observing R_{wp} plot, one can observe that Phase 3 behaved very strangely (Figure 6.9). At around scan 300 (which is roughly at T = 180 °C) the error rapidly increases to very high values. Such behavior can explain why the parameters changed so suddenly. Even more curious is the fact that R_{wp} drops back down to around 5 %. It therefore very likely that something wrong must've happened under the measuring procedure. This also likely means that the sudden change in parameters doesn't occur in reality, judging by the plots.
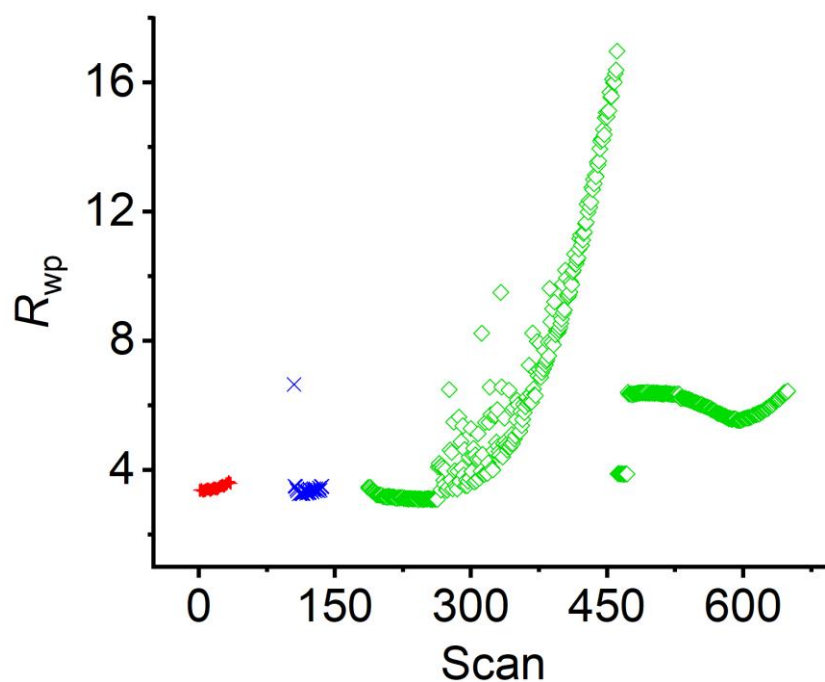
Figure 6.9 - *Plot displaying R_{wp} values for Cu$_2$(abdc)$_2$(dabco) at Phase 1 (red), Phase 2 (blue) and Phase 3 (green).*

Zn$_2$(abdc)$_2$(dabco) displays a familiar pattern for Phase 1, where a = 15.08 Å and gently increasing towards 15.12 Å, while c is pretty much constant at value of 19.26 Å (Figure 5.9). The volume is only slightly increasing, from 4380 to 4410 Å^3. At Phase 2, parameter a shoots up to 15.31 Å and increases further until reaching its maxima at 15.38 Å. Parameter c is shown to be decreasing already in Phase 2, as it is at 19.20 Å. Volume has gone up to 4500 Å^3 and continues increasing until 4550 Å^3. When Phase 3 is reached, all three parameters decrease to an already predicted value and stay constant. Parameter a drops to 10.91 Å, c to 9.62 Å and V to 1140 Å^3. Unfortunately, the data given was incomplete, thus it ends already at T = 150 °C, however it can be safely assumed that the material itself should retain its integrity until T = 250 °C [39,48,72]. The R_{wp} can to some degree support this idea, as it is observed that R_{wp} for Phase 3 is steadily going down (Figure 6.10). It can also be noted that initial R_{wp} at Phase 2 is around 3.8 %, but quickly drops down towards 2 %, which may imply that instead of shifting, the a and c parameters may instead just reach 15.35 Å and 19.2 Å respectively, and remain fairly constant until Phase 3.
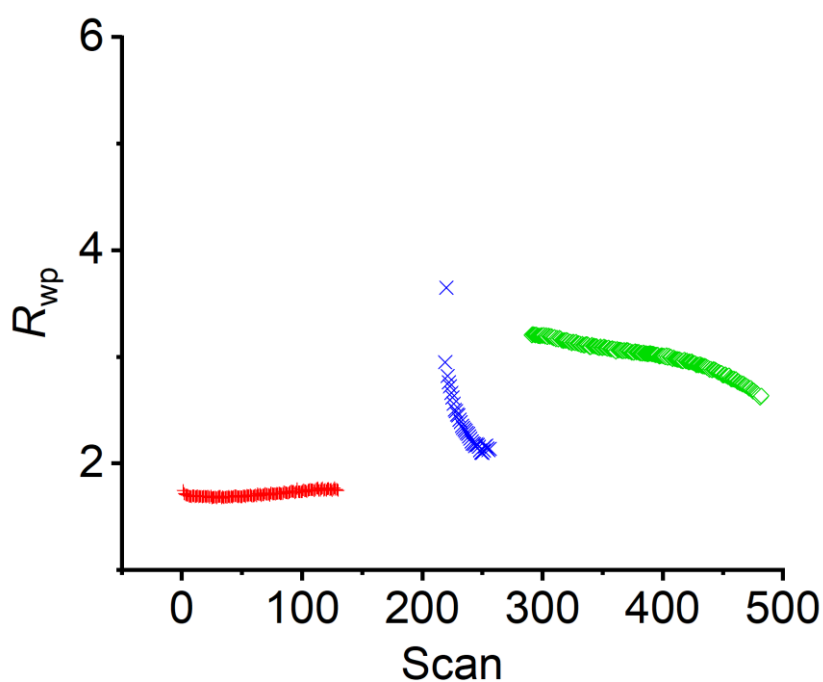
Figure 6.10 - *Plot displaying R$_{wp}$ values for Zn$_2$(abdc)$_2$(dabco) at Phase 1 (red), Phase 2 (blue) and Phase 3 (green).*

Throughout Phase 1, $M_2(abdc)_2(dabco)$ (M = Co, Ni, Cu, Zn) displayed a pattern, in which a and c would increase slightly. Parameters are also very similar, where $a \approx 15.1$ Å and $c \approx 19.18$ Å. This is to be expected, as aside from differing metals, the structures should be identical. The obvious deviation is $Ni_2(abdc)_2(dabco)$, which has a starting c of 9.3 Å, and parameter a is decreasing slightly. Again, this might be to simple error, perhaps during synthesis, or it might be that Ni-analogue is somehow special during its crystallization. Frankly, the observations made gently point towards the latter alternative.

During Phase 2, it was observed that all analogues assumed an increase in lattice parameter a, and similarly, the value of c would reach roughly 19.2-19.3 Å. Its increase or decrease during this phase might be to simple calculation errors (as observed by R_{wp} plots). Ni-analogue would double its unit cell alongside c-axis, which strengthens the assumption that Phase 2 requires parameter c with length of roughly 19 Å. It also seems that during this phase, the unit cell is at its largest, with lattice parameter values being at their highest (Table 5.2). At Phase 3, all parameters shrink down to $a \approx$ 10.8 Å and $c \approx 9.6$ Å, with the volume being roughly a quarter of the volume observed at Phase 1. All analogues appear to follow this pattern.

$M_2(abdc)_2(dabco)$ appear to be going through its transitions under following process. Upon crystallization, solvated pores give rise to I4/mcm space group. When heat is applied and temperatures reach roughly 60 °C, the first solvent molecules may start leaving the pores, and the compound transforms into a P4/nbm space group. It exists purely in this space group at around 80 °C. During this period, the unit cell expands slightly, which infers a limited flexibility of the pores: this quality is tied to the abdc/bdc ligand, and can be observed in other works[30,39,40,48,70,75]. Further heating will lead to quicker desolvation, which at around 90 °C triggers the transition into Phase 3. This causes the unit cell to shrink, as all lattice parameters go down in their values. At roughly 100 °C, most if not all crystallites assume their final form in P4/mmm space group. Further heating facilitates evaporation of most solvents, leaving pores completely empty. The structure remains thermally resistant until around 250-270 °C, after which it will start to decompose into metal oxides.

7.Conclusion

Pillar layered, $M_2(abdc)_2(dabco)$ (M = Co, Ni, Cu, Zn) with paddle-wheel elements are highly versatile materials possessing both good textural properties, alongside interesting structural qualities. The compound exists in a tetragonal crystal system, and remains unchanged. It has been determined that $M_2(abdc)_2(dabco)$ crystallizes in I4/mcm space group[39,48], similar to closely related $M_2(bdc)_2(dabco)$[70-75]. However, it has been observed that the material goes through phase transition at around 60 °C, at which it assumes the P4/nbm space group and is coupled with a slight growth in unit cell. This phase is only temporary, as at around 90 °C the crystallites transition to the predicted P4/mmm space group[48], and remain stable afterwards. Rapid shrinkage in unit cell is coupled together with this transition. $M_2(abdc)_2(dabco)$ remains stable in temperatures up to 270 °C, after which it starts the process of decomposing. $Ni_2(abdc)_2(dabco)$ is observed to crystallize in P4/nbm space group, but with a shortened *c*-axis. Further research is needed whether this is erroneous, or a uniquity to this analogue. The space groups are otherwise in good accordance with previous work[39-42,48,]. Synthesis of $Ni_2(abdc)_2(dabco)$ is most likely improved by implementing increased amount of dabco, which can improve adsorption of N_2 at low pressure for as much as 12 %[48]. The best sample had a_s^{BET} reach 1775.7 m^2g^{-1} and total pore volume of 0.70 cm^3g^{-1}, which is lower than for $Ni_2(bdc)_2(dabco)$[69]. Scaling-up the synthesis of $Ni_2(abdc)_2(dabco)$ will yield in a much less sorption potency, resulting in roughly 50% decrease when compared to previous work[39,48]. Scaled-up $Cu_2(abdc)_2(dabco)$ yielded in a_s^{BET} of 896.67 m^2g^{-1} and total pore volume of 0.36 cm^3g^{-1}, which was roughly 9 % less than anticipated[39,48]. It is likely that synthesizing $M_2(abdc)_2(dabco)$ under inert conditions might result in better results, however further research is needed. It has also been observed that $M_2(abdc)_2(dabco)$ is highly sensitive to the concentration of metal salts, which can drastically change its structure, PXRD plots and textural properties. Scaling up of the procedure[39,41,48] should be avoided, unless new procedure is designed from scratch.

References

[1]   BUI, M., ADJIMAN, C.S., and BARDOW, A., 2018. Carbon capture and storage (CCS): the way forward. *Energy & Environmental Science 11*, 5, 1062-1176. DOI= http://dx.doi.org/10.1039/C7EE02342A.

[2]   ROCHELLE, G.T., 2009. Amine scrubbing for CO2 capture. *Science 325*, 5948 (Sep 25), 1652-1654. DOI= http://dx.doi.org/10.1126/science.1176731.

[3]   YAGHI, O.M., LI, G., and LI, H., 1995. Selective binding and removal of guests in a microporous metal–organic framework. *Nature 378*, 6558 (1995/12/01), 703-706. DOI= http://dx.doi.org/10.1038/378703a0.

[4]   BATTEN, S.R., CHAMPNESS, N.R., CHEN, X.-M., GARCIA-MARTINEZ, J., KITAGAWA, S., ÖHRSTRÖM, L., O'KEEFFE, M., SUH, M.P., and REEDIJK, J., 2012. Coordination polymers, metal–organic frameworks and the need for terminology guidelines. *CrystEngComm 14*, 9, 3001-3004. DOI= http://dx.doi.org/10.1039/C2CE06488J.

[5]   DIETZEL, P.D.C., PANELLA, B., HIRSCHER, M., BLOM, R., and FJELLVÅG, H., 2006. Hydrogen adsorption in a nickel based coordination polymer with open metal sites in the cylindrical cavities of the desolvated framework. *Chemical Communications*, 9, 959-961. DOI= http://dx.doi.org/10.1039/B515434K.

[6]   TAGLIABUE, M., RIZZO, C., MILLINI, R., C, D., BLOM, R., and ZANARDI, S., 2011. Methane storage on CPO-27-Ni pellets. *Journal of Porous Materials 18*(06/01), 289. DOI= http://dx.doi.org/10.1007/s10934-010-9378-0.

[7]   GLOVER, T., PETERSON, G., SCHINDLER, B., BRITT, D., and YAGHI, O., 2010. MOF-74 building unit has a direct impact on toxic gas adsorption. *Chemical Engineering Science - CHEM ENG SCI 66*(12/11). DOI= http://dx.doi.org/10.1016/j.ces.2010.10.002.

[8]   BRITT, D., TRANCHEMONTAGNE, D., and YAGHI, O., 2008. Metal-organic frameworks with high capacity and selectivity for harmful gases. *Proceedings of the National Academy of Sciences of the United States of America 105*(09/01), 11623-11627. DOI= http://dx.doi.org/10.1073/pnas.0804900105.

[9]   DIETZEL, P., BLOM, R., and FJELLVÅG, H., 2008. Base-Induced Formation of Two Magnesium Metal-Organic Framework Compounds with a Bifunctional Tetratopic Ligand. *European Journal of Inorganic Chemistry 2008*(08/01), 3624-3632. DOI= http://dx.doi.org/10.1002/ejic.200701284.

[10]   DIETZEL, P.D.C., MORITA, Y., BLOM, R., and FJELLVÅG, H., 2005. An In Situ High-Temperature Single-Crystal Investigation of a Dehydrated Metal–Organic Framework Compound and Field-Induced Magnetization of One-Dimensional Metal–Oxygen Chains. *Angewandte Chemie 117*, 39 (2005/10/07), 6512-6516. DOI= http://dx.doi.org/https://doi.org/10.1002/ange.200501508.

[11]   ZHOU, W., WU, H., and YILDIRIM, T., 2008. Enhanced H2 Adsorption in Isostructural Metal–Organic Frameworks with Open Metal Sites: Strong Dependence of the Binding Strength on Metal Ions. *Journal of the American Chemical Society 130*, 46 (2008/11/19), 15268-15269. DOI= http://dx.doi.org/10.1021/ja807023q.

[12]   CAVKA, J.H., JAKOBSEN, S., OLSBYE, U., GUILLOU, N., LAMBERTI, C., BORDIGA, S., and LILLERUD, K.P., 2008. A New Zirconium Inorganic Building Brick Forming Metal Organic Frameworks with Exceptional Stability. *Journal of the American Chemical Society 130*, 42 (2008/10/22), 13850-13851. DOI= http://dx.doi.org/10.1021/ja8057953.

[13]   KANDIAH, M., NILSEN, M.H., USSEGLIO, S., JAKOBSEN, S., OLSBYE, U., TILSET, M., LARABI, C., QUADRELLI, E.A., BONINO, F., and LILLERUD, K.P., 2010. Synthesis and Stability of Tagged UiO-66 Zr-MOFs. *Chemistry of Materials 22*, 24 (2010/12/28), 6632-6640. DOI= http://dx.doi.org/10.1021/cm102601v.

[14]   MISHRA, P., EDUBILLI, S., MANDAL, B., and GUMMA, S., 2013. Adsorption of CO2, CO, CH4 and N2 on DABCO based metal organic frameworks. *Microporous and Mesoporous Materials*

169(2013/03/15/), 75-80. DOI= http://dx.doi.org/https://doi.org/10.1016/j.micromeso.2012.10.025.

[15]   WANG, H., GETZSCHMANN, J., SENKOVSKA, I., and KASKEL, S., 2008. Structural transformation and high pressure methane adsorption of Co 2(1,4-bdc) 2dabco. *Microporous and Mesoporous Materials - MICROPOROUS MESOPOROUS MAT 116*(12/01), 653-657. DOI= http://dx.doi.org/10.1016/j.micromeso.2008.05.037.

[16]   DECOSTE, J.B. and PETERSON, G.W., 2014. Metal–Organic Frameworks for Air Purification of Toxic Chemicals. *Chemical Reviews 114*, 11 (2014/06/11), 5695-5727. DOI= http://dx.doi.org/10.1021/cr4006473.

[17]   RITTER, S., 2005. Prussian blue still a hot topic. *Chemical & Engineering News 83*(05/02), 32-35. DOI= http://dx.doi.org/10.1021/cen-v083n018.p032.

[18]   KITAGAWA, S., 1992. Synthesis and Crystal Structures of Novel Copper(i) Co-ordination Polymers and a Hexacopper(1) Cluster of Quinoline-2-thione. *Inorganic Chemistry* 31, 1714-1717.

[19]   LI, H., EDDAOUDI, M., O'KEEFFE, M., and YAGHI, O.M., 1999. Design and synthesis of an exceptionally stable and highly porous metal-organic framework. *Nature 402*, 6759 (1999/11/01), 276-279. DOI= http://dx.doi.org/10.1038/46248.

[20]   BATTEN, S.R., CHAMPNESS, N.R., CHEN, X.-M., GARCIA-MARTINEZ, J., KITAGAWA, S., ÖHRSTRÖM, L., O'KEEFFE, M., PAIK SUH, M., and REEDIJK, J., 2013. Terminology of metal–organic frameworks and coordination polymers (IUPAC Recommendations 2013) *85*, 8, 1715-1724. DOI= http://dx.doi.org/doi:10.1351/PAC-REC-12-11-20.

[21]   MOGHADAM, P., LI, A., WIGGIN, S., TAO, A., MALONEY, A.G.P., WOOD, P., WARD, S.C., and FAIREN-JIMENEZ, D., 2017. Development of a Cambridge Structural Database Subset: A Collection of Metal-Organic Frameworks for Past, Present, and Future(04/11). DOI= http://dx.doi.org/10.17863/CAM.10091.

[22]   LOISEAU, T., SERRE, C., HUGUENARD, C., FINK, G., TAULELLE, F., HENRY, M., BATAILLE, T., and FÉREY, G., 2004. A rationale for the large breathing of the porous aluminum terephthalate (MIL-53) upon hydration. *Chemistry 10*, 6 (Mar 19), 1373-1382. DOI= http://dx.doi.org/10.1002/chem.200305413.

[23]   MILLANGE, F., SERRE, C., and FÉREY, G., 2002. Synthesis, structure determination and properties of MIL-53as and MIL-53ht: the first Criii hybrid inorganic–organic microporous solids: Criii(OH)·{O2C–C6H4–CO2}·{HO2C–C6H4–CO2H}x. *Chemical Communications*, 8, 822-823. DOI= http://dx.doi.org/10.1039/B201381A.

[24]   DIETZEL, P.D.C., BESIKIOTIS, V., and BLOM, R., 2009. Application of metal–organic frameworks with coordinatively unsaturated metal sites in storage and separation of methane and carbon dioxide. *Journal of Materials Chemistry 19*, 39, 7362-7370. DOI= http://dx.doi.org/10.1039/B911242A.

[25]   CHUI, S.S., LO, S.M., CHARMANT, J.P., ORPEN, A.G., and WILLIAMS, I.D., 1999. A chemically functionalizable nanoporous material. *Science 283*, 5405 (Feb 19), 1148-1150. DOI= http://dx.doi.org/10.1126/science.283.5405.1148.

[26]   O'KEEFFE, M., 2009. Design of MOFs and intellectual content in reticular chemistry: a personal view. *Chemical Society Reviews 38*, 5, 1215-1217. DOI= http://dx.doi.org/10.1039/B802802H.

[27]   YAGHI, O.M., O'KEEFFE, M., OCKWIG, N.W., CHAE, H.K., EDDAOUDI, M., and KIM, J., 2003. Reticular synthesis and the design of new materials. *Nature 423*, 6941 (2003/06/01), 705-714. DOI= http://dx.doi.org/10.1038/nature01650.

[28]   MOGHADAM, P.Z., LI, A., LIU, X.-W., BUENO-PEREZ, R., WANG, S.-D., WIGGIN, S.B., WOOD, P.A., and FAIREN-JIMENEZ, D., 2020. Targeted classification of metal–organic frameworks in the Cambridge structural database (CSD). *Chemical Science 11*, 32, 8373-8387. DOI= http://dx.doi.org/10.1039/D0SC01297A.

[29]   SAVONNET, M., BAZER-BACHI, D., BATS, N., PEREZ-PELLITERO, J., JEANNEAU, E., LECOCQ, V., PINEL, C., and FARRUSSENG, D., 2010. Generic Postfunctionalization Route from Amino-

Derived Metal–Organic Frameworks. *Journal of the American Chemical Society 132*, 13 (2010/04/07), 4518-4519. DOI= http://dx.doi.org/10.1021/ja909613e.

[30] WANG, H., GETZSCHMANN, J., SENKOVSKA, I., and KASKEL, S., 2008. Structural transformation and high pressure methane adsorption of Co2(1,4-bdc)2dabco. *Microporous and Mesoporous Materials 116*, 1 (2008/12/01/), 653-657. DOI= http://dx.doi.org/https://doi.org/10.1016/j.micromeso.2008.05.037.

[31] EDDAOUDI, M., KIM, J., ROSI, N., VODAK, D., WACHTER, J., O'KEEFFE, M., and YAGHI, O.M., 2002. Systematic design of pore size and functionality in isoreticular MOFs and their application in methane storage. *Science 295*, 5554 (Jan 18), 469-472. DOI= http://dx.doi.org/10.1126/science.1067208.

[32] MENDES, A.C., BARAN, E.T., REIS, R.L., and AZEVEDO, H.S., 2013. Self-assembly in nature: using the principles of nature to create complex nanobiomaterials. *WIREs Nanomedicine and Nanobiotechnology 5*, 6 (2013/11/01), 582-612. DOI= http://dx.doi.org/https://doi.org/10.1002/wnan.1238.

[33] RUBIO-MARTINEZ, M., AVCI-CAMUR, C., THORNTON, A.W., IMAZ, I., MASPOCH, D., and HILL, M.R., 2017. New synthetic routes towards MOF production at scale. *Chemical Society Reviews 46*, 11, 3453-3480. DOI= http://dx.doi.org/10.1039/C7CS00109F.

[34] STOCK, N. and BISWAS, S., 2012. Synthesis of Metal-Organic Frameworks (MOFs): Routes to Various MOF Topologies, Morphologies, and Composites. *Chemical Reviews 112*, 2 (2012/02/08), 933-969. DOI= http://dx.doi.org/10.1021/cr200304e.

[35] KLINOWSKI, J., ALMEIDA PAZ, F.A., SILVA, P., and ROCHA, J., 2011. Microwave-Assisted Synthesis of Metal–Organic Frameworks. *Dalton Transactions 40*, 2, 321-330. DOI= http://dx.doi.org/10.1039/C0DT00708K.

[36] LEE, J.H., AHN, Y., and KWAK, S.-Y., 2022. Facile Sonochemical Synthesis of Flexible Fe-Based Metal–Organic Frameworks and Their Efficient Removal of Organic Contaminants from Aqueous Solutions. *ACS Omega 7*, 27 (2022/07/12), 23213-23222. DOI= http://dx.doi.org/10.1021/acsomega.2c01068.

[37] PICHON, A., LAZUEN-GARAY, A., and JAMES, S.L., 2006. Solvent-free synthesis of a microporous metal–organic framework. *CrystEngComm 8*, 3, 211-214. DOI= http://dx.doi.org/10.1039/B513750K.

[38] MÄRCZ, M., JOHNSEN, R.E., DIETZEL, P.D.C., and FJELLVÅG, H., 2012. The iron member of the CPO-27 coordination polymer series: Synthesis, characterization, and intriguing redox properties. *Microporous and Mesoporous Materials 157*(2012/07/15/), 62-74. DOI= http://dx.doi.org/https://doi.org/10.1016/j.micromeso.2011.12.035.

[39] ARSTAD, B., FJELLVÅG, H., KONGSHAUG, K.O., SWANG, O., and BLOM, R., 2008. Amine functionalised metal organic frameworks (MOFs) as adsorbents for carbon dioxide. *Adsorption 14*, 6 (2008/12/01), 755-762. DOI= http://dx.doi.org/10.1007/s10450-008-9137-6.

[40] GÓMEZ-AGUIRRE, L.C., CASTRO-GARCÍA, S., SÁNCHEZ-ANDÚJAR, M., YÁÑEZ-VILAR, S., MIRA, J., BERMÚDEZ-GARCÍA, J.M., CENTENO, T.A., and SEÑARÍS-RODRÍGUEZ, M.A., 2016. A Facile Synthesis of Co3O4 Hollow Microtubes by Decomposition of a Cobalt Metal–Organic Framework. *European Journal of Inorganic Chemistry 2016*, 27, 4463-4469. DOI= http://dx.doi.org/10.1002/ejic.201600192.

[41] DYBTSEV, D.N., CHUN, H., and KIM, K., 2004. Rigid and Flexible: A Highly Porous Metal–Organic Framework with Unusual Guest-Dependent Dynamic Behavior. *Angewandte Chemie International Edition 43*, 38 (2004/09/27), 5033-5036. DOI= http://dx.doi.org/https://doi.org/10.1002/anie.200460712.

[42] HIRAI, K., FURUKAWA, S., KONDO, M., MEILIKHOV, M., SAKATA, Y., SAKATA, O., and KITAGAWA, S., 2012. Targeted functionalisation of a hierarchically-structured porous coordination polymer crystal enhances its entire function. *Chemical Communications 48*, 52, 6472-6474. DOI= http://dx.doi.org/10.1039/C2CC31421E.

[43] KONGPATPANICH, K., HORIKE, S., SUGIMOTO, M., KITAO, S., SETO, M., and KITAGAWA, S., 2014. A porous coordination polymer with a reactive diiron paddlewheel unit. *Chemical Communications 50*, 18, 2292-2294. DOI= http://dx.doi.org/10.1039/C3CC47954D.

[44] LEE, J.Y., OLSON, D.H., PAN, L., EMGE, T.J., and LI, J., 2007. Microporous Metal–Organic Frameworks with High Gas Sorption and Separation Capacity. *Advanced Functional Materials 17*, 8 (2007/05/21), 1255-1262. DOI= http://dx.doi.org/https://doi.org/10.1002/adfm.200600944.

[45] MANIAM, P. and STOCK, N., 2011. Investigation of Porous Ni-Based Metal–Organic Frameworks Containing Paddle-Wheel Type Inorganic Building Units via High-Throughput Methods. *Inorganic Chemistry 50*, 11 (2011/06/06), 5085-5097. DOI= http://dx.doi.org/10.1021/ic200381f.

[46] ZAREKARIZI, F., JOHARIAN, M., and MORSALI, A., 2018. Pillar-layered MOFs: functionality, interpenetration, flexibility and applications. *Journal of Materials Chemistry A 6*, 40, 19288-19329. DOI= http://dx.doi.org/10.1039/C8TA03306D.

[47] TANABE, K.K. and COHEN, S.M., 2011. Postsynthetic modification of metal–organic frameworks—a progress report. *Chemical Society Reviews 40*, 2, 498-519. DOI= http://dx.doi.org/10.1039/C0CS00031K.

[48] SKURTVEIT, A., 2021. Amino-Functionalised Pillared-Layered Metal-Organic Frameworks: Characterisation and Selective Adsorption Properties. In *Department of Chemistry* University of Bergen.

[49] REES, O.J., 2011. *Fourier transform infrared spectroscopy: Developments, techniques and applications*.

[50] THOMMES, M., KANEKO, K., NEIMARK, A.V., OLIVIER, J.P., RODRIGUEZ-REINOSO, F., ROUQUEROL, J., and SING, K.S.W., 2015. Physisorption of gases, with special reference to the evaluation of surface area and pore size distribution (IUPAC Technical Report) *87*, 9-10, 1051-1069. DOI= http://dx.doi.org/doi:10.1515/pac-2014-1117.

[51] NUHNEN, A. and JANIAK, C., 2020. A practical guide to calculate the isosteric heat/enthalpy of adsorption via adsorption isotherms in metal–organic frameworks, MOFs. *Dalton Transactions 49*, 30, 10295-10307. DOI= http://dx.doi.org/10.1039/D0DT01784A.

[52] LANGMUIR, I., 1918. THE ADSORPTION OF GASES ON PLANE SURFACES OF GLASS, MICA AND PLATINUM. *Journal of the American Chemical Society 40*, 9 (1918/09/01), 1361-1403. DOI= http://dx.doi.org/10.1021/ja02242a004.

[53] BRUNAUER, S., EMMETT, P.H., and TELLER, E., 1938. Adsorption of Gases in Multimolecular Layers. *Journal of the American Chemical Society 60*, 2 (1938/02/01), 309-319. DOI= http://dx.doi.org/10.1021/ja01269a023.

[54] ROUQUEROL, J., LLEWELLYN, P., and ROUQUEROL, F., 2007. Is the BET Equation Applicable to Microporous Adsorbents? *Studies in Surface Science and Catalysis 160*(12/31), 49-56. DOI= http://dx.doi.org/10.1016/S0167-2991(07)80008-5.

[55] VELLA-ZARB, L., 2020. Physical Methods for Characterizing Solids, 65-130. DOI= http://dx.doi.org/10.1201/9780429027284-2.

[56] WAESELMANN, N., 2012. Structural transformations in complex perovskite-type relaxor and relaxor-based ferroelectrics at high pressures and temperatures.

[57] BRUCE, D.W., O'HARE, D., and WALTON, R.I., 2014. Structure from Diffraction Methods John Wiley & Sons, Incorporated, New York, UNITED KINGDOM.

[58] BALERNA, A. and MOBILIO, S., 2015. Introduction to Synchrotron Radiation. *Synchrotron Radiation: Basics, Methods and Applications*(01/01), 3-28. DOI= http://dx.doi.org/10.1007/978-3-642-55315-8_1.

[59] PAWLEY, G., 1981. Unit-cell refinement from powder diffraction scans. *Journal of Applied Crystallography 14*, 357-361.

[60] COELHO, A., 2018. TOPAS and TOPAS-Academic: an optimization program integrating computer algebra and crystallographic objects written in C++. *Journal of Applied Crystallography 51*, 1, 210-218. DOI= http://dx.doi.org/doi:10.1107/S1600576718000183.

[61]   JÄRVINEN, M., 1992. Application of symmetrized harmonics expansion to correction of the preferred orientation effect, Journal of Applied Crystallography, 525-531.

[62]   COELHO, A., 2000. Whole-profile structure solution from powder diffraction data using simulated annealing. *Journal of Applied Crystallography 33*, 3 Part 2, 899-908. DOI= http://dx.doi.org/doi:10.1107/S002188980000248X.

[63]   RIETVELD, H.M., 1969. A Profile Refinement Method for Nuclear and Magnetic Structures *J. Appl. Cryst. 2*, 65-71.

[64]   FLACK, H.D., 2003. Chiral and Achiral Crystal Structures. *Helvetica Chimica Acta 86*, 4 (2003/04/01), 905-921. DOI= http://dx.doi.org/https://doi.org/10.1002/hlca.200390109.

[65]   LI, J., 2010. *Phase transitions in crystalline materials.* University of Illinois.

[66]   BIRTA, L.G. and DEO, U., 1986. A sequential refinement approach for parameter optimization in continuous dynamic models. *Mathematics and Computers in Simulation 28*, 1 (1986/02/01/), 25-39. DOI= http://dx.doi.org/https://doi.org/10.1016/0378-4754(86)90085-6.

[67]   CADMAN, L.K., BRISTOW, J.K., STUBBS, N.E., TIANA, D., MAHON, M.F., WALSH, A., and BURROWS, A.D., 2016. Compositional control of pore geometry in multivariate metal–organic frameworks: an experimental and computational study. *Dalton Transactions 45*, 10, 4316-4326. DOI= http://dx.doi.org/10.1039/C5DT04045K.

[68]   NGUYEN, T.T. and PHAN, N.T.S., 2014. A Metal–Organic Framework Cu2(BDC)2(DABCO) as an Efficient and Reusable Catalyst for Ullmann-Type N-Arylation of Imidazoles. *Catalysis Letters 144*, 11 (2014/11/01), 1877-1883. DOI= http://dx.doi.org/10.1007/s10562-014-1355-9.

[69]   A, S., ZHOU, K., A, N., YAO, C., KE, X., VAN TENDELOO, G., and VERPOORT, F., 2014. Tuning metal sites of DABCO MOF for gas purification at ambient conditions. *Microporous and Mesoporous Materials 201*(10/03), 277-285. DOI= http://dx.doi.org/10.1016/j.micromeso.2014.09.038.

[70]   SÁNCHEZ-ANDÚJAR, M., YÁÑEZ-VILAR, S., PATO-DOLDÁN, B., GÓMEZ-AGUIRRE, C., CASTRO-GARCÍA, S., and SEÑARÍS-RODRÍGUEZ, M.A., 2012. Apparent Colossal Dielectric Constants in Nanoporous Metal Organic Frameworks. *The Journal of Physical Chemistry C 116*, 24 (2012/06/21), 13026-13032. DOI= http://dx.doi.org/10.1021/jp3026978.

[71]   CATTI, M., SOMMARIVA, M., and IBBERSON, R.M., 2007. Tetragonal superstructure and thermal history of Li0.3La0.567TiO3 (LLTO) solid electrolyte by neutron diffraction. *Journal of Materials Chemistry 17*, 13, 1300-1307. DOI= http://dx.doi.org/10.1039/B614345H.

[72]   ANDRZEJEWSKI, M., CASATI, N., and KATRUSIAK, A., 2017. Reversible pressure pre-amorphization of a piezochromic metal–organic framework. *Dalton Transactions 46*, 43, 14795-14803. DOI= http://dx.doi.org/10.1039/C7DT02511D.

[73]   KIM, Y., HALDAR, R., KIM, H., KOO, J., and KIM, K., 2016. The guest-dependent thermal response of the flexible MOF Zn2(BDC)2(DABCO). *Dalton Transactions 45*, 10, 4187-4192. DOI= http://dx.doi.org/10.1039/C5DT03710G.

[74]   LEE, H.-C., HWANG, J., SCHILDE, U., ANTONIETTI, M., MATYJASZEWSKI, K., and SCHMIDT, B.V.K.J., 2018. Toward Ultimate Control of Radical Polymerization: Functionalized Metal–Organic Frameworks as a Robust Environment for Metal-Catalyzed Polymerizations. *Chemistry of Materials 30*, 9 (2018/05/08), 2983-2994. DOI= http://dx.doi.org/10.1021/acs.chemmater.8b00546.

[75]   ZHU, L.-G. and XIAO, H.-P., 2008. Gas Storages in Microporous Metal-Organic Framework at Ambient Temperature. *Zeitschrift für anorganische und allgemeine Chemie 634*, 5 (2008/05/01), 845-847. DOI= http://dx.doi.org/https://doi.org/10.1002/zaac.200700580.

[76]   GEE, W.J., CADMAN, L.K., AMER HAMZAH, H., MAHON, M.F., RAITHBY, P.R., and BURROWS, A.D., 2016. Furnishing Amine-Functionalized Metal–Organic Frameworks with the β-Amidoketone Group by Postsynthetic Modification. *Inorganic Chemistry 55*, 21 (2016/11/07), 10839-10842. DOI= http://dx.doi.org/10.1021/acs.inorgchem.6b01917.

[77]   TURNER, G.F., MCKELLAR, S.C., ALLAN, D.R., CHEETHAM, A.K., HENKE, S., and MOGGACH, S.A., 2021. Guest-mediated phase transitions in a flexible pillared-layered metal–organic

framework under high-pressure. *Chemical Science 12*, 41, 13793-13801. DOI= http://dx.doi.org/10.1039/D1SC03108B.

[78]   UEMURA, K., YAMASAKI, Y., KOMAGAWA, Y., TANAKA, K., and KITA, H., 2007. Two-Step Adsorption/Desorption on a Jungle-Gym-Type Porous Coordination Polymer. *Angewandte Chemie International Edition 46*, 35 (2007/09/03), 6662-6665. DOI= http://dx.doi.org/https://doi.org/10.1002/anie.200702390.

Appendices
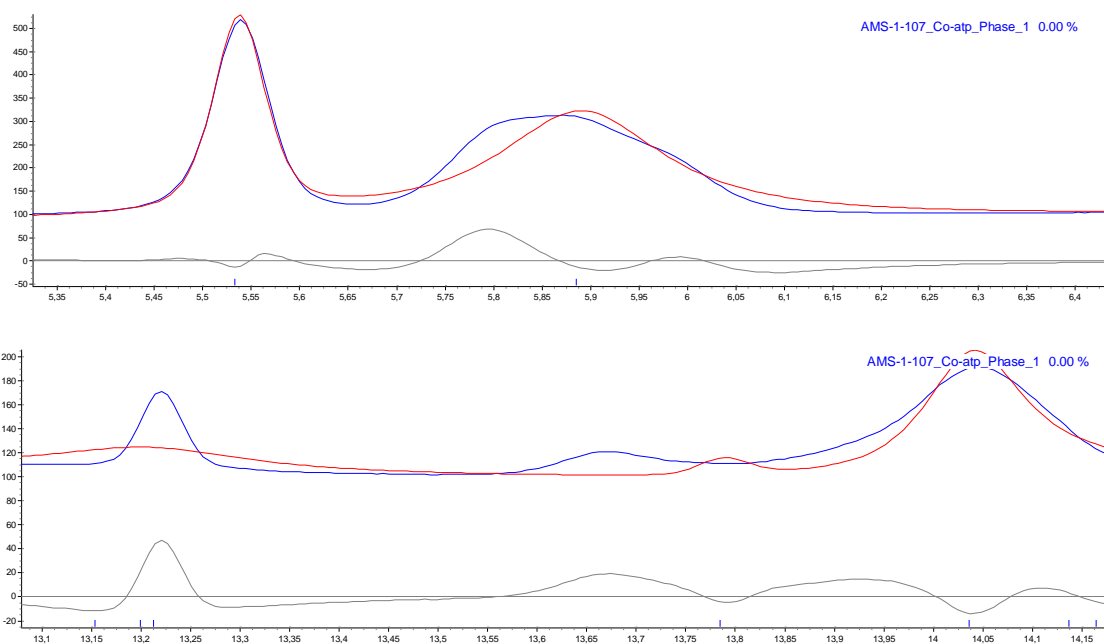
Figure A1.1 - *A PXRD plot, showcasing badly fitted peaks for Co-ATP, I4/mcm, Phase 1.*
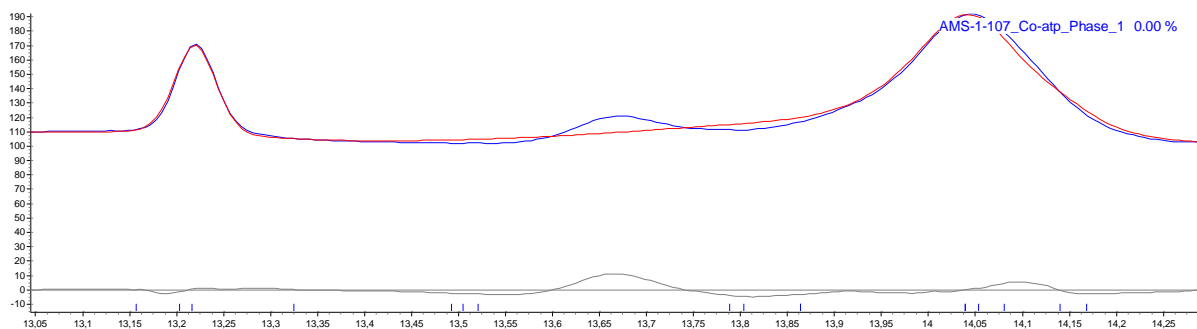
Figure A1.2 - *A PXRD plot, showcasing badly fitted peak for Co-ATP, P4/mmm, Phase 1.*
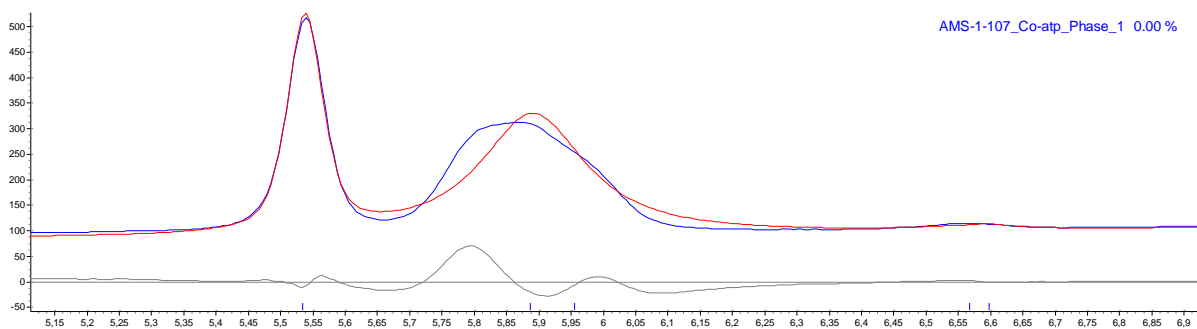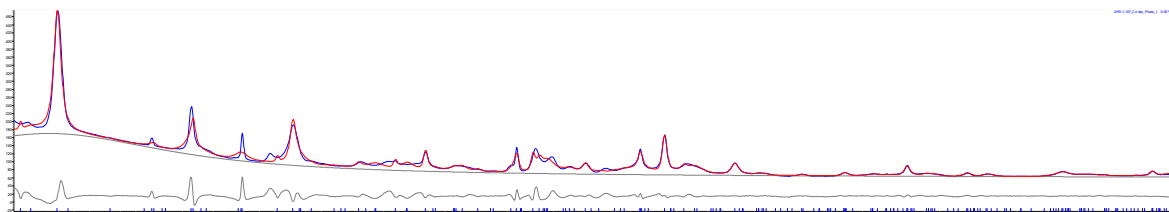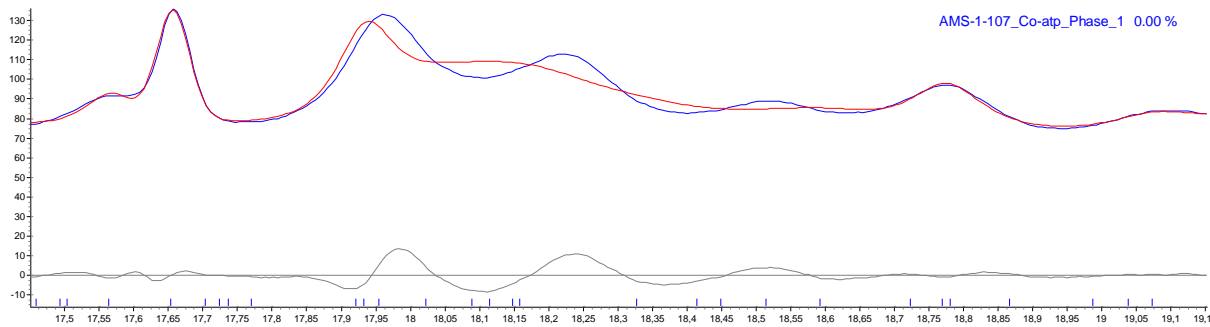
Figure A1.3 - *A PXRD plot, showcasing badly fitted peaks (upper) for Co-ATP, P4/nbm, Phase 1, as well as the overall fit (lower).*
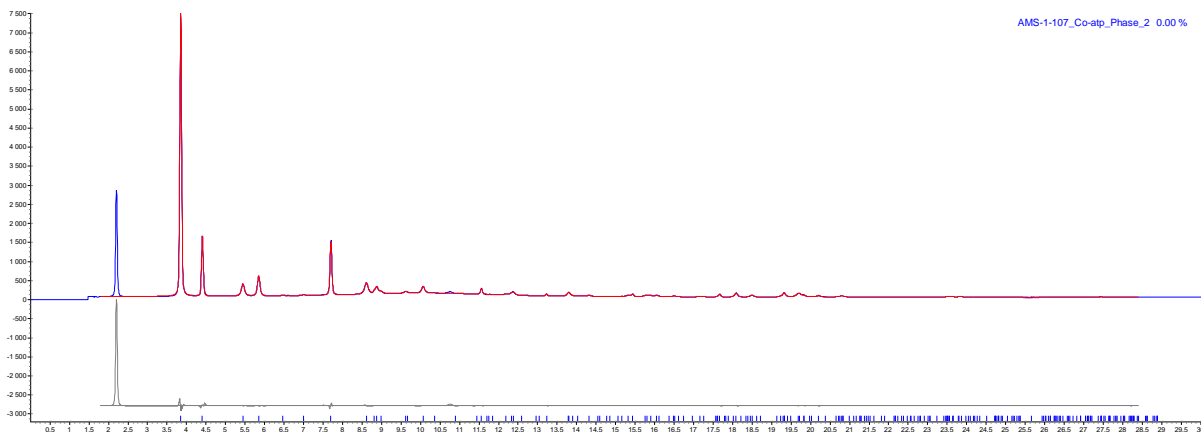
A PXRD fit, showcasing unaccounted for peak at $2\theta = 2°$ Co-ATP, I4/mcm, Phase 2.
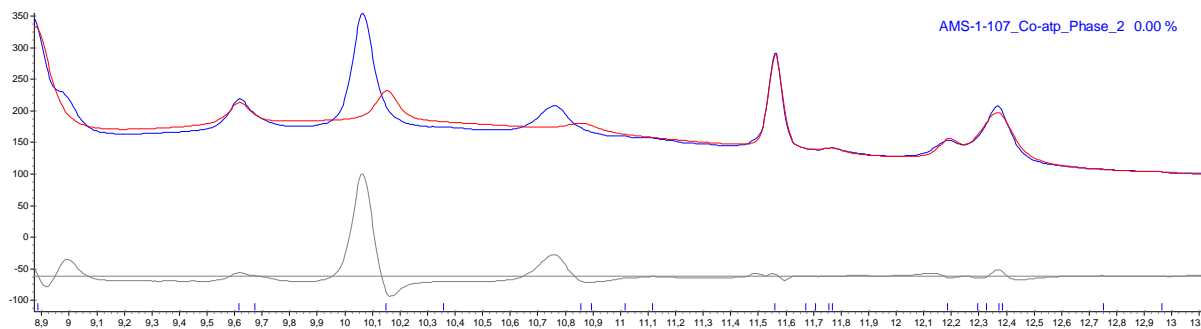
Figure A1.4 - *A PXRD fit, showcasing unaccounted for peaks Co-ATP, P4/mmm, Phase 2.*
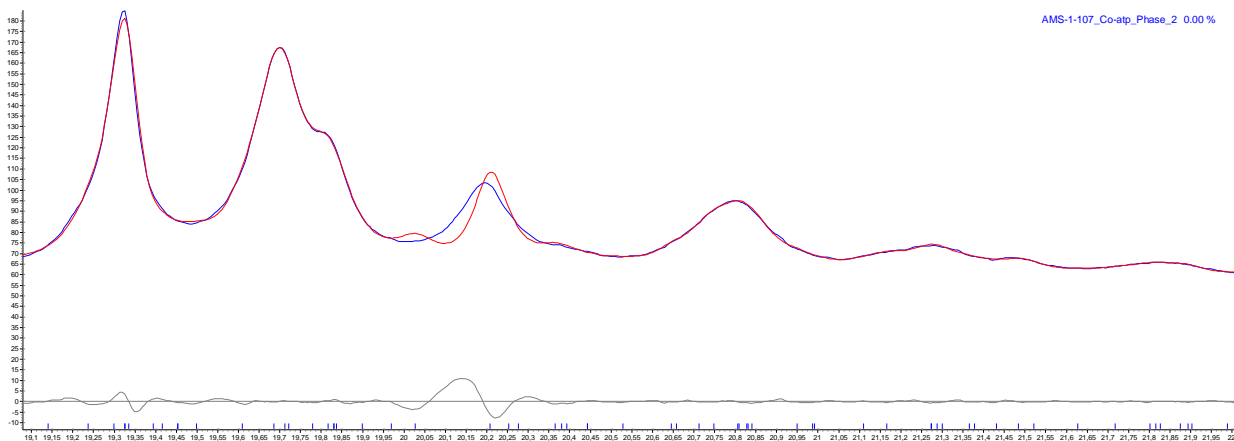
Figure A1.5 - *A PXRD fit, showcasing misfitting peak at 2θ = 20°. Co-ATP, P4/nbm, Phase 2.*
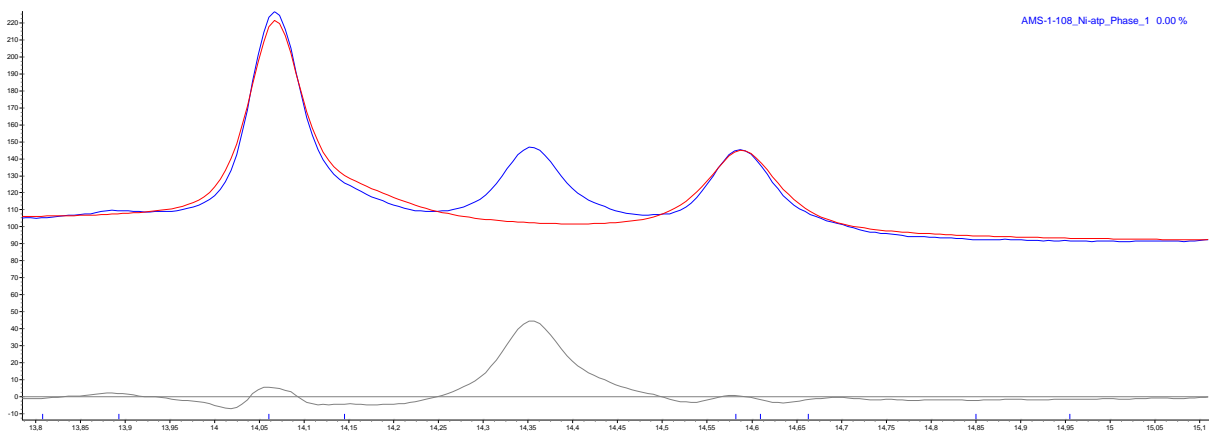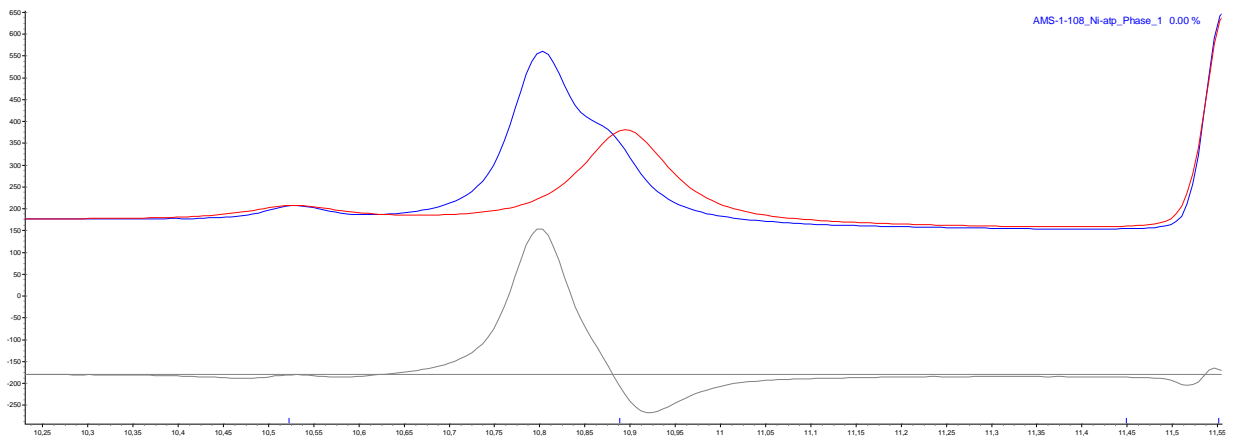
Figure A1.6 - *A PXRD fit, showcasing unaccounted for peak at 2θ =10° and 14°. Ni-ATP, I4/mcm,*

Phase 1.
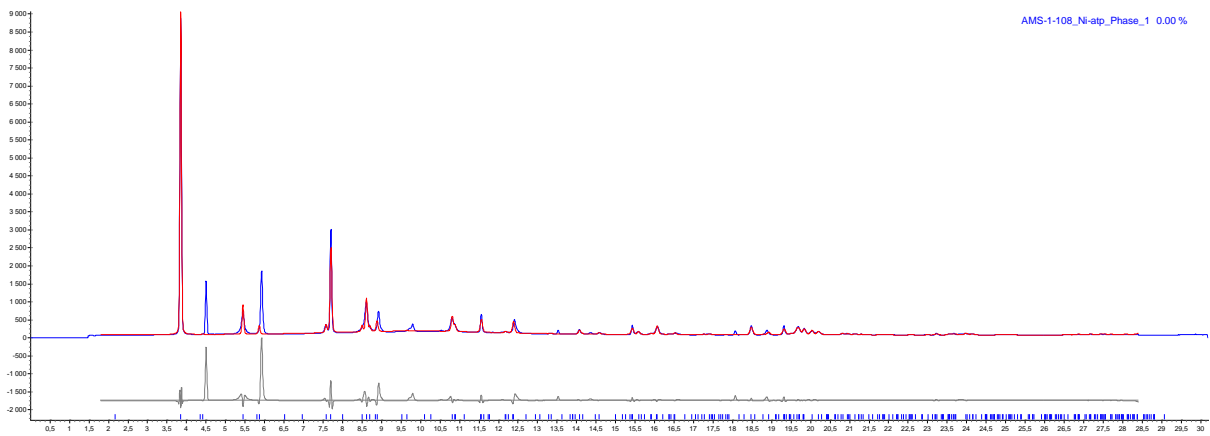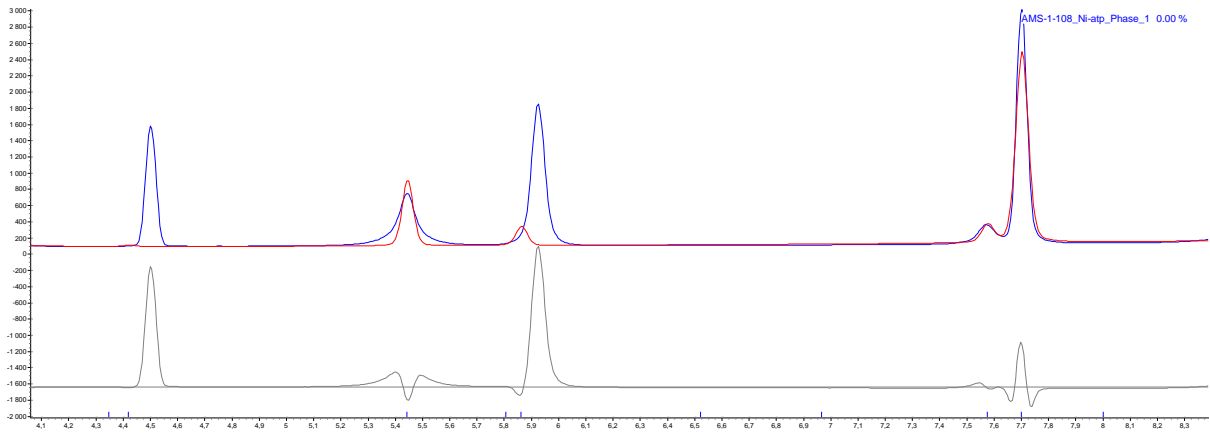
Figure A1.7 - A PXRD fit, showcasing unaccounted for peaks. Ni-ATP, P4/mmm, Phase 1.
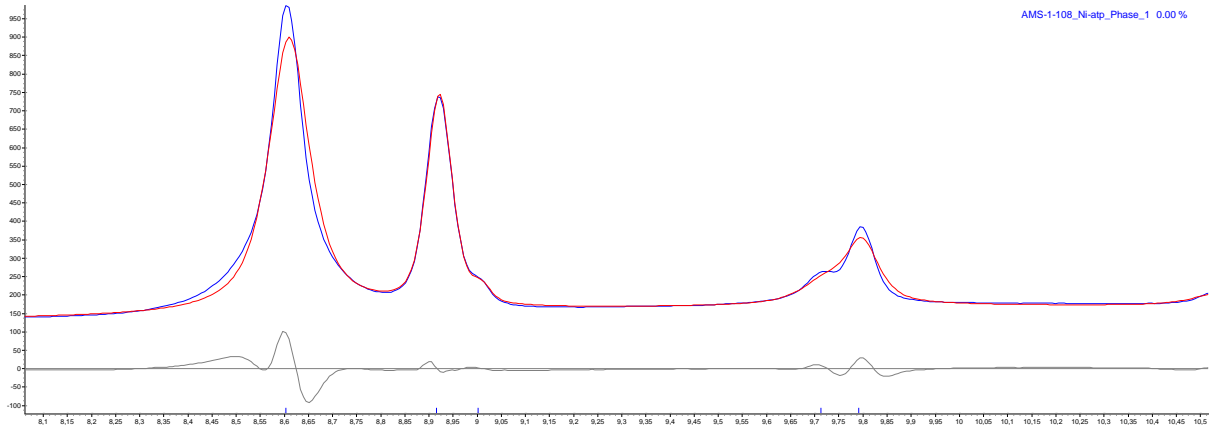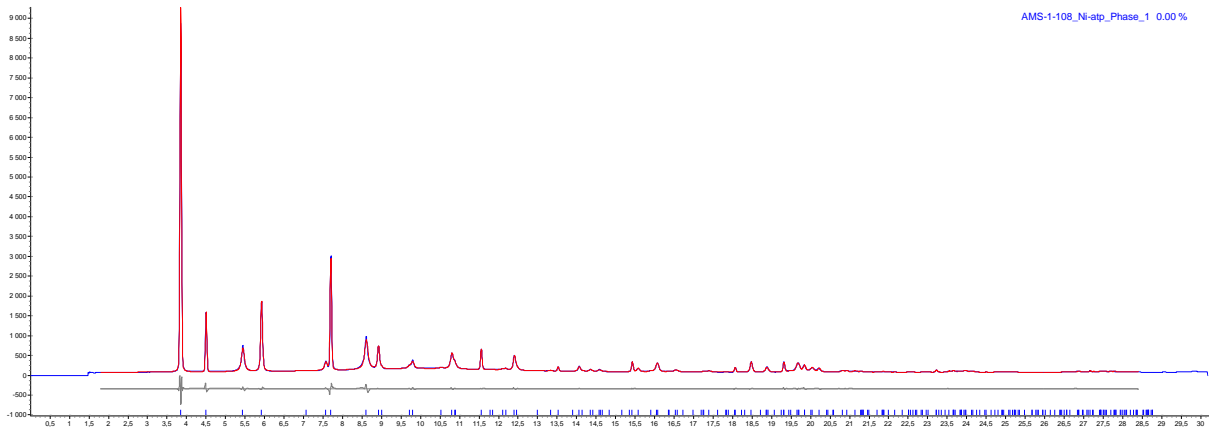
Figure A1.8 - *A PXRD fit, showcasing disparities in the fit and the entirety of the plot. Ni-ATP, P4/nbm,*

Phase 1.
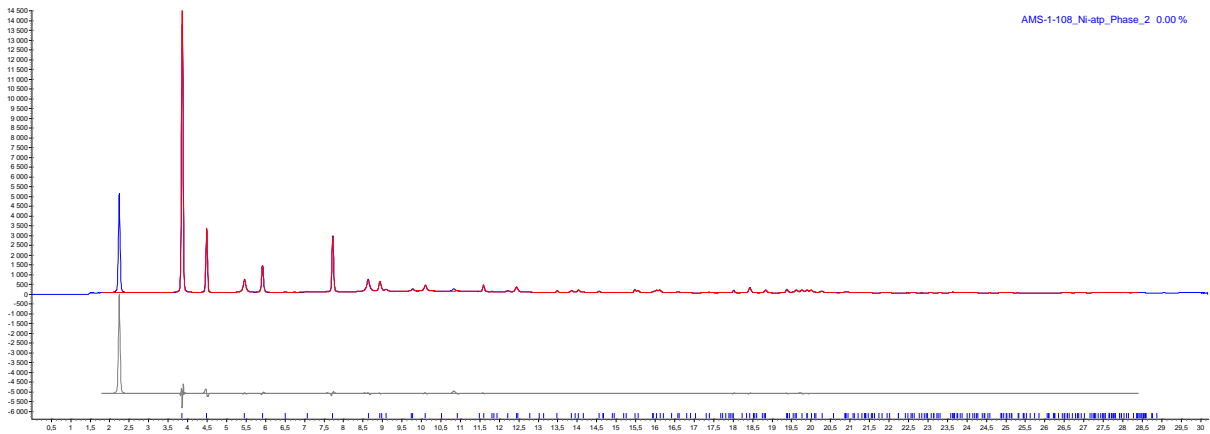
Figure A1.9 - *A PXRD fit, showcasing unaccounted for peak at 2θ =2.2° and the overall fit. Ni-ATP,*

I4/mcm, Phase 2.
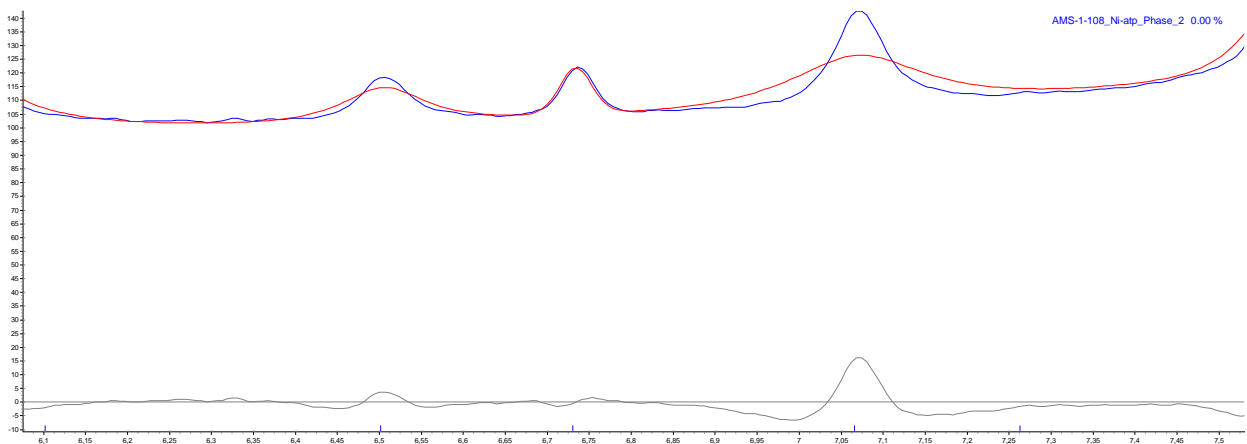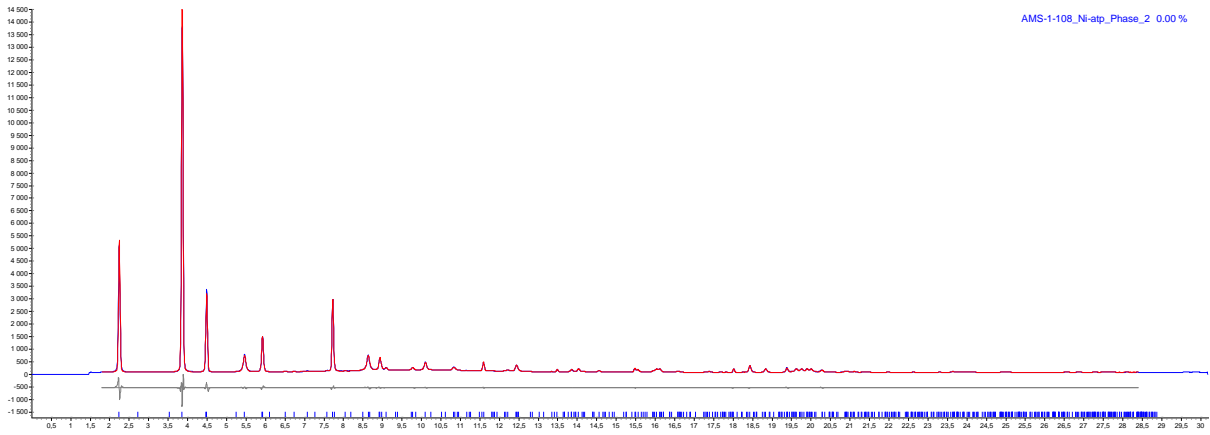
Figure A1.10 - *A PXRD fit, showcasing badly fitting peak at 2θ =7.1° and the overall fit. Ni-ATP, P4/mmm, Phase 2.*
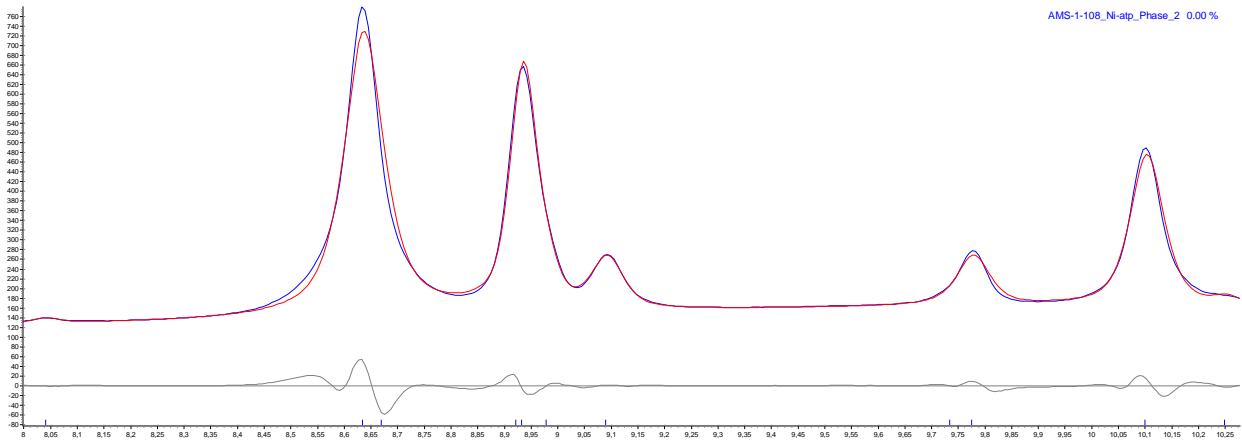
Figure A1.11 - *A PXRD fit, showcasing disparities in the fit at 2θ =8.6°. Ni-ATP, P4/nbm, Phase 2.*
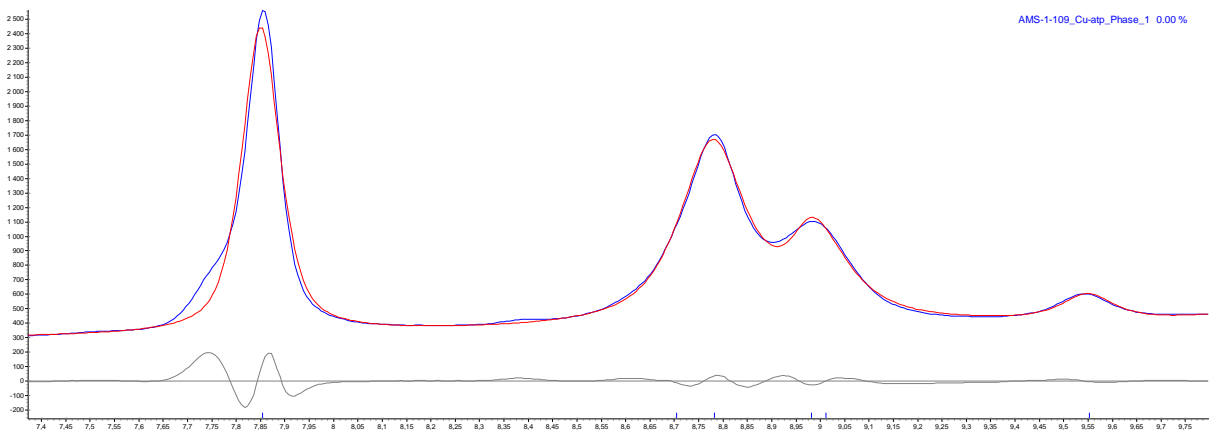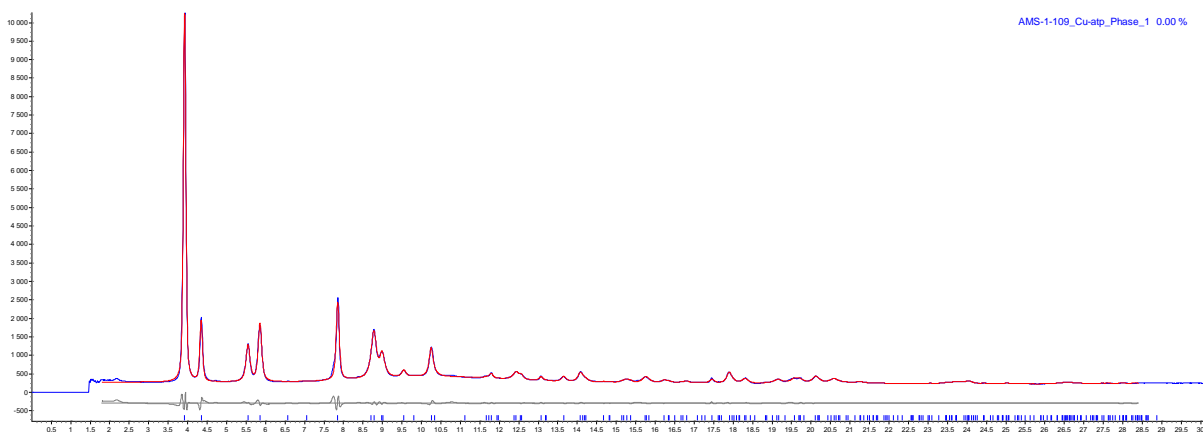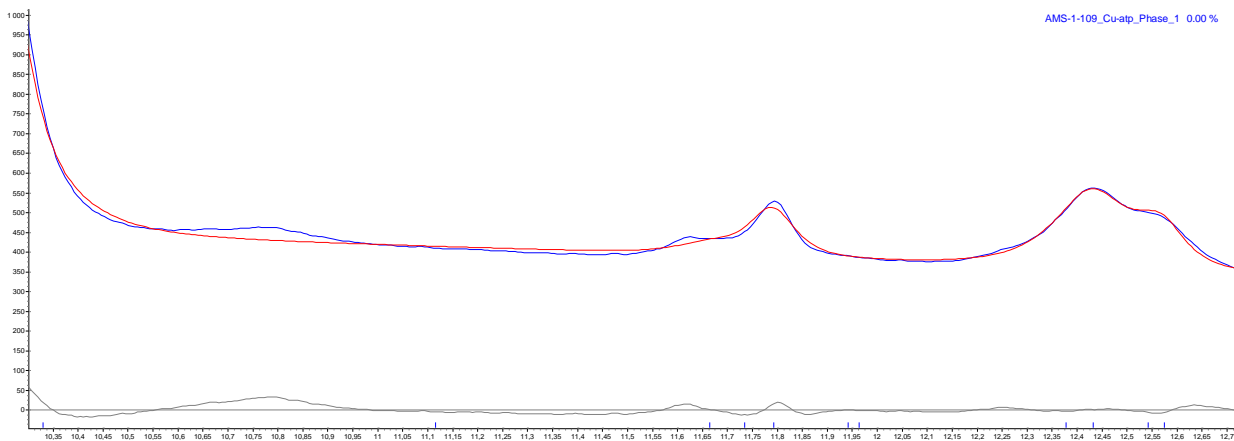
Figure A1.12 - *A PXRD fit, showcasing mismatching in the fit at 2θ =7.7°, 10.7° and 11.8°, together with overall plot. Cu-ATP, I4/mcm, Phase 1.*
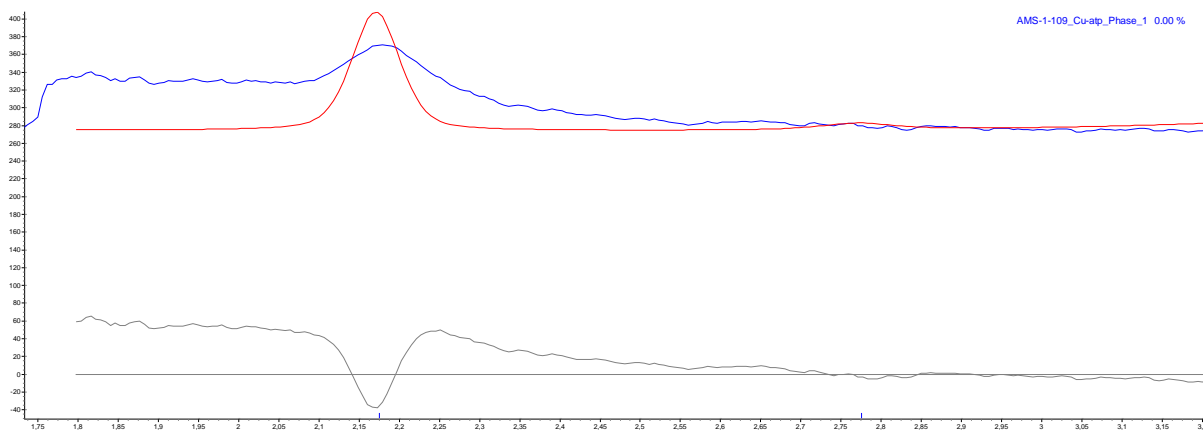
Figure A1.13 - *A PXRD fit, showcasing badly fitted peak at 2θ =2.2°. Cu-ATP, P4/mmm, Phase 1.*
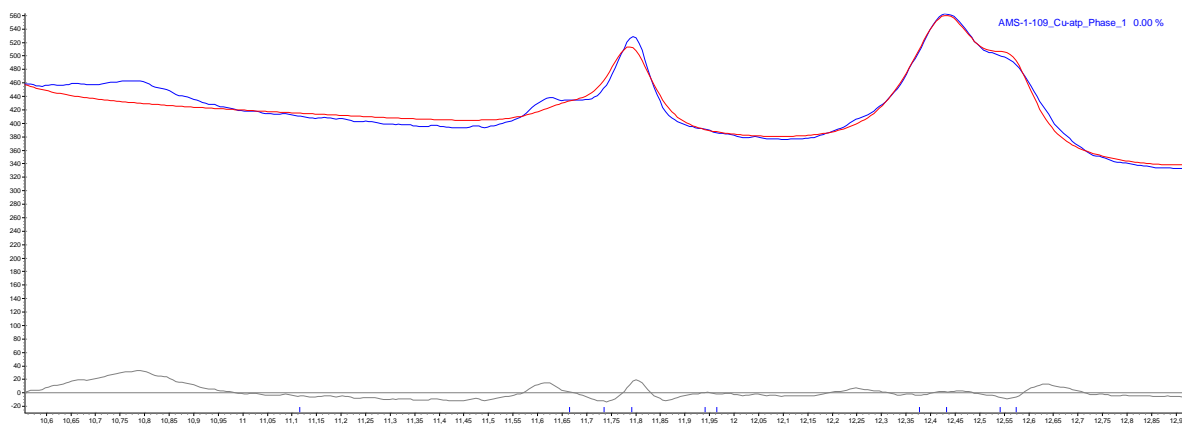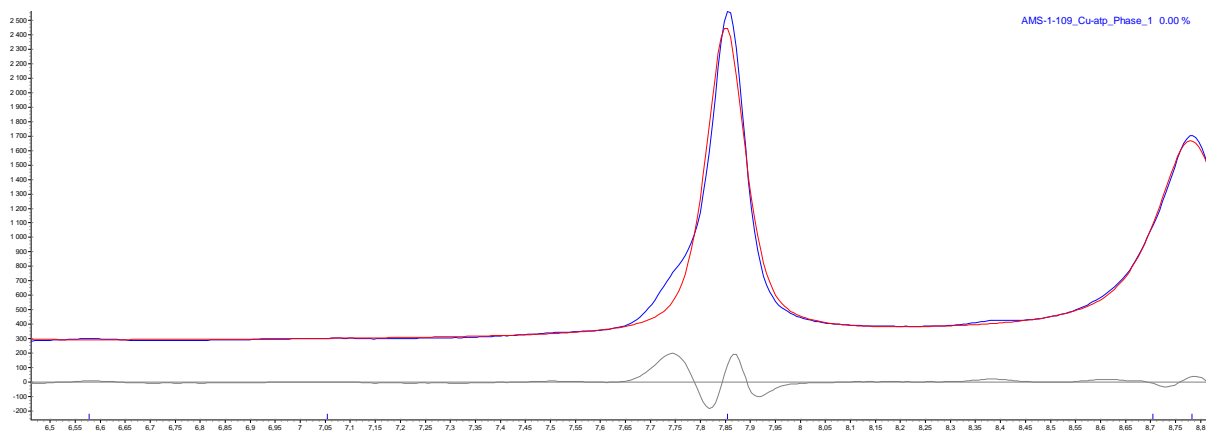
Figure A1.14 - *A PXRD fit, showcasing discrepancies at 2θ =7.7° and 11.6°. Cu-ATP, P4/nbm, Phase 1.*
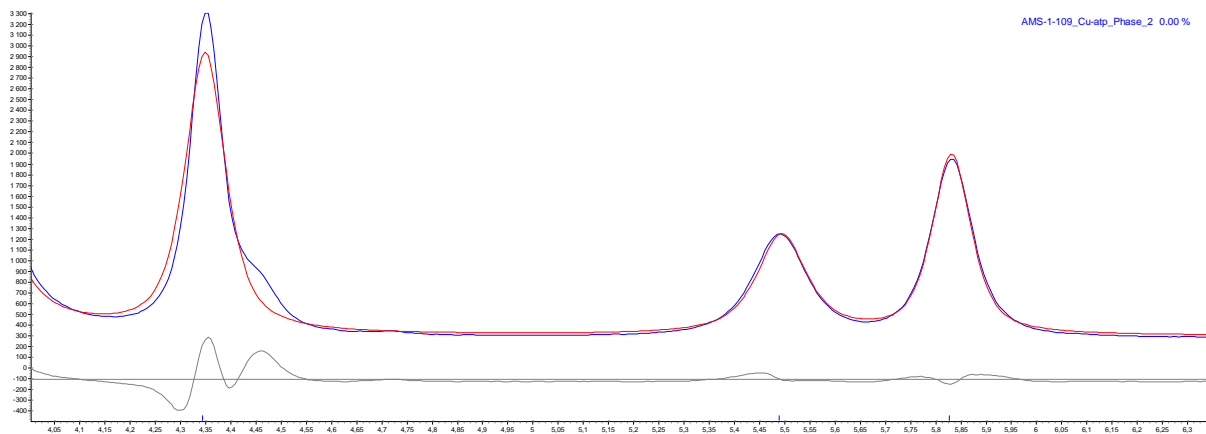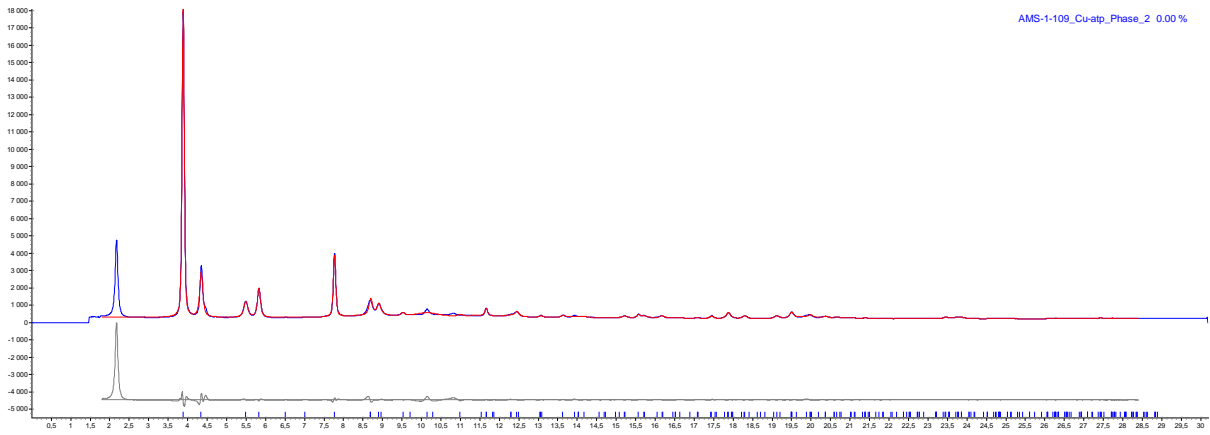
Figure A1.15 - *A PXRD fit, showcasing discrepancies at 2θ =4.3° and 4.5°, together with overall plot.*

Cu-ATP, I4/mcm, Phase 2.
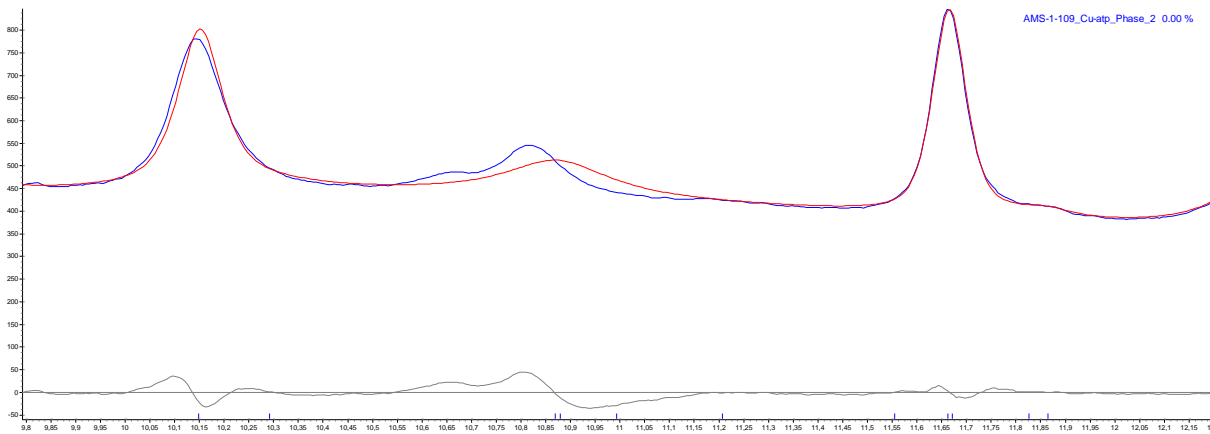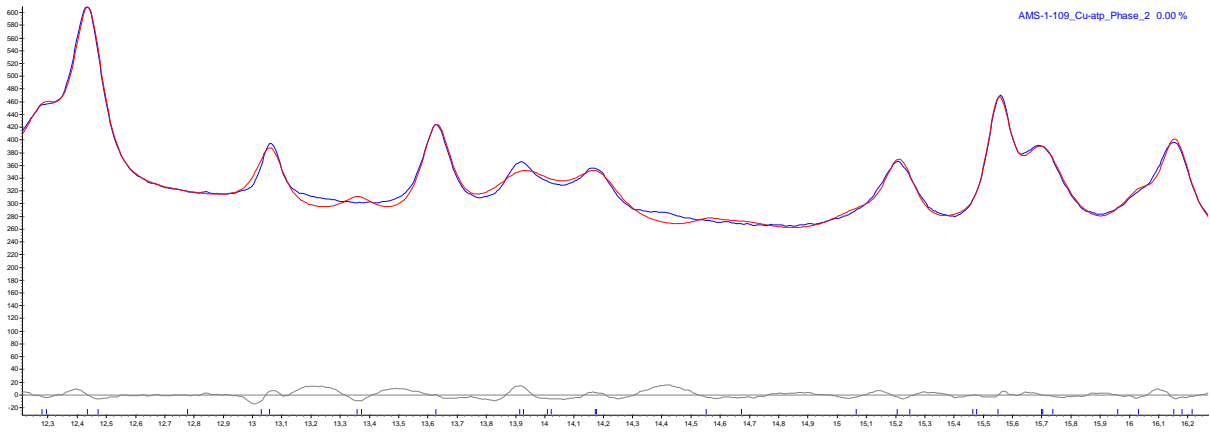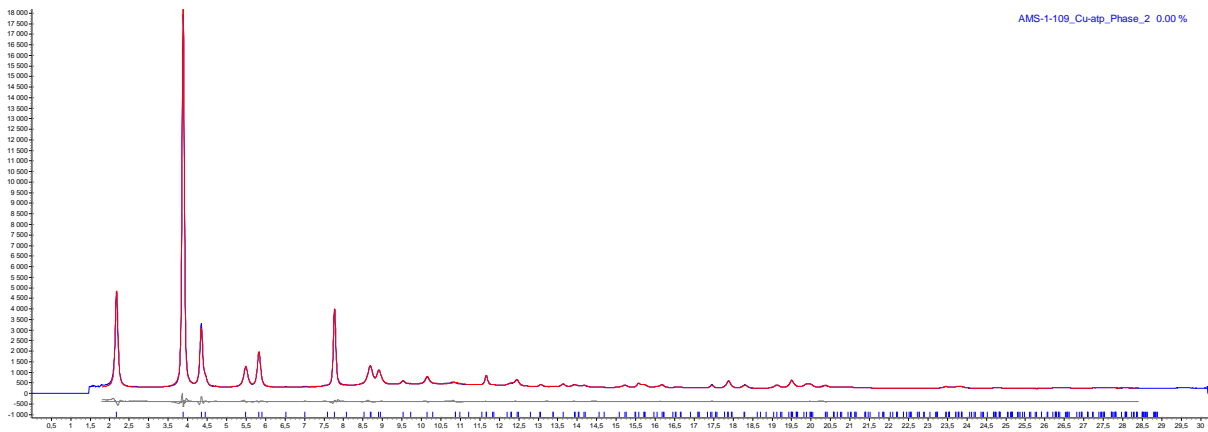
Figure A1.16 - *A PXRD fit, showcasing discrepancies at 2θ =10.6° and 14.0°, together with overall plot. Cu-ATP, P4/mmm, Phase 2.*
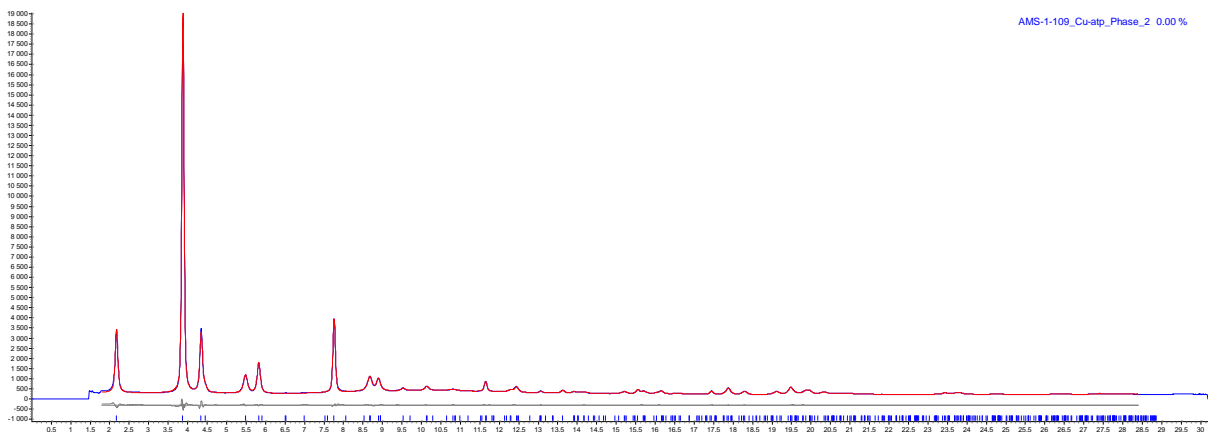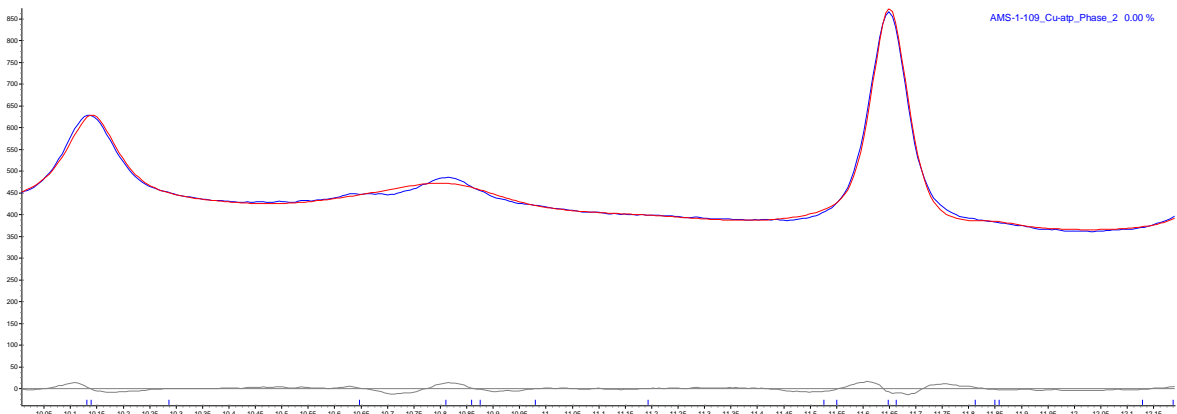
Figure A1.17 - *A PXRD fit, showcasing a discrepancy at 2θ =10.7°, together with overall plot. Cu-ATP, P4/nbm, Phase 2.*
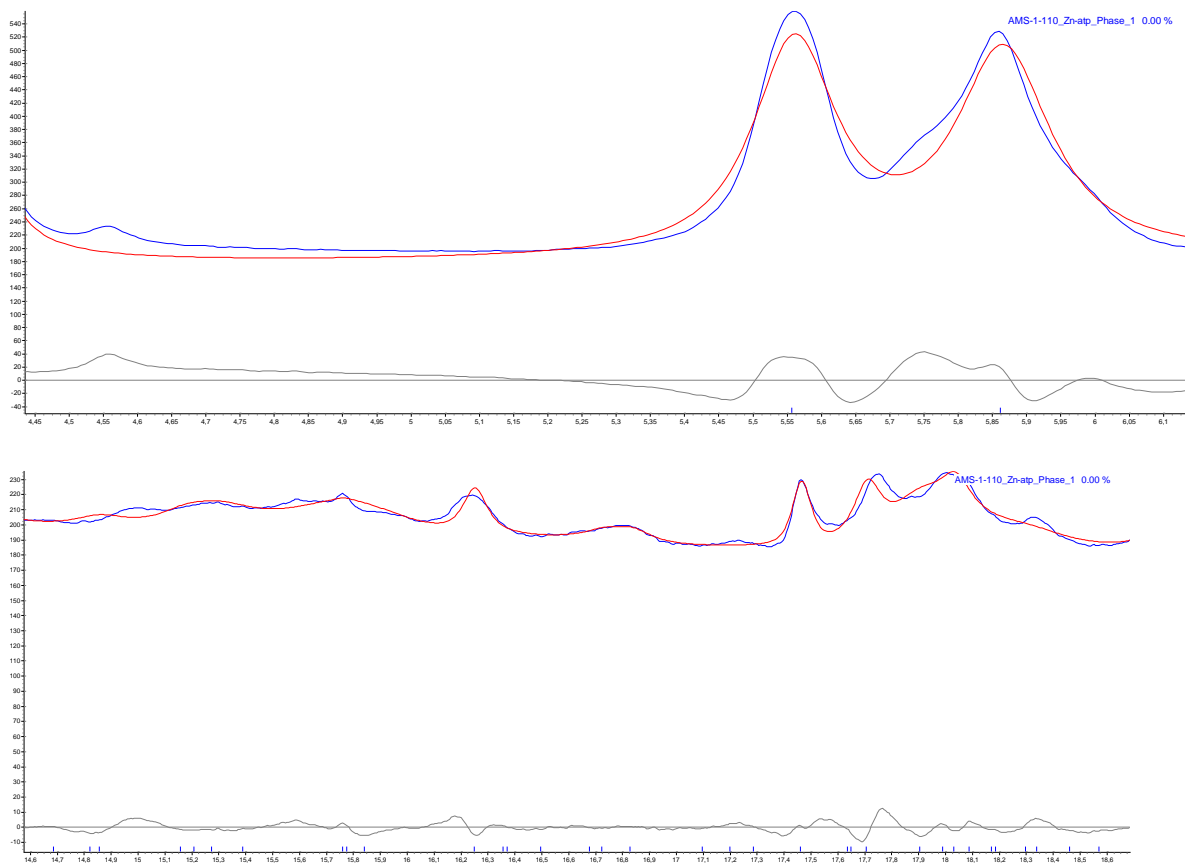
Figure A1.18 - *A PXRD fit, showcasing discrepancies at 2θ =5.5°, 5.8° and 15-19° range. Zn-ATP,*

I4/mcm, Phase 1.
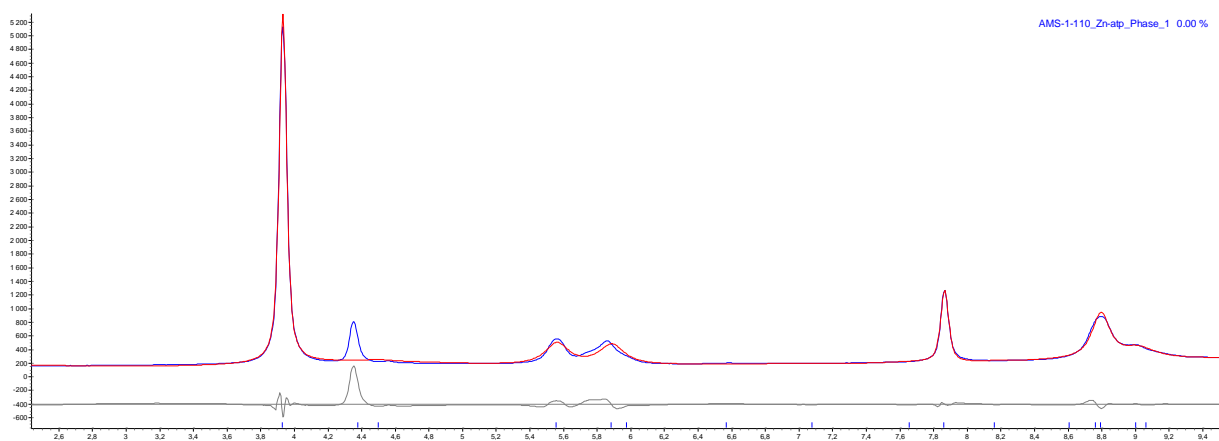
Figure A1.19 - *A PXRD fit, showcasing misfit at 2θ =4.4° and 5.8°. Zn-ATP, P4/mmm, Phase 1.*
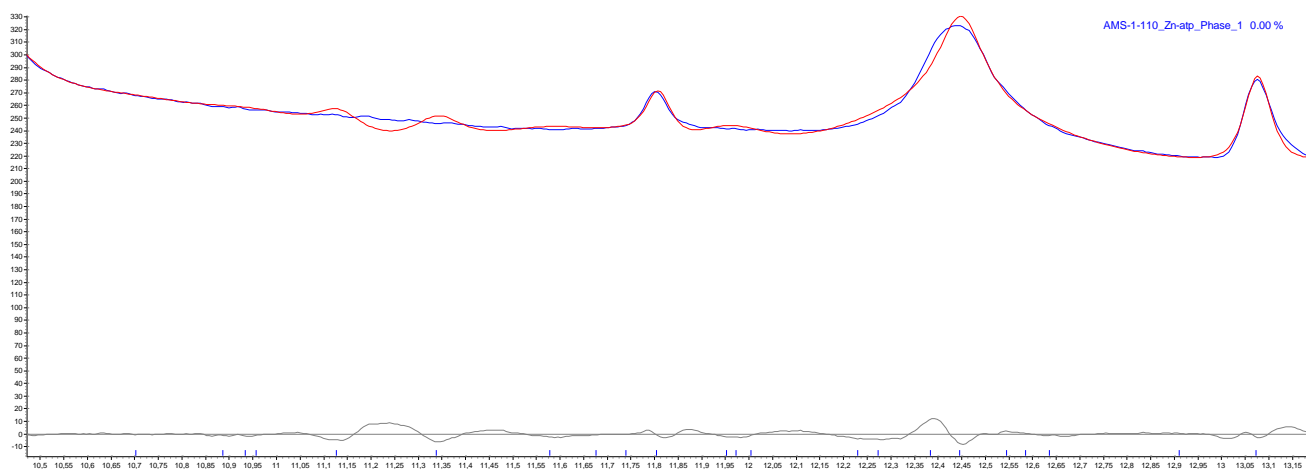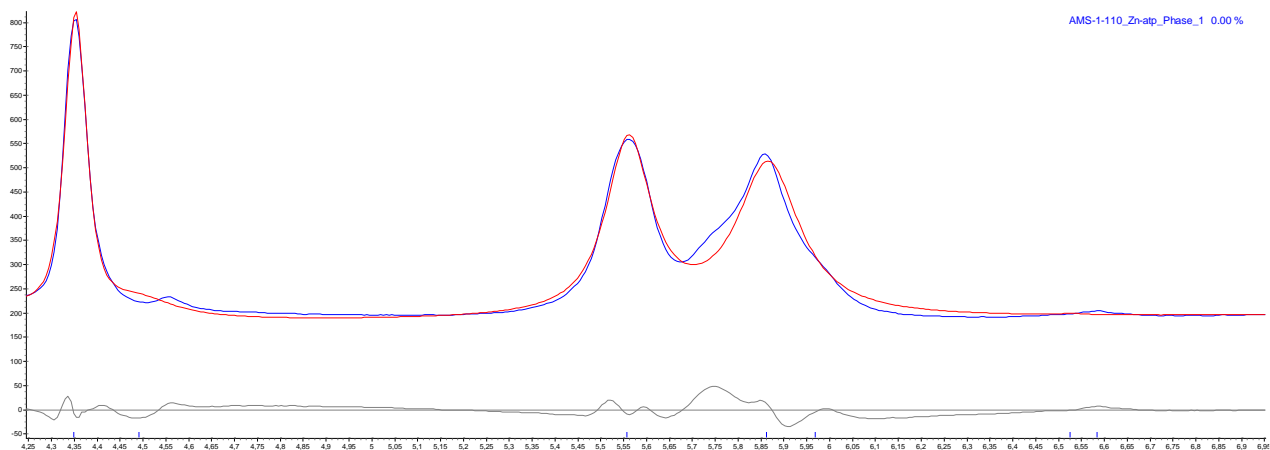
Figure A1.20 - *A PXRD fit, showcasing a misfit at 2θ =4.6°, 11.4°, 12.4° and shoulder at 2θ =5.7°. Zn-ATP, P4/nbm, Phase 1.*
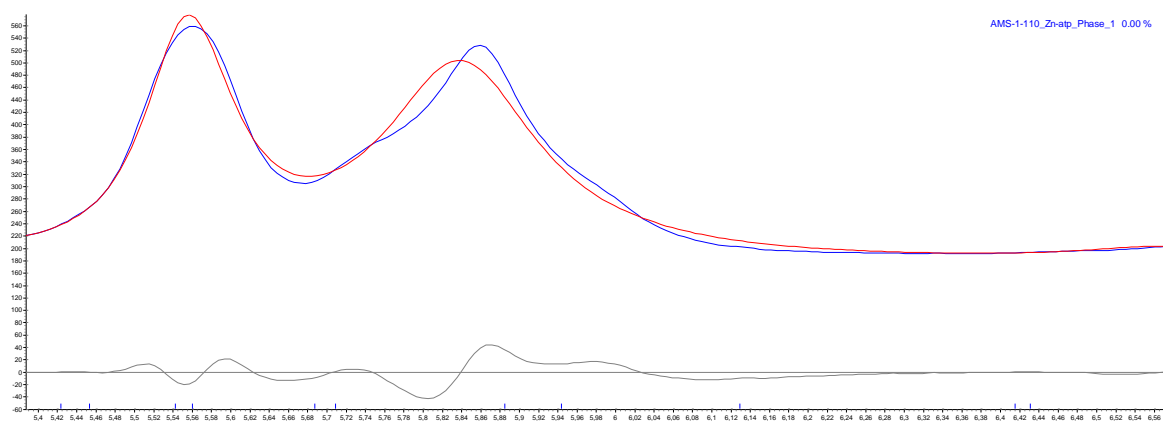
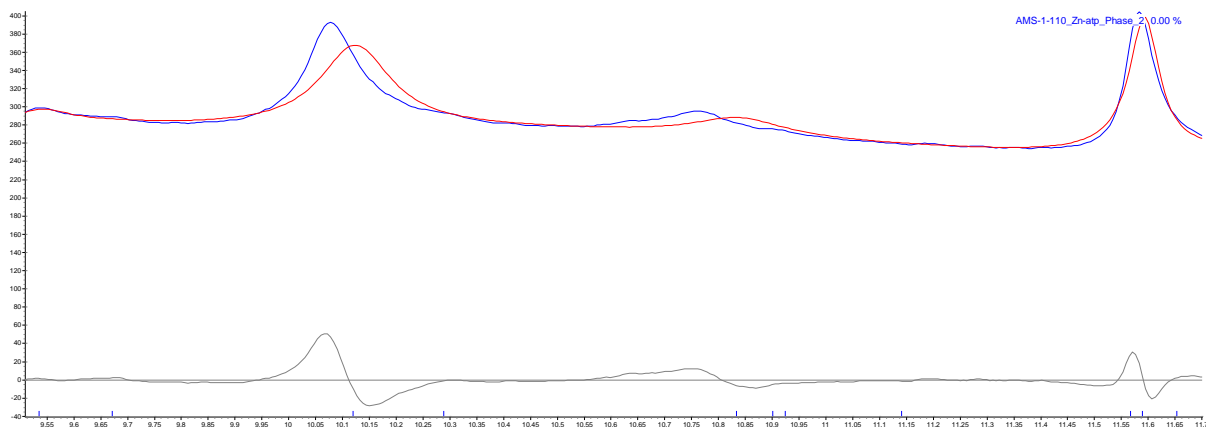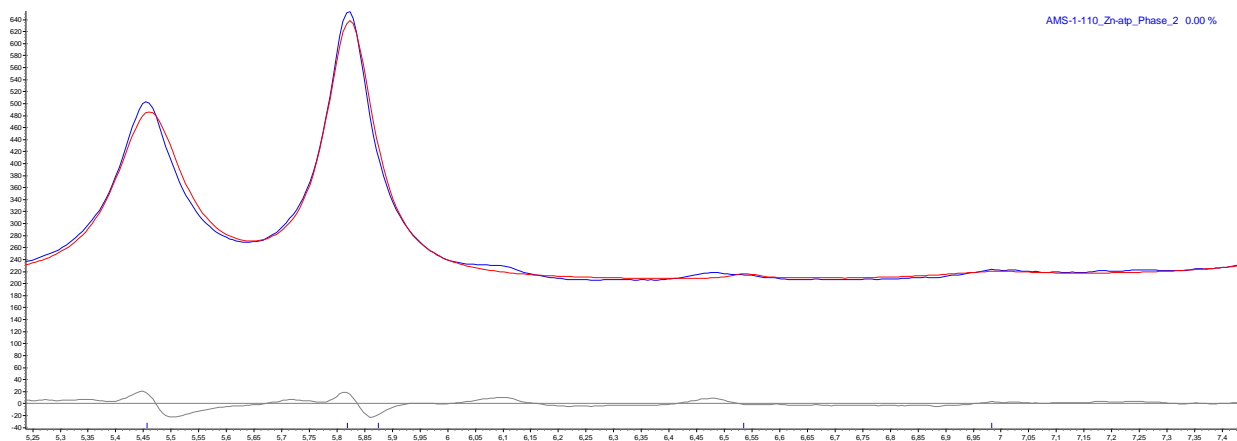***Figure A1.21 -*** *A PXRD fit, showcasing a misfit at 2θ =5.1°. Zn-ATP, Pnc2, Phase 1.*

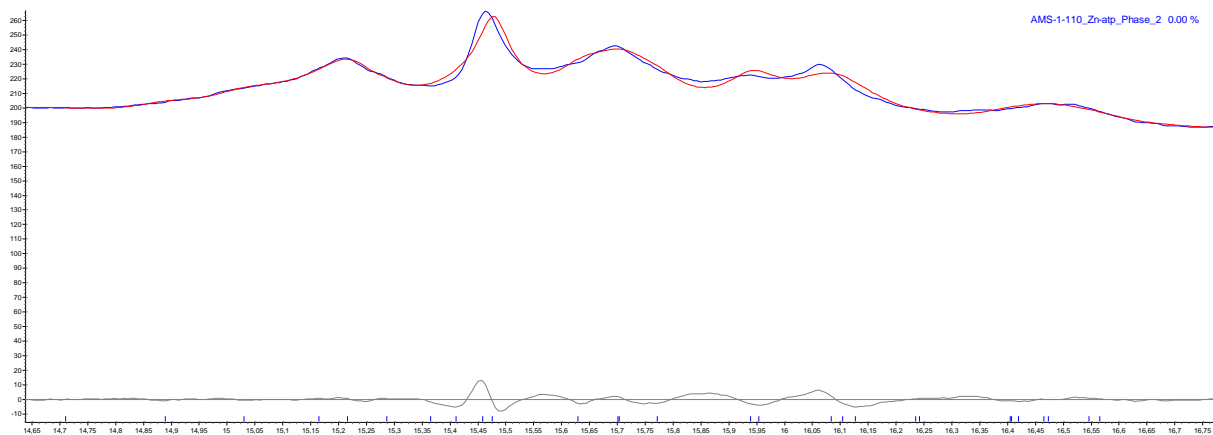*Figure A1.21 - A PXRD fit, showcasing misfits at 2θ =5.4°, 6.1°, 10.1° and 10.8°. Zn-ATP, P4/mmm, Phase 2.*

Figure A1.22 - A PXRD fit, showcasing misfits at 2θ =15.4° and 16.1°. Zn-ATP, P4/nbm, Phase 2.
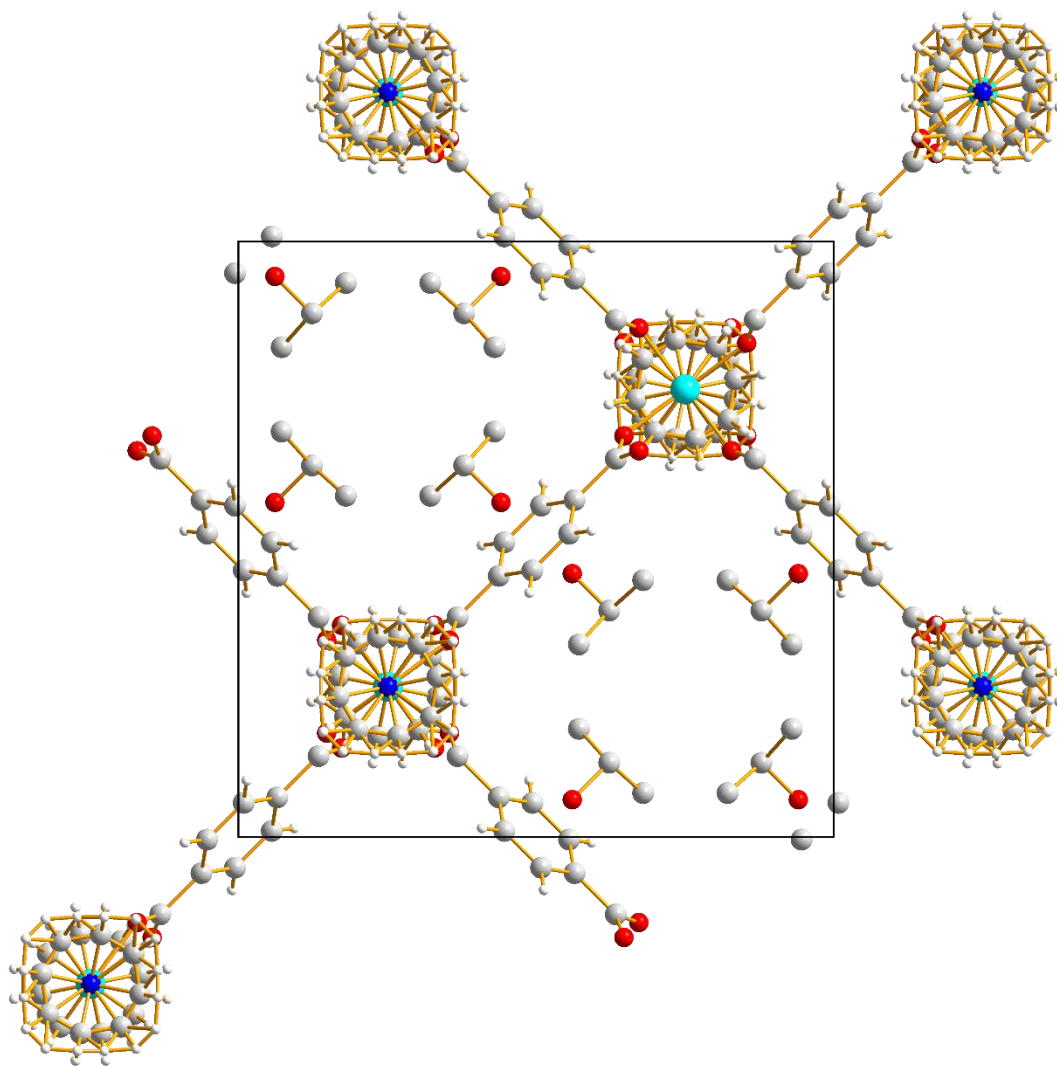
Figure A2 - *Unit cell portraying solvated (propan-2-ol) Zn$_2$(bdc)$_2$(dabco) in P4/nbm space group. Black lines indicate the unit cell's borders.*